

Electronic properties of carbon nanostructures

Martin Knupfer

*Institute for Solid State and Materials Research (IFW) Dresden,
PO Box 270016, D-01171 Dresden, Germany*



ELSEVIER

Amsterdam–London–New York–Oxford–Paris–Shannon–Tokyo

Contents

1. Introduction	3
2. Structural and theoretical background	4
2.1. The archetype fullerene C ₆₀	4
2.2. Higher fullerenes	8
2.3. Doping of fullerenes	9
2.4. Carbon nanotubes	12
3. Experimental details and spectroscopic techniques	15
3.1. Sample preparation	15
3.2. Electron energy-loss spectroscopy	17
3.3. Photoemission spectroscopy	19
3.4. X-ray absorption spectroscopy	20
4. Pristine fullerenes: from C ₆₀ to C ₈₄	21
5. Intercalated fullerenes	28
5.1. Alkali metal intercalation	28
5.1.1. A _x C ₆₀ ($x = 0, \dots, 6$)	28
5.2. A ₃ C ₆₀	31
5.3. A ₄ C ₆₀	36
5.4. K _x C ₇₀	40
5.5. Intercalation beyond $x = 6$: Na _x C ₆₀	41
5.6. Charge transfer to single molecule: C ₇₀ on potassium	44
5.7. Alkaline-earth intercalation	45
6. Heterofullerenes	49
7. Endohedrally doped fullerenes	55
7.1. La@C ₈₂	55
7.2. Tm@C ₈₂	56
7.3. K intercalated Tm@C ₈₂	59
8. Single-wall carbon nanotubes	62
9. Concluding remarks	67
Acknowledgements	67
References	68



ELSEVIER

Surface Science Reports 42 (2001) 1–74

surface science
reports

www.elsevier.nl/locate/surfrep

Electronic properties of carbon nanostructures

Martin Knupfer^{*}

Institute for Solid State and Materials Research (IFW) Dresden, PO Box 270016, D-01171 Dresden, Germany

Manuscript received in final form 28 November 2000

Abstract

Carbon nanostructures (the fullerenes and the carbon nanotubes) have become increasingly important during the last 15 years concerning both their basic physical and chemical properties as well as potential applications. In order to gain a basic understanding of the electronic properties of carbon nanostructures a wealth of experimental and theoretical studies has been performed world-wide. In this review, a summary of experimental studies of the electronic structure of carbon nanostructures using high-energy spectroscopies such as photoemission and electron energy-loss spectroscopy is presented and discussed. © 2001 Elsevier Science B.V. All rights reserved.

1. Introduction

Small structures with nanometer dimensions play a very important and even growing role in biology, chemistry, physics and material science. Examples are the huge number of biomolecules which form the basis of life on earth, small particles which act as catalysts for a lot of chemical reactions, polymers and oligomers which have the potential to form the basis of novel organic opto-electronic devices or future memory devices in computers.

The discovery in 1985 of a third allotrope of carbon, the fullerenes [1], has presented science with a new class of nanostructures that are solely based on carbon. Fullerenes are closed carbon molecules with sphere-like shape, a hollow core and diameters below 1 nm. Solid state fullerene science has been rendered possible by the development of a production process which enables the preparation of bulk quantities of these carbon nanostructures [2]. Within the large family of fullerene compounds and derivatives many fascinating and potentially useful properties have been found, among them superconductivity or ferromagnetism. Consequently, the discoverers of the fullerenes have been awarded the Nobel prize for chemistry in 1996.

In 1991 the family of pure carbon nanostructures has been enlarged by the discovery of carbon nanotubes [3] — very long fullerene molecules with lengths up to a few micrometers and a diameter of

^{*} Tel.: +49-351-4659-544; fax: +49-351-4659-440.

E-mail address: m.knupfer@ifw-dresden.de (M. Knupfer).

only a few nanometers. Again, the successful development of a high yield mass production in 1996 [4] opened a new research field — the carbon nanotubes — exhibiting novel properties reaching from the “strongest fibers that can be made” to carbon based nanowires. Furthermore, only shortly after their discovery the carbon nanotubes have been shown to be useful for technical applications, e.g. as emitting components in field emission displays [5].

In this paper high-energy spectroscopic studies of the basic electronic properties of these new carbon nanostructures in the solid state are discussed. At present, there are a number of review articles available which cover different aspects of the physical and chemical properties of fullerenes [6–9], for instance on their crystal structures and phase diagrams [10,11], optical properties [12,13], superconductivity [11,14,15], magnetism [16], vibrational [17] or electronic properties [18–21]; as well as the various properties of carbon nanotubes [22]. These publications provide a more detailed treatment of the many aspects of fullerene and nanotube research which are beyond the scope of this paper.

In the second section some of the issues relevant for the discussion of the electronic structure of the fullerenes, their derivatives, their compounds and the carbon nanotubes are introduced. Section 3 gives some details about the sample preparation techniques and the experimental methods, while the experimental results are presented and discussed in Sections 4–8. Section 9 then gives a short summary.

2. Structural and theoretical background

2.1. The archetype fullerene C_{60}

The most abundant stable fullerene, C_{60} , which is at the same time the molecule with the highest symmetry (I_h), is built of carbon atoms with predominantly sp^2 -hybridization which are assembled in the form of a truncated icosahedron. The carbon atoms thus outline 20 hexagons and 12 pentagons, the latter of which give rise to the curvature and thus enable the closed quasi-spherical structure of the molecule as shown in Fig. 1. The formation of the most abundant fullerenes satisfies the isolated pentagon rule (IPR) which states that a stable, non-reactive fullerene is only formed when the

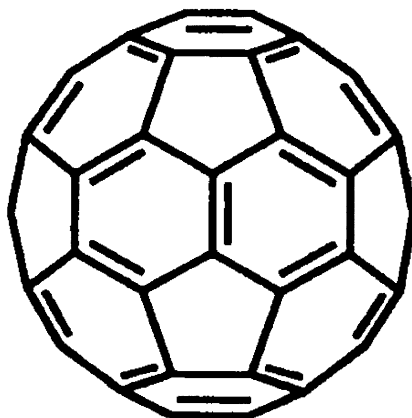


Fig. 1. Structure of the C_{60} molecule. C_{60} consists of 20 hexagons and 12 pentagons with carbon atoms at each corner.

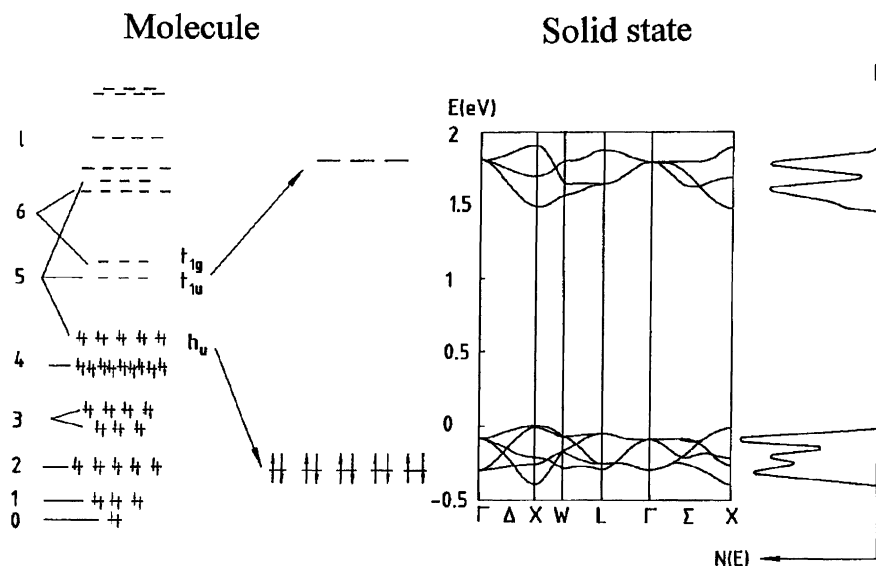


Fig. 2. Schematic representation of the π -derived molecular electronic levels of C_{60} and the formation of the band structure in the solid state as predicted from LDA band structure calculations [27]. Additionally shown is the electronic DOS $N(E)$.

pentagons at its surface are separated. Thus, C_{60} is the smallest stable fullerene formed and there is only one isomer of it. Smaller, non-IPR structures like C_{20} [23] and C_{36} [24] have been produced successfully but, due to their high reactivity, can only be studied in the gas phase or in an oligomerized/polymerized form in the solid.

The diameter of the C_{60} molecule is about 7.1 Å. There are longer C–C bonds (1.446 Å) between a hexagon and a pentagon and shorter bonds (1.402 Å) between two hexagons which are usually addressed as single and double bonds, respectively, although they significantly differ from true single and double C–C bonds in other carbon based materials [17]. The C_{60} molecular structure results in a closed-shell electronic structure with highly degenerate π - and σ -derived molecular electronic states including the π -derived fivefold degenerate highest occupied molecular orbital (HOMO) with h_u symmetry and a triply degenerate lowest unoccupied molecular orbital (LUMO) with t_{1u} symmetry as shown in Fig. 2 [25]. Upon condensation into a solid the C_{60} molecules form a close-packed structure with face-centered cubic (f.c.c.) symmetry and a lattice constant under ambient conditions of $a_0 = 14.198$ Å [26]. In the solid the intermolecular interaction is of the van der Waals type and thus relatively weak. This is expressed, e.g., in a very small cohesive energy of only 1.6 eV per C_{60} molecule [27]. Solid C_{60} undergoes two phase transitions which are connected with the rotational degrees of freedom of the C_{60} molecules. At room temperature the molecules rotate freely, leading to a lattice with f.c.c. symmetry. Below 260 K a first order transition occurs to an orientationally ordered simple cubic (sc) phase in which the molecules can only ratchet from one preferred orientation to another. This ratcheting is finally frozen out in a glass transition at about 90 K [28].

The electronic band formation in the solid is predominantly governed by the weak overlap of the π -derived molecular orbitals leading to narrow bands, whereby the bandwidth of the t_{1u} -derived conduction bands is calculated to be about 0.5 eV [27]. In Fig. 2 the band structure of solid C_{60} is reproduced as obtained from calculations within the local density approximation (LDA) [27]. Within

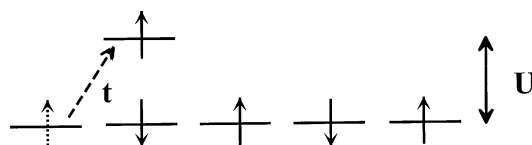


Fig. 3. Schematic representation of a one-dimensional Hubbard chain. Each site is occupied by one electron, the electrons can hop to the nearest neighbor which is controlled by the hopping parameter t and two electrons at the same site repel each other (Coulomb energy U).

LDA, a direct band gap of about 1.5 eV is predicted, the precise value of which differs slightly from one calculation to the next [19,27,29]. As a consequence of the weak intermolecular interaction in the solid, the molecular character and symmetry of the electronic states are scarcely altered, which leaves the transition across the optical gap formally optically forbidden.

The weak intermolecular interaction and the resulting molecular nature of fullerene solids also result in a charge distribution which is rather inhomogeneous with the charge mainly confined to a shell with a radius of about 3.5 Å. This charge confinement is reminiscent of the situation found in many materials with partly filled 3d or 4f electronic levels, i.e. one could expect the Coulomb energy U , which describes the Coulomb repulsion of two electrons on the same C_{60} molecule, to play an important role in a complete description of the electronic structure of fullerene solids. These electronic correlations cause a deviation of the electronic properties from the predictions within LDA, as such calculations treat exchange and correlation effects in a mean-field free electron approach only. The consequences of electronic correlations can be visualized considering a simple, one-dimensional so-called Hubbard chain. Such a chain consists of one orbital per site which are all filled with one electron as illustrated in Fig. 3. The electrons can hop to adjacent sites which is described by a hopping parameter t , analogous to the tight-binding approximation. The electron spins are antiferromagnetically ordered, as otherwise the Pauli principle would forbid hopping. In addition, two electrons at the same site repel each other described by the Coulomb energy U . Thus, hopping to a neighboring site costs this energy U which results in an effective splitting of the half-filled band into two bands, the lower and the upper Hubbard band (see Fig. 3). As long as the splitting is larger than the bandwidth $W = 4t$ the chain is insulating and called a Mott insulator. As the bandwidth increases an insulator-to-metal transition will occur at $U = W$. This behavior is shown in Fig. 4.

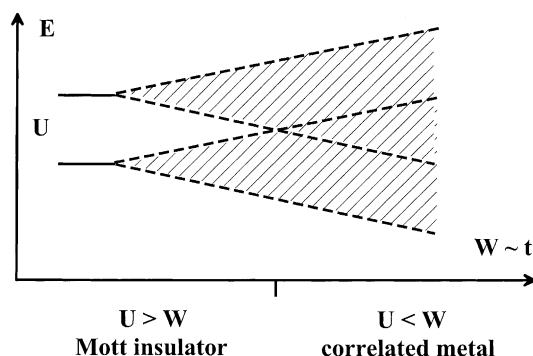


Fig. 4. Electronic levels of a one-dimensional Hubbard chain as a function of the Coulomb energy U and the bandwidth W . At small W , the upper and the lower Hubbard band are separated by a gap which closes at $U = W$, where the system undergoes an insulator-to-metal transition.

In a real system the situation might be more complicated but these simple considerations still allow a general understanding of the observed phenomena. For solid C_{60} and C_{70} the quantity U which describes the Coulomb repulsion of two holes in the valence states has been determined from a comparison of the C KVV Auger spectrum with a self-convoluted photoemission valence band spectrum and has been found to be 1.4–1.6 eV for C_{60} [30] and about 1 eV for C_{70} [31]. Furthermore, it was shown that U does not change significantly in the alkali metal intercalated C_{60} compounds [32]. U is thus larger than the bandwidth predicted from band structure calculations and places fullerene solids in the regime of a strongly correlated electron system. In the context of the results presented below, the impact of U on the electronic structure of fullerene solids will be discussed in more detail.

Also as a result of their molecular nature there is strong electron–phonon coupling present in fullerene solids, especially between the valence electrons and the intramolecular vibrations. This makes the doped molecules with partly filled orbitals susceptible to a Jahn–Teller distortion [33–35] and thus can have a considerable impact on the electronic properties of the material in question. Electron–phonon coupling, for instance, has been discussed as the major driving force of the superconductivity in A_3C_{60} compounds [15,19,36,37]. The Jahn–Teller derived splitting of the formerly degenerate electronic levels might also determine the magnetic ground state of doped fullerene molecules. Provided the Jahn–Teller splitting is larger than the Hund’s rule exchange energy, the system will be in a low spin ground state. Calculations indicate that this is the case for C_{60}^{n-} molecules ($n = 2, 3, 4, 5$).

Furthermore, a Jahn–Teller distortion of the fullerene molecules can directly modify the Coulomb repulsion energy U via the Jahn–Teller contribution U_{JT} to this repulsion energy. From the discussion above it is clear that the on-site interaction U in a system with n electrons is generally defined by the energy needed to transfer one electron from one site to another, which both had originally n electrons:

$$U(n) = E(n+1) + E(n-1) - 2E(n). \quad (1)$$

$E(n)$ denotes the energy of the state with n electrons. A closer inspection of Fig. 5 and Eq. (1) reveals that the Jahn–Teller splitting of the electronic levels also results in a Jahn–Teller contribution to the repulsion energy, U_{JT} , which is significantly different for C_{60} molecules with an odd or an even number of electrons, respectively. For instance, $U_{JT}(n=3)$ is found to be negative while $U_{JT}(n=4)$ adds a positive contribution to the total U :

$$E_{JT}(n=4) + E_{JT}(n=2) - 2E_{JT}(n=3) < 0, \quad (2)$$

$$E_{JT}(n=5) + E_{JT}(n=3) - 2E_{JT}(n=4) > 0. \quad (3)$$

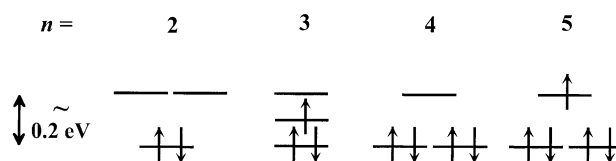


Fig. 5. Schematic energy level diagram of the threefold degenerate LUMO of C_{60} after filling with n electrons and the following Jahn–Teller distortion of the molecule. The Jahn–Teller splitting of the electronic levels exceeds the Hund’s rule exchange energy which leaves the doped molecule in a low spin ground state.

More detailed theoretical considerations also arrived at this result and predicted U_{JT} to be about -0.15 and $+0.35$ eV for $n = 3$ and 4 , respectively [33–35,38]. In Section 5, the effect of U_{JT} on the electronic ground state of alkaline intercalated C_{60} compounds will be discussed.

Moreover, fullerene solids are highly disordered materials which is another direct consequence of their weak intermolecular interactions and their rich molecular dynamics. For instance, below the glass transition at 90 K, 85% of the C_{60} molecules are found in one orientation and the remaining 15% in another orientation with slightly higher energy [28]. Furthermore, in A_3C_{60} materials the crystal structure possesses so-called merohedral disorder with a statistical occupancy of the two possible molecular orientations of the C_{60} molecules [39]. This disorder has been calculated to have an impact on the electronic structure. The fine structure in the density of states (DOS) has been predicted to be smeared out, the bandwidth, however, is expected to remain unchanged [40]. Calculations for K_3C_{60} indicated that in spite of disorder the states near the Fermi level are relatively unaffected and states that are localized due to disorder lie at the bottom and the top of the conduction bands [41], i.e. the disorder has only a minor effect on the electronic properties of fullerene compounds.

2.2. Higher fullerenes

The formation of higher fullerenes (C_{70} , C_{76} , C_{78} , C_{80} , C_{82} , C_{84} , etc.) offers one possibility to modify the electronic properties of fullerenes. Fullerene structures up to C_{116} have been isolated up to now, most of them only in very small amounts. Consequently, these higher fullerenes have been much less widely investigated as regards their physical properties. They also adopt a close-packed crystal structure [42–45], the symmetry, molecular orientation and temperature dependence of which is much more complicated than that of C_{60} due to the lower molecular symmetries and, for some higher fullerenes, the considerable deviation from a quasi-spherical shape [46]. In the case of C_{70} , e.g., hexagonal closed packed (h.c.p.) or f.c.c. phases are observed, which also differ in their temperature-dependent behavior, depending upon the preparation history of the sample [42,43]. A further degree of freedom comes into play for higher fullerenes larger than C_{76} because for each number of carbon atoms there exists more than one structural isomer of the fullerene. These complications notwithstanding, some of the physical properties follow general trends that are easy to visualize and that provide an initial understanding of the observed changes with the size of the molecule. One instructive example is the lattice constant a for higher fullerene solids which increases proportional to $\sqrt{n_C}$, where n_C is the number of carbon atoms forming the corresponding fullerene [45]. This behavior is depicted in Fig. 6

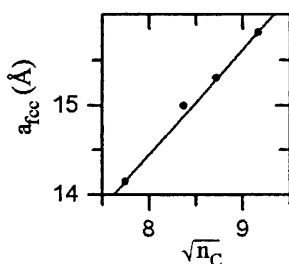


Fig. 6. Lattice constant, $a_{f.c.c.}$, of some higher fullerenes as a function of $\sqrt{n_C}$, n_C is the number of carbon atoms forming the corresponding fullerene [45]. The fullerenes presented (C_{60} , C_{70} , C_{76} and C_{84}) all crystallize in an f.c.c.-like close-packed structure.

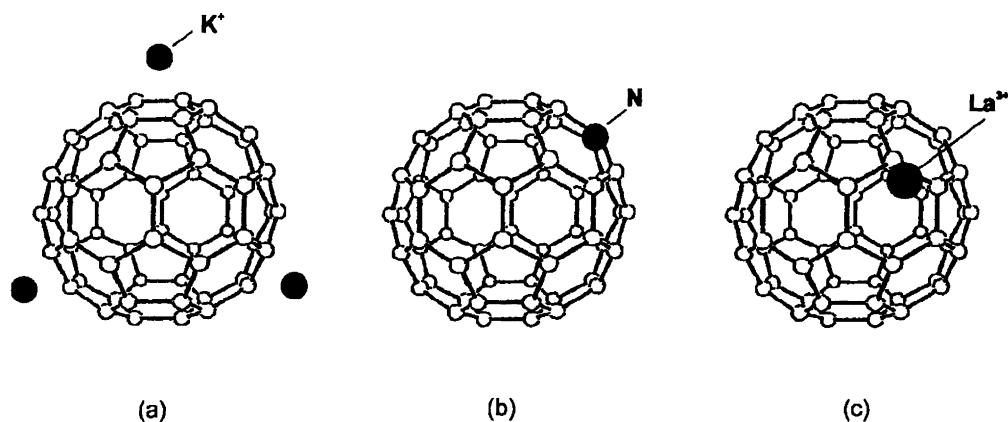


Fig. 7. The three possibilities to dope fullerenes: (a) from outside (intercalation) leading to fullerene salts; (b) on-ball (so-called heterofullerenes); (c) from inside (endohedral or metallofullerenes).

and arises from the fact that the mean radius of the molecules is roughly proportional to $\sqrt{n_C}$ because the C–C bond lengths do not change significantly with the size of the fullerene molecules. As far as the electronic structure of the higher fullerenes is concerned, the general trends and deviations from them are discussed below (Section 4).

2.3. Doping of fullerenes

The main route chosen to alter the electronic properties of fullerenes in a controlled way is to dope them, i.e. to add or remove electrons either to the conduction or from the valence states, respectively. In principal, this can be done in three ways: doping from outside the molecules, doping from inside or changing the molecular structure itself as it is depicted schematically in Fig. 7. All these routes have been successfully followed resulting in a large number of fullerene intercalation compounds (fullerene salts, doping from outside), endohedrally doped fullerenes (metallofullerenes, doping from inside) or heterofullerenes (substituting C atoms with heteroatoms like N or B). In addition, doping from outside can also be achieved via charge injection in a field effect device [47]. These developments were also successful in their aim of property engineering whereby fullerene-based materials now support a wide range of properties such as metallic conductivity [48], superconductivity [47,49–57], ferromagnetism (without the presence of d or f electrons) [58,59], non-linear optical properties [60–62] or polymer formation [63,64]. p-Type doped fullerene solids have not been synthesized yet which is due to the large ionization potential of C₆₀ (~ 7.6 eV [65]) and the next higher fullerenes.

For C₆₀, a number of intercalation compounds have been prepared with predominantly the alkali (A) or alkaline-earth (AE) metals. These compounds, which are often called fullerides, mainly adopt crystal structures with essentially f.c.c., b.c.c. (body-centered cubic) or b.c.t. (body-centered tetragonal) symmetries. The metal atoms occupy the interstitial sites of the fullerene solid (which either have tetrahedral or octahedral symmetry) and they donate their outer electron(s) partly or completely to the C₆₀ molecules. The surrounding of a C₆₀ molecule in structures with A₃C₆₀, A₆C₆₀ and A₄C₆₀ is schematically shown in Fig. 8.

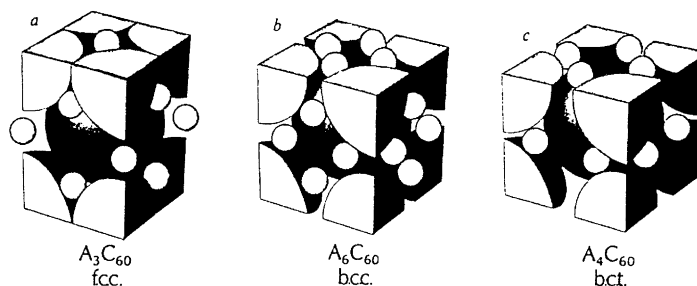


Fig. 8. Schematic representation of the mutual arrangement of the C_{60} molecules (large spheres) and the alkali ions (small spheres) in intercalated A_3C_{60} , A_6C_{60} and A_4C_{60} compounds (from Fleming et al. [66]).

Several structural phases can be found in each metal- C_{60} intercalation series which is illustrated in Fig. 9, where the K- C_{60} phase diagram is shown. At room temperature, for instance, three stable phases with stoichiometries K_3C_{60} , K_4C_{60} and K_6C_{60} are observed [67]. The most famous representatives of intercalated C_{60} compounds are the superconductors with A_3C_{60} [49–52], Ca_5C_{60} [53] or AE_4C_{60}/AE_6C_{60} [54–57] stoichiometry as well as the AC_{60} polymers [63]. These compounds are also the only metallic phases at room temperature within the C_{60} fullerenes although compounds with other stoichiometries like A_2C_{60} or A_4C_{60} should also have partly filled conduction bands. A possible explanation for this observation based upon the role played by strong electron correlation will be discussed below.

As is the case for pristine fullerenes, much less is known about intercalated higher fullerenes. The existence of several K_xC_{70} and K_xC_{84} phases has been concluded from X-ray diffraction studies of

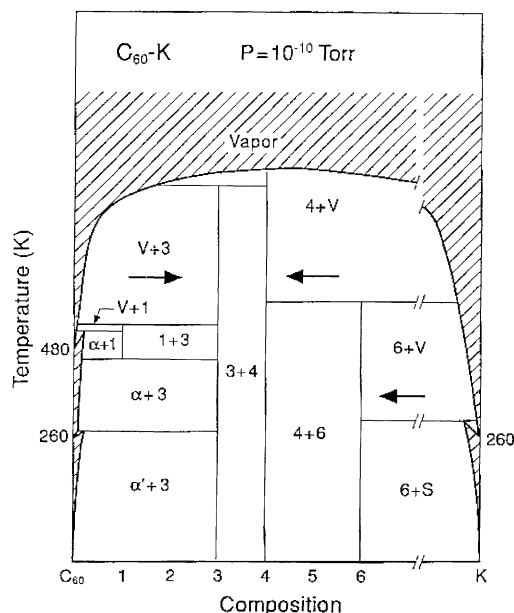


Fig. 9. Proposed phase diagram of K- C_{60} [67]. The arrows indicate the possible distillation pathways (see Section 3).

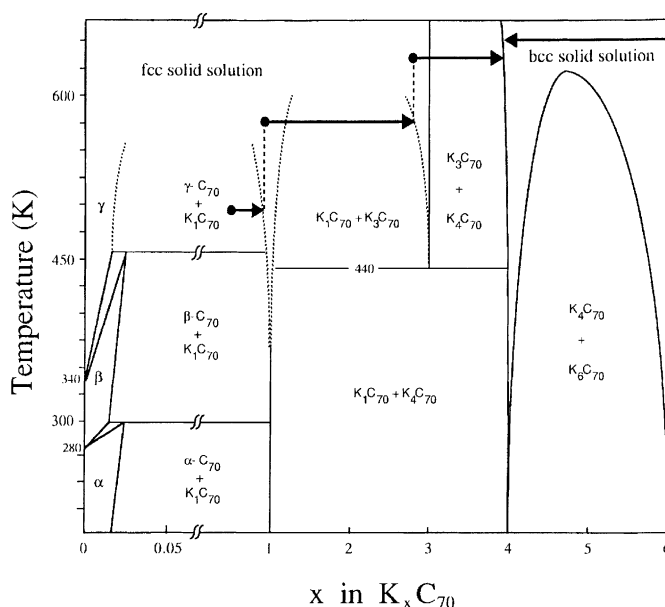


Fig. 10. Provisional phase diagram of K–C₇₀ based upon core level photoemission studies [69]. The horizontal arrows depict distillation pathways with terminal stoichiometries determined from the core level intensities (for details about the distillation process, see Section 3).

mixed phase potassium intercalated C₇₀ compounds [68] and spectroscopic investigations of thin K–C₇₀ [69] and K–C₈₄ films [70]. In the case of K–C₇₀ compounds the spectroscopic studies have helped to derive a provisional phase diagram which is shown in Fig. 10. As can be seen from Fig. 10 there are three stable intercalated phases at room temperature: K₁C₇₀, K₄C₇₀ and K₆C₇₀. In contrast to K–C₆₀ compounds, there is no K₃C₇₀ phase formed at room temperature. Higher temperatures are necessary to stabilize this phase. Instead, the K₁C₇₀ phase is present below the distillation threshold (see also Section 3). This demonstrates the profound impact which the fullerene molecular shape has on the existence of alkali intercalation compounds as a function of temperature and thus also on the variety of electronic properties that can be achieved in the corresponding A–C_n family.

In some cases, the electronic structure of alkali metal intercalated higher fullerenes has been investigated using high-energy spectroscopic techniques [20,69–76]. It is striking that, in all studies up to now, the intercalated phases of higher fullerenes prepared so far are insulators, which is in many cases in contrast to the expectations from one-electron theory. In Section 5, spectroscopic studies of the electronic structure of K–C₇₀ will be presented and discussed in more detail.

The history of heterofullerenes started in 1991 with the production of C_{60–n}B_n and C_mN_n molecules in molecular beam experiments [77,78]. The first heterofullerene which has been available in large enough amounts for solid state spectroscopic studies is C₅₉N [79]. It forms dimers ((C₅₉N)₂) and crystallizes in a lattice with monoclinic symmetry [80]. The N atoms are predicted to be in a *trans* configuration with respect to the intermolecular C–C bond and there is a closed C–N network on the ball [81]. Alkali metal intercalation of C₅₉N has also been carried out which combines two fullerene doping mechanisms at the same time (*combinational doping*). The first intercalated phase which has

been unambiguously identified is $K_6C_{59}N$, in which the dimer bonds are broken and the structure is b.c.c. analogous to that of K_6C_{60} [82].

A large variety of endohedral fullerenes have been prepared. Among others they include $He@C_{60}$ [83], $N@C_{60}$ [84] and many metallofullerenes M_xC_n which contain one or more metal ions inside the carbon cage [9]. Again, the number of solid state experiments has been limited because of the scarcity of pure endohedral fullerenes. Extended X-ray absorption fine structure (EXAFS) studies of $Y@C_{82}$ provided evidence for the endohedral nature of this material [9]. X-ray diffraction investigations showed that in $Y@C_{82}$ the Y ion does not occupy the center of the molecule but resides close to the fullerene cage [85]. The electron density distribution derived from this study indicated a charge transfer of three electrons to the C_{82} cage resulting in a $Y^{3+}@C_{82}^{3-}$ molecule in agreement with electron spin resonance measurements [86]. X-ray photoemission studies of $La@C_{82}$ suggested a La valency similar to that in $LaBr_3$ [87], whereas recent resonant PES investigations indicate a La valency of less than 3 [88]. A detailed discussion of the electronic properties of two examples of metallofullerenes, $La@C_{82}$ and $Tm@C_{82}$, will be presented in Section 7. Combinational doping can also be carried out by intercalating metallofullerene solids, and spectroscopic results on the electronic structure of $K-Tm@C_{82}$ compounds are also discussed in Section 7.

2.4. Carbon nanotubes

Carbon nanotubes are cylindrical molecules with a diameter of as little as 1 nm and a length up to many micrometers, thus one of the most perfect realizations of a one-dimensional physical object. They consist of only carbon atoms, i.e., like the fullerenes, they belong to the family of carbon nanostructures. The structure of carbon nanotubes can be thought of as a single or a few graphite layers that have been wrapped into one (single-wall carbon nanotube, SWNT) or several concentric (multi-wall carbon nanotube, MWNT) cylinders. The structure of an SWNT is schematically shown in Fig. 11. Alternatively, an SWNT can also be visualized as an ‘extended’ fullerene, where the fullerene molecule has been cut at its equator and lengthened by introducing further carbon hexagons.

Carbon nanotubes have aroused great excitement in the recent years due to their unique physical properties which span an extremely wide range [22]. For instance, nanotubes have a very low weight while exhibiting a record high elastic modulus: they are predicted to be the strongest fibers that can be made [22]. Their high strength is accompanied by their ability to buckle in a reversible manner: when a tube is bent it does not fracture but buckles like a drinking straw. When the bending strain is released,

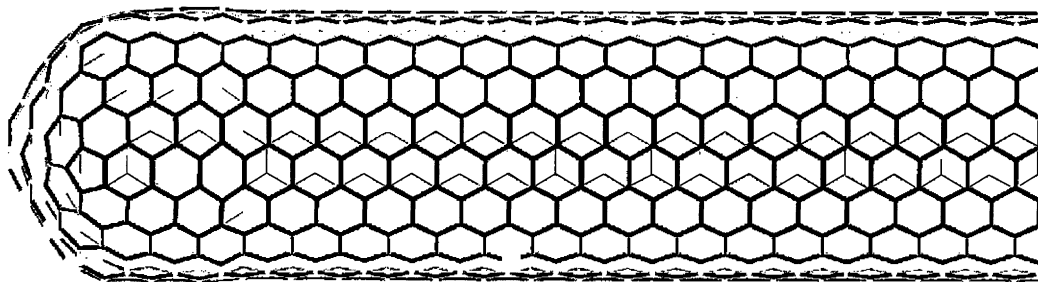


Fig. 11. Schematic representation of a (10, 10) SWNT. The diameter of such a tube is about 1.4 nm while the length usually exceeds 1000 nm.

the tube straightens out again [89]. Such remarkable mechanical properties are relevant for a number of potential applications of carbon nanotubes. Also, carbon nanotubes can act as nanocapillaries, which renders them useful for applications in catalysis or energy storage [90,91]. Moreover, the electronic properties of carbon nanotubes are also exceptional and of particular interest. Recent results on the electronic structure of SWNTs will be discussed in Section 8.

Carbon nanotubes were discovered in 1991 by Iijima [3] in electron microscopy images. He observed tubular objects during the study of fullerene soot that has been produced in an arc-discharge. They were identified as fullerene-like tubes that consist of multiple shells whereby many tubes are arranged coaxially. In 1993 it was discovered that the use of transition metals as catalyst leads to the formation of carbon nanotubes with a single shell or wall only [92,93]. The breakthrough in carbon nanotube research, however, was the discovery that SWNTs can be produced with yields up to 80% using a laser ablation technique [4]. In such a process, the tubes are formed with a narrow diameter distribution [4,94–96] and they assemble in nanotube ropes — bundles of parallel carbon nanotubes [4]. Later, it was shown that single-wall nanotubes (SWNTs) can also be produced using the arc-discharge method [97] or even chemical vapor deposition (CVD) [98] with high yields. The latter is of considerable importance as the CVD process has the potential to enable a large-scale production of carbon nanotubes as well as a growth of nanotubes at specific sites on, e.g. microfabricated chips.

SWNTs can be classified by the wrapping vector which determines the direction and distance in which the graphite layer is wrapped up and thus controls the chirality and the diameter of the nanotube. Thus, nanotubes are structurally identified by the two vector components (n, m) with respect to the graphite layer lattice vectors. This is illustrated in Fig. 12. There are two types of (n, m) carbon nanotubes that possess reflection planes and are achiral. They are called the ‘arm-chair’ (n, n) tubes and the zig-zag $(n, 0)$ tubes. All other tubes with independent n and m are chiral.

The electronic properties of carbon nanotubes are intimately connected to their structure and depend on both the diameter and chirality of the nanotube in question. A slight change in the chirality, for

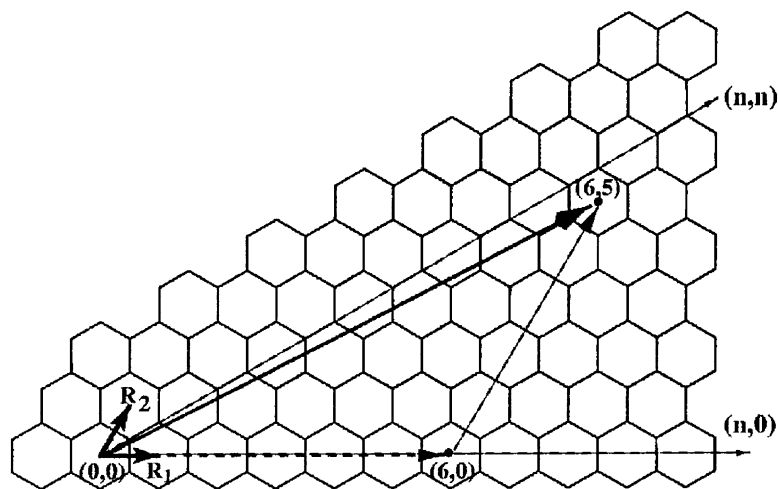


Fig. 12. Structure of the two-dimensional graphite layer which is the precursor of a nanotube. The primitive lattice vectors \mathbf{R}_1 and \mathbf{R}_2 are depicted. Carbon nanotubes can be envisaged as wrapped up graphite layers whereby the wrapping direction and distance are given by a single vector. Here, the wrapping vector $(6, 5)$ is shown for illustration (from Mintmire and White [99]).

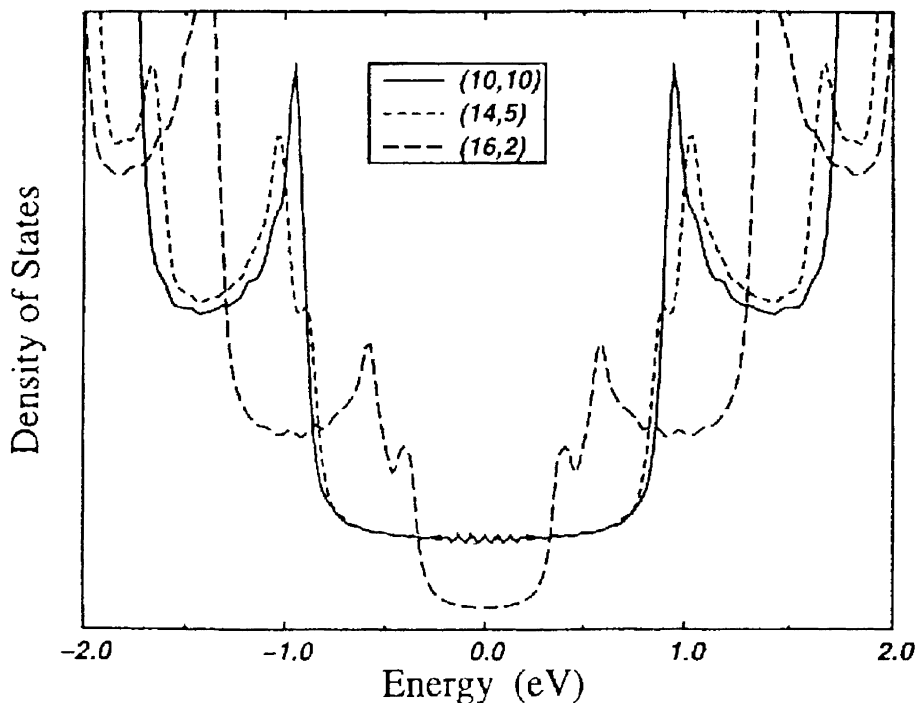


Fig. 13. Calculated electronic DOS of metallic (14, 5) and semiconducting (16, 2) chiral as well as of a metallic arm-chair tube (10, 10) using tight-binding calculations (from Ref. [102]). The Fermi level is positioned at zero energy.

instance, can transform a nanotube from a metal into a large gap semiconductor. Generally, the nanotube band structure is derived from that of a graphite layer where only discrete momenta are allowed perpendicular to the tube axis as a consequence of the one-dimensional nanotube structure [100,101]. It turns out that about one-third of the possible SWNTs are metallic; these are the nanotubes with wrapping vectors (n, m) where $n - m = 3l$ ($l = 0, 1, 2, \dots$). All other tubes are semiconductors [100,101]. An example of the electronic DOS of metallic and semiconducting tubes is presented in Fig. 13. It shows the DOS of a semiconducting (16, 2) and a metallic (14, 5) chiral tube as well as that of an arm-chair tube (10, 10) which have been derived by tight-binding calculations [102]. Fig. 13 also shows the characteristic van Hove singularities in the DOS which one would expect for a one-dimensional system such as the nanotubes. The appearance of semiconducting and metallic carbon nanotubes was predicted shortly after the discovery of the carbon nanotubes. More recently, it has also been confirmed by experiments using a scanning tunneling microscope as a spectroscopic probe [103,104]. Such experiments can directly relate structural information to the electronic DOS in the vicinity of the Fermi level of individual SWNTs. The measured DOS is remarkably similar to the results of the tight-binding calculations.

Carbon nanotubes also exhibit unique quantum wire properties that result from the small nanotube diameter in combination with the special electronic structure of graphite. Low temperature transport studies of individual SWNTs and of ropes of nanotubes lying across two metal contacts showed step-like features in the current–voltage curves whose positions depend on the voltage applied to a third

electrode that is coupled electrostatically to the nanotubes [105,106]. These features are due to single electron tunneling which is blocked at low bias as a result of the very small capacitance of the conducting nanostructure, the so-called Coulomb blockade. For nanotubes, the charging energy is in the range of 1–10 meV and single electron tunneling has been observed up to 100 K.

All the fascinating nanotube properties described above have been observed on individual nanotubes or on single ropes of nanotubes. However, studies of bulk material are also of great interest as they can provide information on the electronic properties of carbon nanotubes on a macroscopic average scale and thus complement our knowledge about this new material. One of the first studies of the electronic properties of bulk material will be described below. Finally, it should be noted that intercalation of carbon nanotube ropes with, e.g. alkali metals or halogenides is also possible [107–110] and, similar to the fullerenes, might open the door to further unexpected and fascinating properties or applications.

3. Experimental details and spectroscopic techniques

3.1. Sample preparation

The fullerene and nanotube materials for the studies described in this paper were provided by several groups world-wide. In the following the main production steps are sketched. In order to obtain pristine fullerenes, fullerene-containing soot is produced using the Krätschmer/Huffman carbon arc method [2]. Hereby, pure carbon rods are evaporated into a helium atmosphere of about 100 mbar using an arc-discharge. After extraction with appropriate solvents (e.g. toluene), the fullerenes are separated using state-of-the-art chromatography [111]. Primarily due to the small quantities involved, but also due to their chemical similarity and low solubility, the separation and isolation of different isomers of the higher fullerenes in quantities sufficient for spectroscopic studies is an important and exacting task so far achieved by only a few laboratories world-wide.

The production of the endohedral metallofullerenes also follows a modified Krätschmer/Huffman method [112], with consequent separation and isolation of the respective isomers in a multi-step chromatography process [112]. Thereby, the corresponding metal is mixed to the carbon rods as oxides or carbides. The cage symmetry of the Tm@C_{82} isomers discussed below was determined with nuclear magnetic resonance (NMR) spectroscopy and was found to be $\text{C}_{3v}(8)$, $\text{C}_s(4)$ and $\text{C}_s(6)$. The numbers in brackets give the classification according to Ref. [46]. In the case of La@C_{82} the sample consisted of a mixture of two isomers with a ratio of about 2:1. The symmetry of the majority isomer is C_2 that of the minority species is unknown [113,114].

C_{59}N is produced via an organic synthetic route which is based upon a regioselective opening of two adjacent bonds of a C_{60} molecule [115] and following reactions in acidic solution [79].

For the high-energy spectroscopic studies fullerene films are prepared by vacuum sublimation. For EELS, free standing films are produced by evaporation onto alkali-halide single crystals. After deposition of ~ 1000 Å of the fullerene material (as monitored by a quartz crystal thickness monitor), the films are floated off the substrates in distilled water, mounted on standard electron microscopy grids and transferred into the spectrometer. Prior to the energy-loss measurements the films are characterized in situ by electron diffraction. Polycrystalline fullerene films for photoemission and X-ray absorption spectroscopy of ~ 100 Å in thickness are prepared in situ by sublimation onto a clean, heated gold or copper substrate.

Similar to the fullerenes, the SWNTs used for the studies described below are produced by evaporation of carbon and metal (Ni, Co) catalyst, using a laser vaporization technique [4]. The material consists of up to 60% nanotubes with approximately 1.4 nm mean diameter and is purified as described in Ref. [116]. Free-standing films for EELS of effective thickness ~ 1000 Å are prepared on standard copper microscopy grids via vacuum filtration of a nanotube suspension in a 0.5% surfactant (Triton X100) solution in de-ionized water, with a nanotube concentration of ~ 0.01 mg/ml. The surfactant is then rinsed off and the film is transferred into the spectrometer and also characterized in situ using electron diffraction.

Intercalation of the fullerenes is carried out under ultra-high vacuum (UHV) conditions (base pressure 10^{-10} mbar) by evaporation either from a commercial SAES getter source (alkali metals, Ba) or from a resistively heated tungsten boat (Ca). During intercalation, the fullerene film is maintained at elevated temperature (400–470 K) to promote intercalant homogeneity and to improve the grain size of the resultant fulleride film. An additional post-anneal at higher temperature (up to 620 K) may also be used for the same purpose. Phase-pure fulleride samples can be prepared using vacuum distillation, in which either the fullerene or the intercalant is preferentially evaporated from the sample held at elevated temperature in UHV, such that the stoichiometry of a nominal starting composition approaches that of the desired phase. This technique has been shown to be highly effective in the preparation of phase-pure fulleride thin film samples [66,67,117,118].

Fig. 14 illustrates one example of the results of such distillation experiments for K_xC_{70} compounds [69]. The data points represent measured compositions as a function of time at the temperatures indicated. The lines were added as a guide to the eye. The bottom curve shows the changes in composition of an 800 Å thick film, that had an initial stoichiometry of $K_{0.5}C_{70}$, as it was held at 495 K in vacuo, then at 575 K and finally at 635 K. The measured compositions at saturation are very close to K_1C_{70} , K_3C_{70} and K_4C_{70} . The final compositions represent phase boundaries at the given distillation temperature. In Fig. 14 the increase in relative K content indicates that C_{70} evaporates preferentially when the stoichiometry is below 4. In contrast, the relative K content can be reduced by distillation of a saturated K_6C_{70} film. In this case heating to 650 K produces K_4C_{70} , as can be seen in the top curve. The fact that K_4C_{70} is reached by distilling from either higher or lower stoichiometry indicates that this

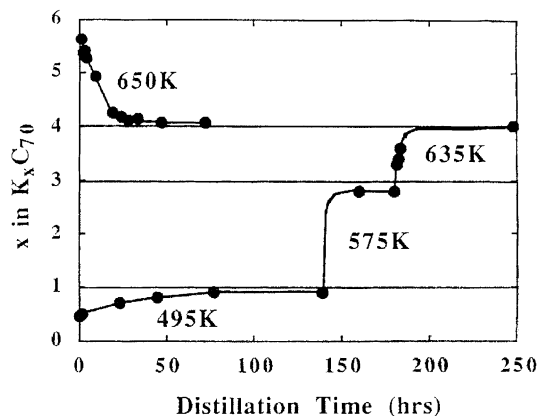


Fig. 14. Summary of results obtained during distillation of samples of initial stoichiometry of $K_{0.5}C_{70}$ and K_6C_{70} at the temperatures given [69].

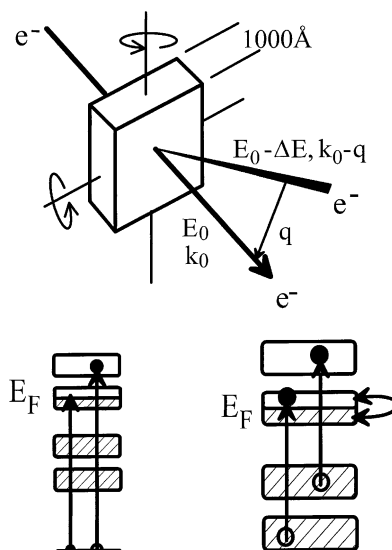


Fig. 15. Scattering geometry of an electron energy-loss experiment in transmission (upper panel). The inelastically scattered electrons deposit both energy, ΔE , and momentum, q , in the sample. Depending upon the energy-loss, core electrons (lower left-hand panel) or valence/conduction band electrons (lower right-hand panel) can be excited into unoccupied states.

compound is the most stable in the K–C₇₀ series against sublimation. K₄C₇₀ can also be sublimed, but this occurs stoichiometrically. At 675 K the sublimation rate is ~ 0.2 monolayers/h.

3.2. Electron energy-loss spectroscopy

In an electron energy-loss experiment in transmission, high-energy electrons with a primary energy larger than about 30 keV are transmitted through samples which have a thickness of about 1000 Å. Inelastically scattered electrons are detected and the respective energy-loss corresponds to excitation energies of the solid. The scattering geometry and the possible excitations are schematically drawn in Fig. 15. The electrons are scattered by a finite scattering angle which corresponds to a momentum transfer to the solid.

The quantity measured in EELS is the loss function, $\text{Im}(-1/\epsilon(q, \omega))$, which provides information on the excitations of the system and after a Kramers–Kronig analysis (KKA), yields the real and imaginary parts of the dielectric function, $\epsilon_1(q, \omega)$ and $\epsilon_2(q, \omega)$, respectively. For energy-losses below ~ 50 eV, the loss function essentially describes collective plasmon excitations of the system which can arise from intra- and interband transitions. As regards interband transitions, which will play a dominant role in the discussions below, the excitation energy of the related plasmon E_p is given by the interband transition energy E_0 and the oscillator strength ω_p of the transition [119]:

$$E_p^2 = E_0^2 + \hbar^2 \omega_p^2. \quad (4)$$

At higher energies, the loss function describes transitions from core or shallow core levels into unoccupied states derived from orbitals of the same atom. Such core excitations are governed by the dipole selection rule, thus, e.g., excitations from the C1s core level of a carbon atom will give a picture

of the unoccupied C2p-derived DOS at that site. If the effect of the resultant core hole was negligible, this would give a direct measure of the transition matrix element weighted site and symmetry specific unoccupied density of electronic states (DOS). The presence of the core hole, however, and its interaction with the excited electron system leads to changes of the electronic levels in the excited states. These changes can be visualized by introduction of an impurity with a nuclear charge which is larger by one and which simulates the core hole (the so-called $Z + 1$ approximation) [120]. Calculations of the C1s core hole interaction for several carbon-based systems indicate that the core hole causes an excitonic excited state below the conduction band threshold with a spectral shape that does not reflect the undisturbed conduction band (e.g. Ref. [121] and references therein). This has also been shown in detail for the fullerene molecules C_{60} and C_{70} [122]. The spectral intensity, however, is much less affected by the core hole interaction, i.e. it still gives a good measure for the occupancy of the unoccupied states which will be utilized in the discussion below.

A more detailed description of the operation and principles behind EELS experiments can be found in Ref. [119]. Information analogous to that obtainable from EELS in the low energy region is provided by optical spectroscopy (although only with zero momentum transfer), and in the high-energy region from X-ray absorption spectroscopy (XAS, see below). Furthermore, as the EELS cross-section is also proportional to the dynamic structure factor $S(q, \omega)$, one can gain information on the spatial extension of electronic excitations via momentum dependent measurements provided that the excitations are of pure multipole character (e.g. pure dipole excitations). This has been utilized recently for a number of finite-size π conjugated systems [123–126] and is outlined in the following. The matrix element, M , for EELS is proportional to $\langle f | \exp(iqr) | i \rangle$ which can be expanded to

$$M \propto \sum_n \frac{i^n}{n!} (q\langle r \rangle)^n \langle f | \left(\frac{r}{\langle r \rangle} \right)^n | i \rangle. \quad (5)$$

Hereby, the introduction of an effective radius $\langle r \rangle$ allows one to separate the characteristic dimensionless $(q\langle r \rangle)$ -dependence of the matrix element from the (now also dimensionless) q -independent excitation probability $\langle f | (r/\langle r \rangle)^n | i \rangle$. In the case of excitations with a *specific* multipole character (e.g. dipole excitations) the latter has a finite value only for the corresponding n (e.g. $n = 1$). Thus, the momentum dependence of the excitation intensity I_n ($\propto |M|^2$) of an excitation with a *specific* multipole character can be written as

$$I_n \propto \frac{n!^{-2} (q\langle r \rangle)^{2n}}{N}, \quad N = \sum_n \frac{(q\langle r \rangle)^{2n}}{n!^2}. \quad (6)$$

N is a sum over the intensities of all excited (final) multipole contributions and represents a normalization factor which guarantees the oscillator strength sum rule.

In Fig. 16 the intensities I_n as a function of $q\langle r \rangle$ are shown for $n = 1-4$. Maxima are found at $q\langle r \rangle = 0, 2.2, 3.2$ and 4 for $n = 1-4$, respectively. A comparison of the curves in Fig. 16 and the momentum dependent intensity variation of an excitation now allows the determination of the effective radius of this excitation. This will be discussed below in detail for the lower lying excitations of C_{60} .

For the valence level excitations and elastic scattering (electron diffraction) data shown here, the momentum resolution of the EELS spectrometer was set to 0.05 \AA^{-1} with an energy resolution of about 120 meV. The core level excitations were performed with a momentum and energy resolution of 0.15 \AA^{-1} and 160 meV, respectively. All EELS experiments were conducted at room temperature.

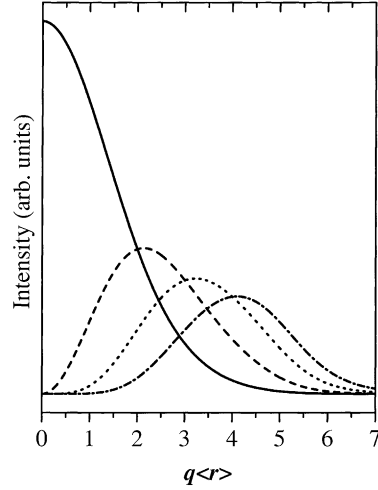


Fig. 16. Intensity of the n th multipole excitation according to Eq. (6) ($n = 1$: solid line, $n = 2$: dashed line, $n = 3$: dotted line, $n = 4$: dashed-dotted line).

3.3. Photoemission spectroscopy

Photoemission is widely used in the study of the electronic structure of solids (see, e.g. Ref. [127]). It utilizes the photoelectric effect in which an electron is ejected from the occupied electronic levels of the sample. The geometry of a photoemission experiment is schematically shown in Fig. 17. The photoelectron flux resulting from the absorption of monochromatic light as a function of the final state (kinetic) energy is a measure of the energy distribution of the $(N - 1)$ electron states (where N is the number of electrons in the ground state). This is also known as the electron removal spectrum. For non-correlated systems and non- k -resolved measurements this quantity is equivalent to a matrix element weighted measure of the occupied DOS. Otherwise, the photocurrent in a photoemission experiment, j , is proportional to the so-called spectral function $A(k, \omega)$ which represents the imaginary part of the fundamental, many-particle Green's function $G(k, \omega)$ of the electron system [127]:

$$j(k, \omega) \propto A(k, \omega) = \frac{1}{\pi} \text{Im}[G(k, \omega)]. \quad (7)$$

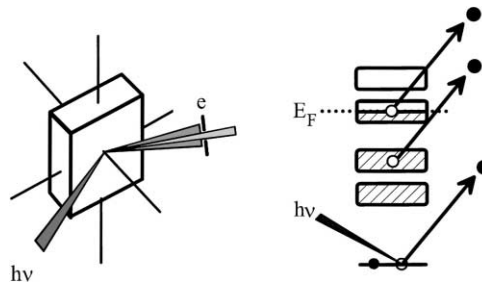


Fig. 17. Scattering geometry of a photoemission experiment (left-hand panel). Depending upon the photon energy, $h\nu$, electrons from core levels or valence/conduction band states are ejected (right-hand panel).

For independent particles, the Green's function is given by the single particle energies $E(k)$:

$$G_0(k, \omega) = \frac{1}{\hbar\omega - E(k) + i\delta}. \quad (8)$$

The effect of the interaction of the particles (the formation of quasi-particles) can be expressed by the so-called complex self-energy $\Sigma(k, \omega)$ which describes both the change of the quasi-particle energy in comparison to the non-interacting case (real part of Σ), as well as the finite lifetime of the quasi-particles due to the interaction (imaginary part of Σ):

$$G(k, \omega) = \frac{1}{\hbar\omega - E(k) - \Sigma(k, \omega) + i\delta}. \quad (9)$$

Σ not only contains the effects of electron–electron interaction but also describes the consequences of other interactions like electron–phonon coupling, which can give rise to satellites in the photoemission spectrum and an altered lifetime of the quasi-particle states.

In a photoemission experiment, the kinetic energy of the photoelectrons usually varies from a few electron volts up to a few hundred electron volts, depending on the photon energy, $h\nu$, used. This results in the surface sensitivity of the technique, as the inelastic mean free path of a typical photoelectron in the solid is in the range of 5–30 Å. This means that UHV is necessary to maintain a surface free of adsorbates during the timescale of the measurement, and that the effect of the surface should be borne in mind during the interpretation of the resulting spectra. The photoemission experiments presented here were carried out using a hemispherical electron analyzer, together with a noble gas discharge lamp providing radiation at an energy of 21.22 eV for operation with He, an X-ray source providing monochromatized Al K α radiation (1486.6 eV) or synchrotron radiation.

3.4. X-ray absorption spectroscopy

The unoccupied electronic structure of a solid can be probed using X-ray absorption spectroscopy, the principle of which is shown in Fig. 18. In an XAS experiment monochromated photons of energy $h\nu_1$ impinge on a sample and are absorbed. If the photon energy is high enough, there exists the possibility of the excitation of core level electrons into unoccupied states of the solid. This is measured indirectly via the decay of the corresponding excitation giving rise to fluorescence light ($h\nu_2$) or Auger

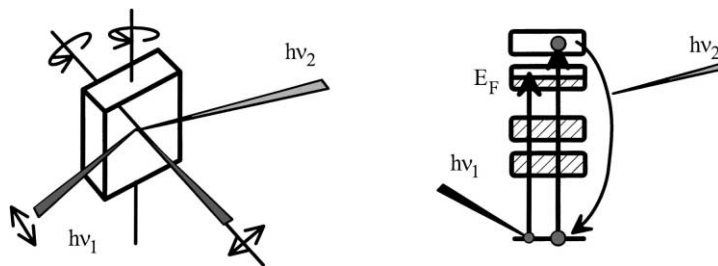


Fig. 18. Scattering geometry of an X-ray absorption experiment (left-hand panel). Linearly polarized photons of energy $h\nu_1$ are absorbed in the sample which results in the excitation of core electrons into unoccupied states (right-hand panel). The absorption process is monitored indirectly either by measuring the fluorescence light ($h\nu_2$) or Auger electrons which are created by the decay of the corresponding excitation.

electrons, whose intensity is proportional to the absorption cross-section. Since dipole selection rules apply for light absorption, only states with an angular momentum $L \pm 1$ can be reached, where L is the angular momentum of the respective core level. Thus, XAS is equivalent to core level EELS studies which are described in further detail above. Again, as long as core exciton effects are small, the matrix element weighted, site and symmetry specific unoccupied DOS is probed. For more information about this technique, see Ref. [120].

The XAS measurements presented here are conducted using monochromatized synchrotron radiation from the PM5 monochromator at the Berliner Elektronenspeicherring für Synchrotronstrahlung (BESSY) [128]. All experiments are carried out at room temperature and the total electron yield method is applied to monitor the absorption at the corresponding absorption edges.

4. Pristine fullerenes: from C_{60} to C_{84}

The photoemission profiles at room temperature of C_{60} [129], C_{70} [130], the two C_{2v} isomers of C_{78} [131] and C_{84} [132] are shown in the left-hand panel of Fig. 19. The data are representative of other data in the literature [31,71,133–135]. The notation of the C_{78} isomers follows Ref. [46]. The structures closest to the chemical potential (binding energy = 0 eV) arise from the HOMO of the corresponding fullerene followed by deeper lying electronic states (HOMO-1, HOMO-2, etc.). Below about 6 eV binding energy (BE) the σ -derived states additionally contribute to the photoemission spectra. The sharpness of the structures demonstrates that upon solid formation the electronic states remain relatively unchanged. This is also indicated by the close similarity of the C_{60} PES data shown in Fig. 19 to those from gas phase measurements [136]. There is an overall similarity of the occupied electronic structure of the fullerenes shown in Fig. 19 which is an expression of the similarity between the molecular structures of the different members of the fullerene family. In detail, however, the profiles are significantly different, most clearly in the π -derived structures at low BE, which is a result of the individual fullerene geometry. The lower degeneracy of the electronic states due to the lower molecular symmetry of the higher fullerenes, for instance, leads to a larger width and a splitting of the features

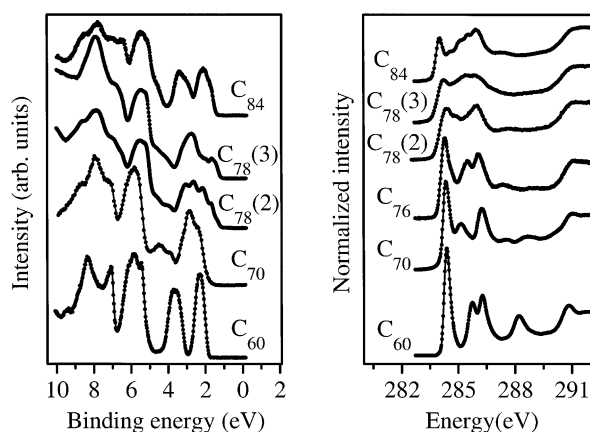


Fig. 19. Left-hand panel: the PES spectra of solid C_{60} , C_{70} , C_{78} and C_{84} . Right-hand panel: C1s excitation spectra of thin films of C_{60} , C_{70} , C_{76} , C_{78} and C_{84} . The spectra in each case are offset in y-direction.

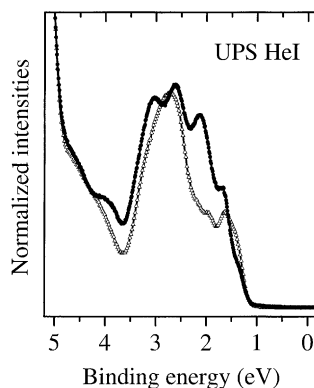


Fig. 20. Comparison of the photoemission profiles of the two C_{78} isomers with C_{2v} symmetry: $C_{78}(2)$ circles and $C_{78}(3)$ open triangles.

observed. Moreover, even very small variations in the molecular structure have considerable impact on the relative energy position of the lowest lying electronic levels. This is demonstrated in Fig. 20 which focuses on the photoemission spectra of the two isomers of C_{78} [131]. Both have the same number of carbon atoms and the same C_{2v} symmetry and their molecular structure is directly related through a Stone–Wales transformation: a rotation of one C–C unit by 90° [137]. Therefore, for a molecule of this size one would naively expect a very similar electronic structure, in contrast to what is shown in Fig. 20. Generally, the spectrum is more structured for the $C_{78}(2)$ isomer although the electronic states are non-degenerate for both isomers due to the relatively low symmetry. The data indicate an almost equidistant relative energy position of bundled electronic levels for $C_{78}(2)$, whilst in $C_{78}(3)$ the levels are spread over a wide energy range except the clearly separated first features at about 1.5 eV BE. In agreement with this experimental result, such a tendency has also resulted from tight-binding and LDA calculations of the electronic levels of the different C_{78} isomers [138,139].

High resolution PES has also been applied in order to study temperature-dependent variations of the electronic structure, i.e. the impact of the rotational phase transitions on the electronic states. While for C_{60} and C_{84} no changes could be observed [129,132], the electronic structure of C_{70} was found to be significantly dependent upon temperature changes across the phase transitions [31]. This difference arises from the elliptical structure of C_{70} , with D_{5h} symmetry while C_{60} and also C_{84} are much more spherical in shape.

In Fig. 21, the valence band structures of C_{70} measured between 40 and 360 K are depicted. The uppermost curve represents the gas-phase photoemission results of Ref. [140]. The spectrum obtained at 360 K shows clearly resolved features at 2, 2.6, 2.9, 3.5 and 4.2 eV BE. Comparison to the gas-phase data reveals a one-to-one correspondence in features, but also changes that are evident upon condensation, and then again upon cooling through the phase transitions at about 280 and 340 K. Above 340 K the molecules rotate freely; their long axes become aligned below 340 K but they still can rotate about this axes and below 280 K all rotation is hindered. The most obvious changes in Fig. 21 are seen in the features at 2 and 3.5 eV. The structure at 3.5 eV is distinct in the high temperature phase but it is barely distinguished at 40 and 220 K. The feature at 2 eV increases in relative intensity on going from 360 to 40 K. These changes result from the orientational phase transitions which lead to significant lattice constant changes and molecular ordering in solid C_{70} and thus to a significant change in the

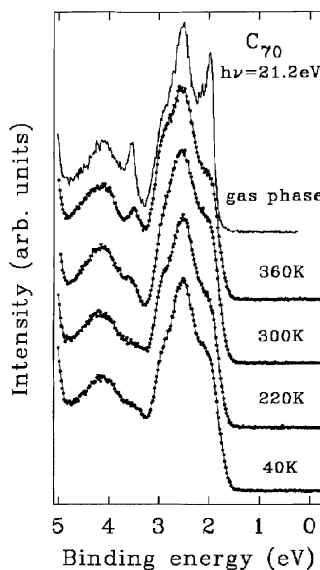


Fig. 21. Photoemission spectra of solid C_{70} near the Fermi energy as a function of temperature. The gas-phase spectrum is reproduced from Ref. [140] for comparison. Condensation of molecules into the randomly tumbling high temperature phase produces solid-state broadening of the leading orbitals. Upon cooling further broadening of the spectral features is observed which indicates increased overlap of the molecular orbitals.

intermolecular orbital overlap [31]. The stronger the orbitals overlap at lower temperatures the broader the spectral features become which is a direct sign for increasing valence bandwidths at low temperatures. The lattice changes and thus also the changes in the electronic structure in the case of C_{60} and C_{84} are considerably smaller.

In the right-hand panel of Fig. 19 the C1s excitation spectra of C_{60} [73], C_{70} [73], C_{76} [45], the two C_{2v} isomers of C_{78} [131] and C_{84} [132] are depicted. The features below 290 eV are caused by transitions into π^* -derived electronic states. The step-like structure at about 290.5 eV corresponds to the onset of transitions into σ^* -derived unoccupied levels. Although the core level interaction alters the spectral information (see Section 3), the spectra shown in Fig. 19 represent transitions into unoccupied molecular orbitals as these orbitals are energetically well separated and the core hole induced changes in spectral shape are smaller than the energy distance of the orbitals near the excitation threshold [142]. Consequently, the first feature at about 284.5 eV represents transitions into the LUMO of the corresponding fullerene. The data shown for C_{60} are similar to those obtained using XAS and inverse photoemission [134,141]. As was the case for the occupied electronic states, the overall similarity between the different fullerenes and the broadening towards higher fullerenes is also visible for the unoccupied part of the electronic structure. The energy onset of the C1s excitation decreases with increasing fullerene size which can be ascribed to the decrease in curvature and concurrent increase of the C2p contribution to the π -derived states as the larger fullerenes become more graphitic. The decrease in intensity of the first feature reflects the lower orbital degeneracy for the higher fullerenes. Again, there is a clear difference between the C1s excitation spectra of the two C_{78} isomers, which shows that both the occupied and the unoccupied electronic states near the chemical potential are closely related to the details of the molecular geometry.

There has been a number of comparisons of the experimental results with theoretical predictions for the electronic structure of fullerenes [18,129,133]. The overall agreement is rather good but important discrepancies are found, especially as regards the band gap and the bandwidth of the HOMO- and LUMO-derived bands. Furthermore, fine structure in the DOS as it is reported from calculations is not observed in the experiments. Most of the discrepancies result from the fact that electron spectroscopic techniques do not probe the electronic ground state of the system studied. Instead, they leave the system in an excited state, e.g. PES probes the $(N - 1)$ state. This gives rise to relaxation processes which can make themselves felt in the appearance of satellites in the spectra. A significantly improved agreement between theory and experiment is obtained when one takes into account such relaxation processes as was done for C_{60} using the GW approximation [143]. Within such an approach the calculated bandwidth of the HOMO-derived bands of about 1 eV and the PES–IPES gap are much closer to the experimental results.

Information about the optical properties and the dielectric function of pristine fullerenes have been obtained by measuring the loss function and performing a KKA. Fig. 22 shows the loss function, $\text{Im}(-1/\epsilon)$, and the real and imaginary parts of the dielectric function, ϵ_1 and ϵ_2 , of solid C_{60} for a small momentum transfer of $q = 0.1 \text{ \AA}^{-1}$ [73]. At such small q the results are equivalent to those obtained in optical experiments, thus dipole selection rules apply. Similar to the case of graphite or conjugated polymers [119], the loss function is dominated by two main features at about 6 and 25 eV, the so-called π and $\pi + \sigma$ plasmons. They are due to a collective excitation of only the π or of all valence electrons, respectively. The features which can be observed at energies lower than 6 eV arise from interband transitions between the occupied and unoccupied π -derived electronic states and the shoulders between 8 and 25 eV are due to transitions that involve σ -derived states. The sharp structures below 6 eV again demonstrate the highly molecular nature of the electronic states of C_{60} . At zero energy, the real part of the dielectric function, ϵ_1 , has a value of about 4, i.e. the refractive index, n , of C_{60} is $n = \sqrt{\epsilon_1} = 2$. The imaginary part, ϵ_2 , has its spectral onset at about 1.8 eV which is the optical gap of solid C_{60} . These values are in good agreement with results from optical studies [13].

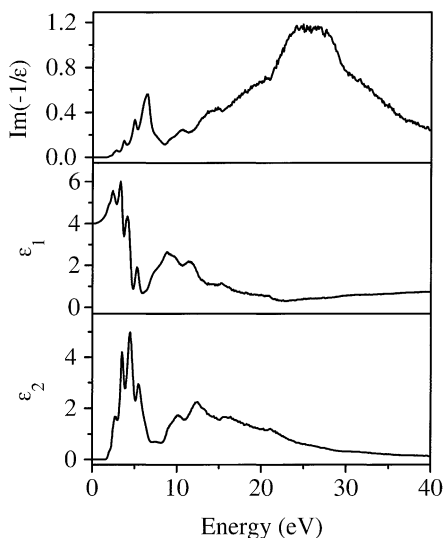


Fig. 22. Loss function, $\text{Im}(-1/\epsilon)$, real and imaginary parts of the dielectric function, ϵ_1 and ϵ_2 , of solid C_{60} .

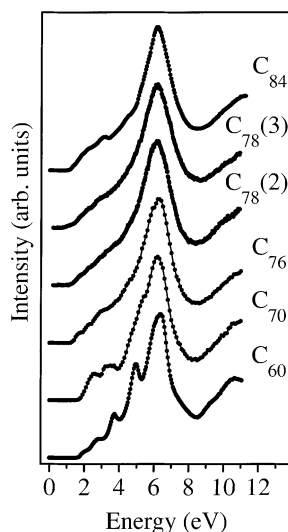


Fig. 23. The loss function, $\text{Im}(-1/\epsilon)$, of thin films of C_{60} , C_{70} , C_{76} , the two C_{2v} isomers of C_{78} and C_{84} . The curves are normalized to have equal π plasmon intensities and are offset in the y-direction.

In Fig. 23, we show a comparison of the loss functions of C_{60} [73], C_{70} [73], C_{76} [45], the two C_{2v} isomers of C_{78} [131] and C_{84} [132] up to 12 eV. The overall structure of the loss functions is rather similar for all the fullerenes shown. The spectral onset displays a tendency to lower energies, i.e. the optical gap generally decreases with the size of the fullerene molecules. This can be understood taking into consideration the addition of more hexagons into the carbon network which means that the higher fullerenes become increasingly ‘graphitic’. The end member of this development would be a graphene sheet which is a zero-gap metal. In addition, the fine structure in the loss function is washed out going to higher fullerenes which again is a consequence of the lower orbital degeneracy. Deviations from these general trends are, however, also observable in the loss functions. For example, the onsets for the two C_{78} isomers differ, the exact values being 0.7 and 0.85 eV for $\text{C}_{78}(3)$ and $\text{C}_{78}(2)$, respectively, which is a further confirmation of the result that the details of the electronic structure are nevertheless very sensitive to small variations of the molecular geometry.

In contrast to optical measurements, EELS offers the possibility to determine the dielectric properties as a function of momentum transfer, q . As discussed above, this renders it possible to gain information on the spatial extension of the electronic excitations provided the excitations are of pure multipole character, which is true for the highly symmetric C_{60} molecule. In Fig. 24 the optical conductivity, σ , of C_{60} is shown between 0.6 and 3.2 eV for various momentum transfers [124]. The optical conductivity has been derived performing a KKA of the loss function [144]. In Fig. 24 strong intensity variations with increasing momentum transfer are visible. At low momentum transfers the spectrum consists of a small shoulder at about 2.1 eV and two further structures located at about 2.45 and 2.8 eV. While the 2.1 eV shoulder develops into a clear peak with increasing momentum transfer the intensity of the two higher lying excitations decreases. At a momentum transfer of about 0.8 \AA^{-1} the feature at 2.1 eV reaches its maximal intensity before it starts to decrease again, whereas the other two structures show the opposite behavior. The momentum dependent intensity variation of the electronic excitations is also shown in Fig. 24 (right-hand panel).

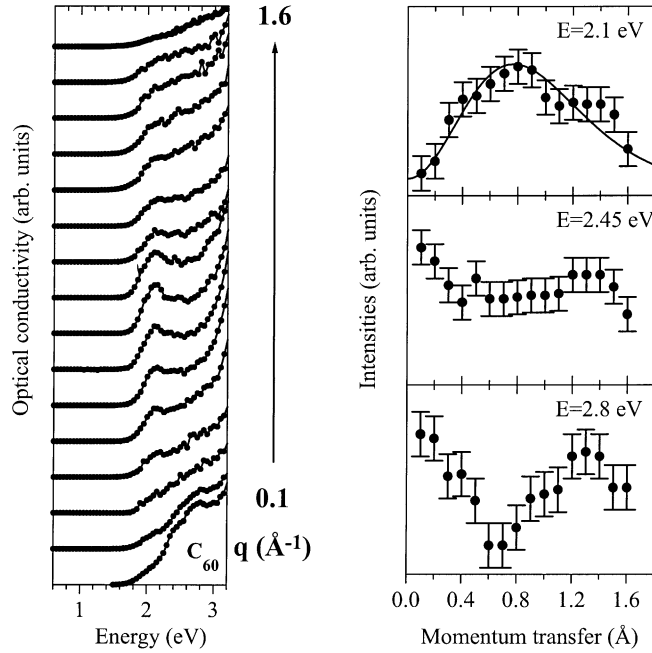


Fig. 24. Left-hand panel: low energy optical conductivity σ of C_{60} as a function of momentum transfer q in steps of 0.1 \AA^{-1} . The curves are offset in y-direction. Right-hand panel: the experimentally determined intensity variation of the gap excitation (upper panel) and the following electronic excitations (middle and lower panel) of C_{60} as a function of momentum transfer q . The excitation energies are given in the corresponding panel. The solid line in the upper panel represents the theoretical expectation for a quadrupole excitation with an effective radius of 2.8 \AA (see also Fig. 16).

As expected, the gap transition at 2.1 eV clearly shows the behavior of a dipole forbidden excitation. The EELS response function in the gap region is almost solely caused by the gap multiplet component having 1H_g symmetry because it can be reached via an electric quadrupole transition while the other multiplet components with $^1T_{1g}$, $^1T_{2g}$ and 1G_g symmetry can only be reached via magnetic dipole or even higher order transitions [60]. Consequently, a comparison of the intensity variation of the gap transition shown in Fig. 24 with Fig. 16 gives a direct measure of the effective radius of the 1H_g excitation of $\langle r \rangle \sim 2.8 \text{ \AA}$. This value is somewhat smaller than one would expect for the mean distance \bar{d} of two particles moving independently on a sphere with the radius, R , of a C_{60} molecule which is $\bar{d} = (4R_{C_{60}}/\pi) \sim 4.5 \text{ \AA}$. This might indicate that the electron-hole pair is excitonic in agreement with other results and predictions [30]. From the effective radius one can also derive an estimate for the exciton BE, E_B :

$$E_B \sim \frac{1}{4\pi\epsilon_0\epsilon_r} \frac{e^2}{\langle r \rangle}, \quad (10)$$

which is screened by the static dielectric constant ϵ_r (~ 4 for C_{60}). This simple consideration leads to a BE, E_B of about 1.3 eV also in good agreement with other results [30].

Moreover, the fact that the 1H_g excitation dominates the EELS response function in the region of the energy gap yields a direct experimental access to its excitation energy which can be derived from the first maximum in Fig. 24 to be 2.1 eV. Together with optical studies of the other multiplet components

[145] one can determine the total width of the gap excitation multiplet of C_{60} to be about 260 meV [124]. Thus, the multiplet width of the gap transition of C_{60} is significantly smaller than predictions from calculations which range from about 400 to 600 meV [146,147]. This indicates that, independent of the exact approach, the models used to describe the electronic excitations of C_{60} (and other π electron systems) tend to overestimate electron interaction effects.

The q -dependent intensity changes of the excitations visible at about 2.45 and 2.8 eV are also shown in the right-hand panel of Fig. 24. The excitation occurring at 2.45 eV does not show any significant momentum dependence which suggests that it is not of a pure multipole but of mixed character. Since intra-molecular excitations in C_{60} can all be classified as either *gerade* or *ungerade*, the electronic excitation appearing at 2.45 eV in C_{60} can be attributed to a charge transfer excitation resulting in the final state hole and electron sitting on different molecules [124]. In contrast, the spectral weight of the excitation at 2.8 eV decreases with increasing momentum transfer which is consistent with a dipole allowed molecular Frenkel excitation. The assignment of the two excitations at 2.45 and 2.8 eV to charge transfer and Frenkel excitons, respectively, is in agreement with a comprehensive analysis of the excited states of C_{60} using optical absorption and luminescence spectroscopy, electroabsorption studies and photoconductivity [148]. It is also qualitatively in line with theoretical calculations [147] which predict the charge transfer excited states to occur about 150 meV above the 1H_g excitation.

It is interesting to compare the gap value derived from EELS (or optical) experiments to those determined in combined measurements using PES and inverse PES (IPES). In EELS at high primary energies one can only make excitations resulting in singlet states [119]. The triplet excitation corresponding to the HOMO–LUMO transition in C_{60} has been found to be at about 1.5 eV using low energy EELS experiments in reflection [149], where exchange processes render triplet excitations accessible. In the PES–IPES studies, however, a gap value of about 2.3 eV has been observed [30,150]. The latter measurements probe the real transport gap as a photoemission experiment removes an electron from the valence band while in IPES an electron is added to the conduction band. Thus, the gap excitation in EELS corresponds to the formation of a Frenkel exciton which is mainly localized on a C_{60} molecule as discussed above. The Coulomb repulsion U for two holes located on the same C_{60} molecule is of the order of 1.5 eV [30]. It is this relatively large value of U in comparison to the bandwidth which results in exciton formation, and means that the energy penalty paid for the creation of separate $(N - 1)$ and $(N + 1)$ states is not equal to the simple splitting in energy between the HOMO and LUMO. The energy separation of the HOMO and LUMO in C_{60} can be estimated from the separation of the corresponding levels in solid K_6C_{60} which is ~ 1.7 eV (see Section 5, although the non-rigid band-like changes of the electronic structure upon intercalation also play a role here).

Excitons also play a role in the low energy excitation spectra of the higher fullerenes. In Fig. 23, for each of the fullerenes measured, the gap from EELS in the solid state is similar to that observed in solution, and is significantly smaller than the transport gap derived from PES–IPES data [45]. Furthermore, the Coulomb repulsion energy U for two holes on a C_{70} molecule is large enough to expect similar excitonic effects as in for C_{60} . Fig. 25 shows a comparison of the fine structure of the C KVV Auger spectrum of C_{70} with a self-convoluted valence band photoemission spectrum (see Fig. 19) [31]. The Auger spectrum corresponds to a state where there are two interacting holes on a C_{70} molecule while the self-convoluted photoemission spectrum represents the case of two independent, non-interacting holes. In order to obtain the feature-to-feature correspondence as shown in Fig. 25, the self-convoluted photoemission spectrum has to be shifted by 1 eV to higher BE. This 1 eV shift gives a measure for the effective Coulomb repulsion of two holes on C_{70} in the solid. This value represents an

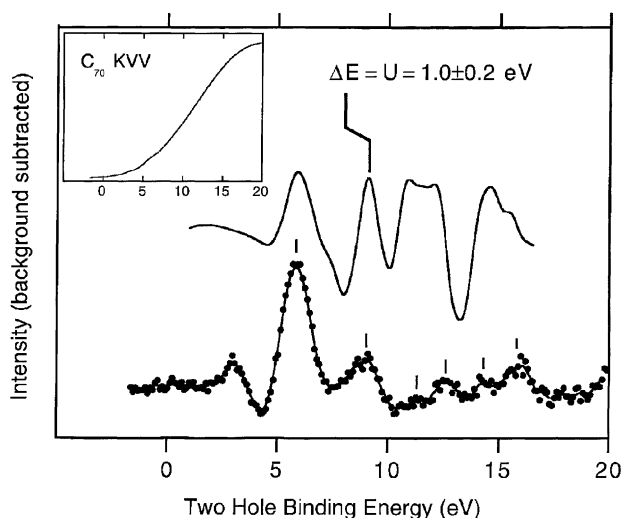


Fig. 25. Comparison of the C KVV Auger spectrum of C_{70} (filled circles) with a self-convoluted valence band photoemission spectrum (solid line) after the subtraction of smooth backgrounds (see Ref. [31]). The energy shift needed to achieve optimal peak alignment corresponds to the on-site Coulomb repulsion, U . The inset shows the Auger spectrum before background subtraction.

average measure of U since the interaction between two holes depends on the specifics of the molecular orbitals that are involved. The result for the Coulomb repulsion U of 1 eV is in agreement with what can be deduced from combined photoemission and inverse photoemission studies [31]. Furthermore, taking into consideration the electron affinity $E_A = 2.8$ eV and the ionization potential $E_I = 7.47$ eV from gas phase measurements [140,151] one obtains a repulsion energy for an isolated C_{70} molecule of $U = E_I - E_A - \Delta = 3.1$ eV, where Δ is the energy splitting of the HOMO and LUMO in the ground state ($\Delta \sim 1.6$ eV [151]). In the solid, U is further screened by the polarization of the neighboring molecules [30] to its value of about 1 eV [31].

5. Intercalated fullerenes

5.1. Alkali metal intercalation

5.1.1. A_xC_{60} ($x = 0, \dots, 6$)

In this section, we will present spectroscopic results of A_xC_{60} (A = alkali metal) compounds which are representative of intercalation with alkali metals for $x \leq 6$. Thereby, only those compounds are discussed that are composed of individual C_{60} molecules at room temperature, i.e. the polymer phases with AC_{60} [63] or Na_4C_{60} [64] stoichiometry are not considered. In Fig. 26, we show the photoemission results [129,152] and the C1s excitation edges [153,154] for C_{60} , K_3C_{60} , K_4C_{60} and K_6C_{60} , the K- C_{60} phases that are stable at room temperature (see Fig. 9). The spectrum labelled α - C_{60} in the left-hand panel was recorded from a sample which had been exposed to a very low flux of K atoms, which results in a highly dilute solid solution of potassium in C_{60} . The Fermi level in this case is pinned at donor

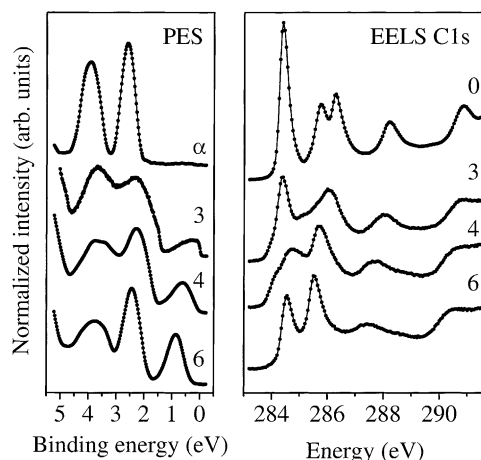


Fig. 26. Left-hand panel: PES spectra ($h\nu = 21.22$ eV) of K_xC_{60} ($x = 3, 4, 6$) compounds normalized to the C_{60} HOMO-derived spectral weight (for ‘ α ’, see text). Right-hand panel: C1s excitation edges of the same compounds. The data are normalized to the σ^* onset at about 290 eV.

levels near the base of the LUMO-derived bands, thus causing a shift of the spectrum to higher BE in comparison to the spectrum of pristine C_{60} shown earlier. Upon intercalation the charge transfer of electrons to the C_{60} molecules is clearly revealed by the presence of a new feature located in the former gap. This is the partly or completely filled band formed from the triply degenerate molecular LUMO. For K_3C_{60} a considerable DOS at the Fermi level and a clear Fermi cutoff are visible indicating the metallic ground state for this compound. On further intercalation to $x \sim 4$ the LUMO-derived peak has grown further and shifted away from the Fermi level (E_F), resulting in small or zero intensity at E_F . By $x = 6$, the LUMO-derived band is completely full and there is a clear gap between the highest occupied states and E_F . The first feature in the C1s excitation spectrum of C_{60} , which is due to transitions into t_{1u} -derived states, decreases in intensity by 50% on going from C_{60} to K_3C_{60} , as would be expected for half-filling of the t_{1u} -derived band. For K_4C_{60} , its intensity is additionally reduced, consistent with further charge transfer to C_{60} . In K_6C_{60} , this feature is no longer visible, as the t_{1u} band is completely filled and is therefore seen to lie completely below the Fermi level in the PES spectrum. Thus, in the case of K_6C_{60} , the first peak represents instead transitions into states derived from the molecular t_{1g} level. The second peak in the C1s excitation spectrum now corresponds to transitions into states derived from the molecular h_g level. The shift to lower energy and the broadening apparent in the spectra of the fullerenes both show the relaxation of the electronic structure of C_{60} upon intercalation, as well as the charge transfer induced chemical shift of the core level.

In Fig. 27 the loss functions of the same A_xC_{60} compounds are shown [153,154] which probe transitions from the occupied to the unoccupied electronic states as well as collective excitations. Going from C_{60} to K_6C_{60} the changes induced by electron doping are clearly visible. For K_3C_{60} new spectral features appear in the former gap at 0.55 and 1.2 eV. These can be assigned to the charge carrier plasmon (0.55 eV) due to a collective excitation of the t_{1u} electrons and to a plasmon related to the now possible transition from the half-filled t_{1u} -derived to the empty t_{1g} -derived states. Further doping causes even more fine structure in this energy region and a small energy gap in the case of K_4C_{60} . Reaching

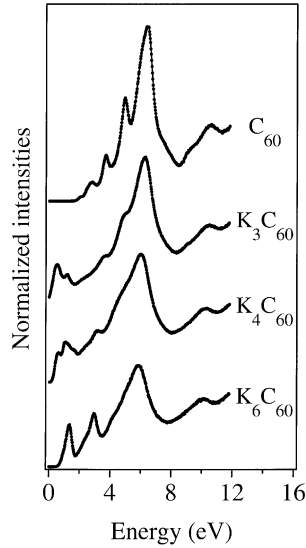


Fig. 27. Loss function, $\text{Im}(-1/\epsilon)$, of C_{60} , K_3C_{60} , K_4C_{60} and K_6C_{60} . The data are normalized to the valence band plasmon at about 25 eV and are offset in the y-direction.

K_6C_{60} a gap of about 0.5 eV has opened and the leading features with a shoulder at its low energy side is located at about 1.35 eV and results from a plasmon related to $t_{1u} \rightarrow t_{1g}$ transitions. We note that in the case of the intercalated C_{60} compounds, the contributions from the elastic line have been subtracted such that the results from optical studies [12,13,155] are reproduced at energies lower than ~ 0.3 eV. Upon intercalation, the π plasmon around 6 eV shows a small shift to lower energies (of the order of 0.3 eV) which is difficult to rationalize in detail, but which also illustrates the changes of the excitation properties of C_{60} with the addition of electrons to the fullerene cage and the changes of the crystal structure.

An understanding of the spectra for C_{60} and K_6C_{60} presented in Figs. 26 and 27 is relatively straightforward. Both materials have completely filled electronic levels which results in their observed insulating nature, i.e. they can be described as band insulators. However, the exact size of the energy gap is not only determined by the energy separation of the corresponding electronic states but also by the strong on-site correlation energy U (see discussions above) which, for instance, leads to a significant difference of the gaps measured in optical or combined PES–IPES measurements [30]. In the intermediate doping regime things become more complex. This is illustrated in Fig. 28, where the photoemission spectra of K_3C_{60} and K_4C_{60} near the Fermi level are shown. From Fig. 28, it is evident that K_3C_{60} has a finite DOS at the Fermi level, in full agreement with its metallic and (at low temperatures) superconducting ground state. In contrast, the spectrum of K_4C_{60} shows no emission from the Fermi level, a clear indication that this phase is insulating. In particular, the latter is unexpected as both phases have a partially filled conduction band and thus would be predicted to be metallic. In the following the spectroscopic results for A_3C_{60} and A_4C_{60} compounds are discussed in more detail and the impact of the correlation energy U , the electron–phonon and electron–plasmon coupling on the electronic structure of these phases is addressed.

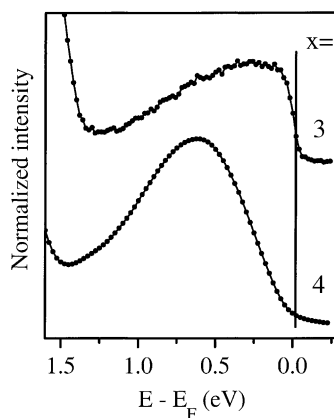


Fig. 28. Valence band photoemission spectra ($h\nu = 21.22$ eV) of K_3C_{60} ($x = 3$) and K_4C_{60} ($x = 4$) near the Fermi level (solid line) normalized to the C_{60} HOMO-derived spectral weight. While for K_3C_{60} a clear Fermi cutoff, i.e. a metallic ground state, is observed the spectrum of K_4C_{60} shows a vanishing DOS at E_F demonstrating its insulating nature.

5.2. A_3C_{60}

The metallic nature of thin A_3C_{60} films has also been reported from other PES studies [18,134,135,156,157] as well as from conductivity measurements [158,159]. On the other hand, it has been speculated that stoichiometric A_3C_{60} would have a gap of about 0.7 eV due to strong electron correlation and that the metallic and superconducting phases are thus off-stoichiometric [30]. A detailed analysis of the dependence of the superconducting transition temperature T_c upon the sample stoichiometry of $Na_2Cs_xC_{60}$ and $K_{3-x}Ba_xC_{60}$ compounds indicated, however, that stoichiometric A_3C_{60} most likely has a metallic ground state [160] as indicated by the photoemission results above. Independent of the exact stoichiometry, the photoemission profiles of A_3C_{60} materials already cannot be understood within a simple independent-electron picture. The bandwidth observed for the half-filled t_{1u} -derived conduction band is about 1.2 eV (see Fig. 28) and thus a factor of 5 larger than the predictions from band structure calculations. A clue to the explanation of this observation can be gained from low temperature PES studies of Rb_3C_{60} and K_3C_{60} [152] which are shown in Fig. 29. Similar data for K_3C_{60} have been reported by Benning et al. [156]. In these high resolution photoemission data, a fine structure becomes visible at low temperatures revealing a feature at the Fermi level followed by a second feature at about 250 meV BE and a third much broader one centered at about 600 meV. The structures close to E_F ($0 < BE < 300$ meV) are generally agreed to be phonon satellites, resulting from the excitation of molecular vibrations during the photoemission process [152] in analogy to the phonon sidebands observed in the PES of gas phase C_{60}^- [161]. Also shown in Fig. 29 are PES profiles of A_3C_{60} calculated within a model [152,162] which shows that good agreement can be found by taking into account relatively strong coupling of the electronic system to the molecular A_g and H_g vibrational modes. The electron–phonon coupling constants are derived from ab initio calculations [162] and they correspond to an electron–phonon coupling parameter, λ , of 0.58 and 0.68 for K_3C_{60} and Rb_3C_{60} , respectively, which are of the correct order of magnitude to explain the superconductivity in these compounds within a conventional electron–phonon scenario [15]. In addition, a relatively strong coupling of the conduction band electrons to the charge carrier plasmon observed at about 0.5 eV in the

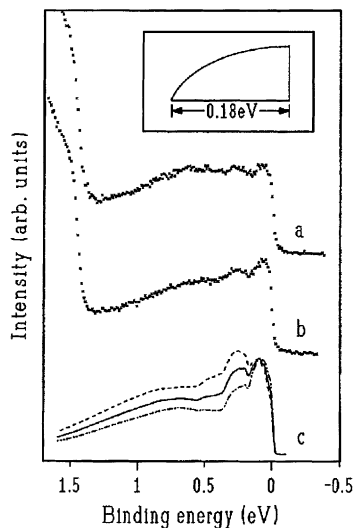


Fig. 29. Photoemission data for: (a) K_3C_{60} ; (b) Rb_3C_{60} at 10 K. Also shown are (c) the calculated spectra taking electron–phonon coupling and electron–plasmon coupling into consideration. The three lines illustrate the changes as a function of the electron–phonon coupling strength: $\lambda/N(0) = 0.068$ (dotted-dashed line), $\lambda/N(0) = 0.095$ (solid line), $\lambda/N(0) = 0.112$ (dashed line) [152]. The inset shows the form of the half-filled conduction band used in the calculation.

loss function has to be considered to model the high-energy feature around 600 meV in the photoemission spectra [152]. This electron–plasmon coupling is in line with the energy width of the plasmon as observed in the loss function which indicates a short lifetime of the plasmon which cannot be understood on the basis of electron–phonon coupling alone (see discussion below).

Alternative interpretations of the PES intensity at higher energies have been proposed. Firstly, the PES results have been discussed in terms of a shift of spectral weight due to the effects of correlation [163], in which it is suggested that A_3C_{60} could lie in the region of U/W in which a correlation satellite remains in the electron removal spectrum, despite the clear metallic nature of the carriers close to the Fermi level. Recent calculations, however, have shown that the effect of electron correlation cannot fully explain the magnitude of the satellite at 600 meV [164]. Secondly, it has been proposed that intra-molecular charge disproportionation occurs in A_3C_{60} compounds which arises from the simultaneous presence of strong correlations and the Jahn–Teller instability of the C_{60}^{3-} molecules [165]. The resulting electronic DOS is predicted to have a satellite about 600 meV below the Fermi level. Thus, the satellite observed in the photoemission spectra most probably arises from a combination of electronic correlations, electron–phonon and electron–plasmon coupling. This demonstrates the exceptional status of the fulleride materials as several mechanisms have a significant impact on the electronic properties.

The temperature dependence of the PES profiles of K_3C_{60} and Rb_3C_{60} has also been studied [152,166] and is shown in Fig. 30 for the case of K_3C_{60} . On going from 10 to 425 K a smearing out of the fine structure and a reduction of the intensity at the Fermi level is observed. Calculations taking into consideration the temperature dependence of the Fermi–Dirac distribution and changes in the population of the molecular vibrations could not model this behavior [20]. The gradual change that is observed in Fig. 30 over the entire temperature range argues against phase transitions as a cause. A recent theoretical study of the mean free path for electron conduction in metallic fullerenes has provided

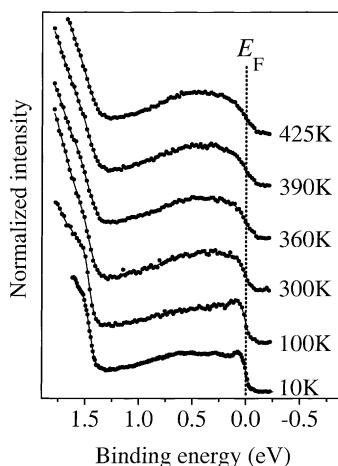


Fig. 30. Photoemission data for K_3C_{60} as a function of temperature [166]. The position of the Fermi level is marked as a dotted line. The spectra are offset in y -direction.

evidence that for higher temperatures the concept of quasi-particles breaks down as the lifetime of the ‘quasi-particles’ becomes larger than the one-particle bandwidth [167]. However, it is not clear whether this can explain the behavior seen in Fig. 30 and it remains an open question which mechanism is responsible for the temperature-dependent changes of the A_3C_{60} photoemission spectral weight underlining the complex nature of fulleride compounds. Finally, ultra-high resolution photoemission studies at very low temperatures (6 K) have revealed the superconducting energy gap and a BCS-type DOS below T_c consistent with the weak-coupling limit [168]. This shows that the fullerenes are ‘conventional superconductors’ where the superconductivity is due to electron–phonon coupling.

Further insight into the electronic structure of A_3C_{60} compounds can be gained from measurements of the loss function [118]. In Fig. 31 the loss function, $\text{Im}(-1/\epsilon)$, as well as the real part, ϵ_1 , and the imaginary part, ϵ_2 , of the dielectric function which have been obtained performing a KKA for a momentum transfer of 0.1 \AA^{-1} . At such a small momentum transfer the data presented in Fig. 31 are equivalent to those derived from optical studies. The insets of Fig. 31 focus on a narrower energy range of 0–1.7 eV. The loss function is dominated by a strong maximum at about 25 eV which is due to the $\pi + \sigma$ plasmon, a collective excitation of all valence electrons in the system. Above $\sim 8 \text{ eV}$ the additional features in the loss function are caused by C_{60} -derived $\sigma-\sigma^*$, $\pi-\sigma^*$ and $\sigma-\pi^*$ electronic transitions and by transitions from K3p shallow core levels. Below 8 eV several structures can be observed at about 0.55, 1.2, 2.3, 3.7, 5.0 and 6.3 eV which are a result of $\pi-\pi^*$ excitations. Compared to the loss function of pure C_{60} (see above) an overall broadening is observed in Fig. 31 and the respective maxima are shifted downward in energy. This shows that relaxation of the electronic states occurs as a response to the addition of three electrons to the C_{60} molecules. The feature appearing at 1.2 eV in K_3C_{60} is due to transitions of electrons from the now half-filled LUMO derived states into the next higher lying unoccupied states (LUMO + 1). An additional small shoulder can be observed at about 1.4 eV. Since the electronic states are very localized on the fullerene molecules this fine structure might result from electron–hole multiplet splitting in the excited state [169]. An alternative mechanism that can cause a splitting of features in the loss function is a Jahn–Teller distortion of the molecules. Various

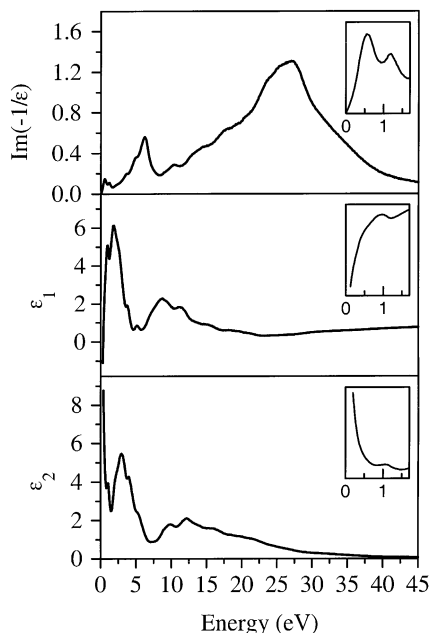


Fig. 31. Loss function, $\text{Im}(-1/\epsilon)$, as well as the real part, ϵ_1 , and the imaginary part, ϵ_2 , of the dielectric function of K_3C_{60} [118]. The momentum transfer is 0.1 \AA^{-1} . The inset shows a narrower energy range of 0–1.7 eV.

calculations [33–35] predict such a distortion of the order of 0.2 eV in agreement with the splitting observed in Fig. 31.

All interband excitations can be observed as maxima in the imaginary part of the dielectric function, ϵ_2 . As is evident from Fig. 31, ϵ_2 is large and positive at low energies while the real part, ϵ_1 , is also large but negative, which is expected for a metallic system. The zero-crossing of ϵ_1 generally defines the energy of the longitudinal collective excitation of the conduction electrons, the charge carrier plasmon. This zero-crossing is located at about 0.4 eV but there is also a small structure visible at about 0.6 eV in ϵ_1 and ϵ_2 which indicates the existence of additional ‘interband-like’ excitations in this energy region. This is further addressed in Fig. 32, where the optical conductivity σ at low energies is shown. The optical conductivity is best suited to separate contributions from different excitations to the dielectric response. The result of a Drude–Lorentz fit to the optical conductivity is also shown in Fig. 32 [118]. It demonstrates that the low energy part of the electronic excitations (below 1 eV) is a combination of Drude-like, intraband excitations and mid-infrared transitions centered around 0.6 eV. The presence of the latter suggest very strong interaction effects, e.g. electron–phonon coupling or electronic correlations in K_3C_{60} [170]. Calculations of the optical conductivity of K_3C_{60} [170] have shown that the inclusion of electron–phonon coupling reduces the width of the Drude peak and transfers spectral weight to the mid-infrared region. This underlines the importance of electron–phonon coupling in fulleride systems, as has been already discussed above. However, the calculations cannot reproduce the experimental results quantitatively, i.e. additional mechanisms have to be taken into account in order to fully describe the optical conductivity. The most likely further contribution arises from Coulomb interaction effects in the electronic system [170] which indicates that both electron–electron and

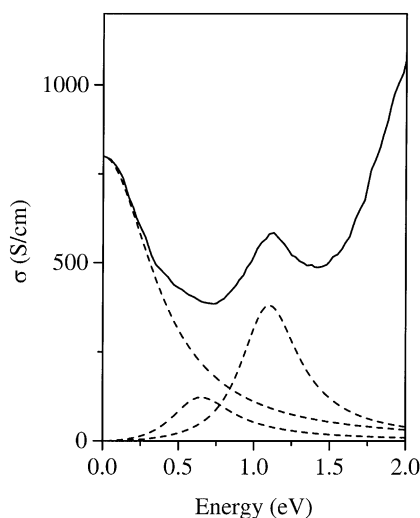


Fig. 32. Optical conductivity $\sigma = \omega\epsilon_0\epsilon_2$ of K_3C_{60} for a momentum transfer of 0.1 \AA^{-1} (solid line). Additionally shown is the result of a Drude–Lorentz fit revealing the free electron part and the first two interband contributions to the optical conductivity [118].

electron–phonon coupling must be considered to understand the electronic properties of fullerenes. A further example for this is discussed below for the case of A_4C_{60} materials.

Further insight into the electronic properties of K_3C_{60} can be gained by momentum dependent measurement of the loss function. As in pristine C_{60} (see above), the features in the loss function of K_3C_{60} , which are purely due to interband transitions (i.e. above 1 eV), show a strong momentum dependence because of their high molecular character [118]. The charge carrier plasmon at about 0.55 eV exhibits an unexpected and unusual behavior as shown in Fig. 33 [171–173] in that both its energy position and its spectral width do not change as a function of momentum transfer, q . This is quite different from what is observed for the charge carrier plasmons of many metallic systems. For a free electron gas within the random-phase approximation one would expect a plasmon dispersion proportional to the Fermi velocity and an increasing plasmon width due to a decreasing lifetime at higher momentum transfer [174]. As regards the plasmon dispersion in K_3C_{60} , the opposite behavior, i.e. a significantly negative dispersion, has been predicted from calculations as a result of the strongly inhomogeneous charge distribution in this material [175]. Neither of these expectations is consistent with the experimental result shown in Fig. 33. The origin of the non-dispersive nature of the charge carrier plasmon in K_3C_{60} lies in a complex interplay between local field effects due to the inhomogeneous charge distribution and the considerably momentum dependent dielectric background [171,172]. The latter is strongly reduced at higher momentum transfers as a consequence of the decreasing polarizability of the C_{60}^{3-} molecules which would lead to a relatively large positive contribution to the plasmon dispersion. These two effects: local field effects and the momentum dependent dielectric background, turn out to cancel resulting in the observed negligible plasmon dispersion [171,172].

The relatively large and momentum independent width of the charge carrier plasmon of K_3C_{60} is another example of the complex interplay of different coupling mechanisms in these materials as already discussed above. It could be shown that the plasmon width is caused by a decay of the plasmon

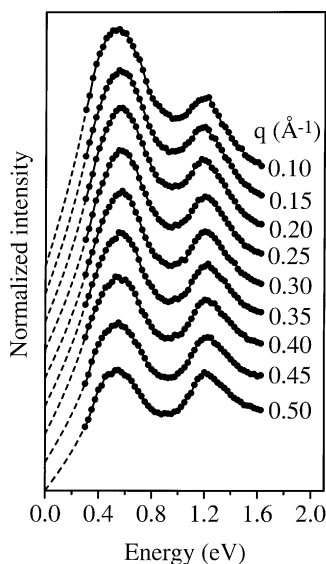


Fig. 33. Momentum dependent loss function of K_3C_{60} in the energy range of the charge carrier plasmon (0.55 eV) and the interband plasmon related to the first interband transition due to $t_{1u} \rightarrow t_{1g}$ excitations (1.2 eV).

into phonon-dressed electron–hole pairs [173] which is a direct consequence of the large electron–plasmon coupling in K_3C_{60} , whereby electron–phonon coupling increases the electron bandwidth such that this decay becomes energetically possible [173].

5.3. A_4C_{60}

A further demonstration of the unexpected electronic properties of fulleride compounds are the A_4C_{60} materials. These have an insulating, non-magnetic ground state [158,176] although their t_{1u} -derived bands are only partly ($\frac{2}{3}$) filled, which would lead one to expect a metallic behavior within a one-electron description. Full band structure calculations support the expectation of a metallic ground state [177]. The scenarios proposed to explain the insulating behavior have included the suggestion of a Mott–Hubbard ground state for A_4C_{60} [30,163,178] and a description of these compounds as Jahn–Teller insulators [179,180]. A systematic study of the optical conductivities of A_4C_{60} and $Na_{10}C_{60}$ (which also has a partly ($\frac{1}{3}$) filled conduction band and a loss function very similar to that of the A_4C_{60} compounds) has provided strong evidence for a Mott–Hubbard ground state of these compounds [181]. In Fig. 34 the optical conductivity σ of A_4C_{60} and $Na_{10}C_{60}$ is shown in an energy range of 0–2.2 eV. When compared to the optical conductivity of A_6C_{60} materials [155] (see also Fig. 27) the curves shown in Fig. 34 are rich in structure. In the case of Cs_4C_{60} and Rb_4C_{60} , four features at about 0.6, 1.0, 1.3 and 1.6 eV are visible. Going to $Na_{10}C_{60}$, K_4C_{60} and Na_4C_{60} a broadening of the structures is observed and the first feature shifts to lower energies. The changes in energy position and oscillator strength of the four features have been determined by a fit [181] and the results of this fit are shown in Fig. 35 as a function of the volume of the primitive unit cell, V_p . The crystal structures of the compounds under investigation differ in both their lattice parameters and symmetry, i.e. the number of nearest neighbors. Both these quantities determine the volume of the primitive unit cell V_p . As can be

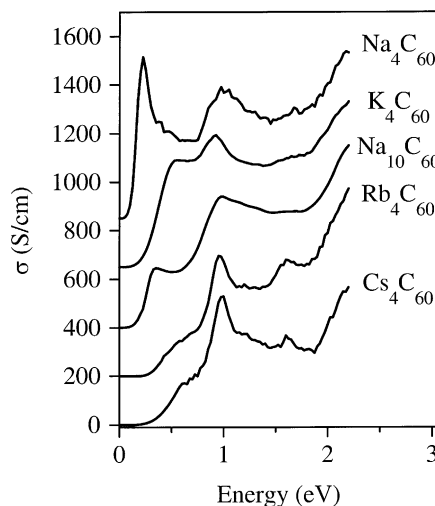


Fig. 34. The optical conductivity σ of A_4C_{60} and $Na_{10}C_{60}$ compounds as derived via a KKA of the measured loss function. The curves are offset in y-direction [181].

seen in Fig. 35, the energy position of the three higher lying transitions (open squares, circles and triangles) is almost independent of V_p and their oscillator strength also hardly varies. In contrast, the first transition (filled squares), which represents the energy gap, significantly shifts to higher energies with increasing V_p , while its oscillator strength considerably decreases. In a solid consisting of relatively weakly interacting molecules one has to distinguish between electronic excitations that are confined to a molecule and those which involve a transfer of the excited electron to a neighboring molecule. Whilst the latter strongly depend upon the interaction of the molecules, i.e. their distance and

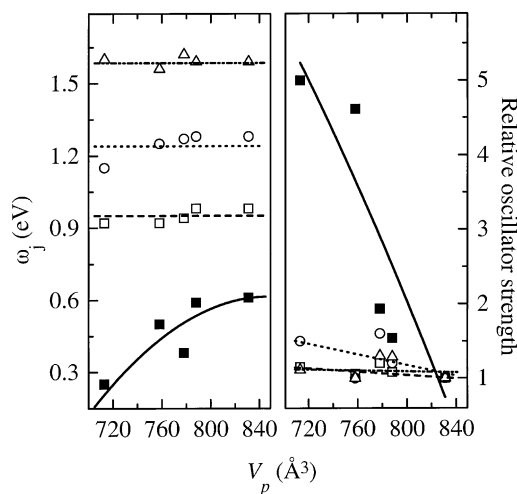


Fig. 35. The energy position ω_j and oscillator strength (relative to that of Cs_4C_{60}) of the four low-lying excitations shown in Fig. 34 plotted as a function of the volume of the primitive unit cell, V_p .

coordination, the first are only weakly influenced by these parameters. It can therefore be concluded from Fig. 35 that the optical gap in A_4C_{60} and $Na_{10}C_{60}$ is defined by an excitation to an adjacent C_{60} molecule. The higher lying excitations, however, are intra-molecular transitions between different electronic levels. Comparing the data in Fig. 34 to those of A_6C_{60} (Ref. [155] and Fig. 27), which exhibit only one structure centered at about 1.1 eV arising from $t_{1u} \rightarrow t_{1g}$ transitions, it is clear that the highly degenerate electronic levels of C_{60} must be split in A_4C_{60} and $Na_{10}C_{60}$. The most likely mechanism for such a splitting is a Jahn–Teller distortion of the molecules, which has been predicted to be of the order of 0.2 eV for the t_{1u} - and t_{1g} -derived levels of a C_{60}^{4-} molecule [33–35] consistent with the energy separation of the observed structures in Fig. 34. For $Na_{10}C_{60}$ a similar Jahn–Teller splitting can be assumed. This interpretation is supported by resonant Raman [182] and NMR [180] experiments in which an (optically forbidden) excitation has been observed at around 0.2 eV for A_4C_{60} compounds which can be attributed to transitions between the split t_{1u} -derived states. Furthermore, optical studies [155] have reported a splitting of the $T_{1u}(4)$ vibrational mode in A_4C_{60} and a significant broadening of the C1s excitation edges has been observed using EELS for A_4C_{60} [183] which is also fully consistent with a Jahn–Teller distortion of the fullerene molecules.

The insulating ground state of A_4C_{60} and the observed behavior of the energy gap, however, cannot be understood within a Jahn–Teller scenario. Firstly, the Jahn–Teller splitting of the molecular levels is considerably smaller than the calculated one-particle bandwidth [177], from which one would therefore expect the system to remain metallic. Secondly, the calculated bandwidths for f.c.c. and b.c.t. fulleride systems are very similar [177,184]. It is thus impossible to rationalize the observed difference in the magnitude of the gap between K_4C_{60} (b.c.t.) [66] and Na_4C_{60} (f.c.c.) [185] on the basis of a Jahn–Teller model because the gap then would depend solely on the Jahn–Teller splitting and the bandwidths, both of which hardly change. The energy shift of the gap as a function of V_p indicates transitions to adjacent molecules and one should therefore seriously consider electron correlation effects.

In the following it is shown that the size and the shift of the energy gap in the materials described above can be satisfactorily explained within a simple Mott–Hubbard description [181]. The gap Δ in a half-filled correlated fulleride system roughly behaves as [186]:

$$\Delta \sim (U_0 - \delta U) - \sqrt{N}W. \quad (11)$$

The parameters are the bare on-site correlation energy $U_0 \sim 2.9$ eV [15], the screening of this energy due to polarization $\delta U \sim 1.58$ eV for a b.c.t. lattice with lattice constants $a = 11.886$ Å and $c = 10.774$ Å and $\delta U \sim 1.69$ eV for an f.c.c. lattice with $a = 14.1$ Å [181], the orbital degeneracy N of the molecular t_{1u} levels which form the conduction band ($N = 3$), and the conduction bandwidth W . For systems with fourfold occupied t_{1u} states \sqrt{N} is reduced to $\sqrt{N_{\text{eff}}} = \frac{1}{2}(\sqrt{2} + \sqrt{3})$.

The lattice dependence of Δ enters via those parameters which are a function of the nearest neighbor distance d : $\delta U \propto d^{-4}$ (Ref. [30]) and $W \propto d^{-2}$ (Ref. [187]). Furthermore, band structure calculations give a width of the t_{1u} -derived bands of $W = 0.61$ eV for K_3C_{60} ($d = 9.927$ Å) [184], and 0.56 eV for K_4C_{60} ($d = 9.969$ Å) [177]. With the figures given above one obtains the gap as a function of d , $\Delta(d)$ ($d_0 = 9.969$ Å):

$$\Delta(d) \sim U_0 - \delta U \frac{d_0^4}{d^4} - \sqrt{N_{\text{eff}}}W \frac{d_0^2}{d^2}. \quad (12)$$

In Fig. 36, the d -dependence of Δ for crystals with b.c.t. A_4C_{60} , $A = K, Rb, Cs$ and f.c.c. symmetry (Na_4C_{60} , $Na_{10}C_{60}$) is shown. Additionally depicted are the gap values as derived from the optical

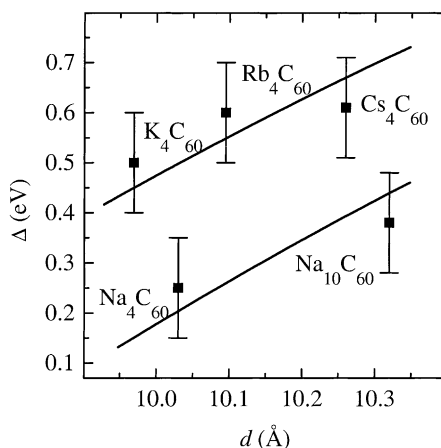


Fig. 36. The experimentally determined energy gap of A_4C_{60} and $\text{Na}_{10}\text{C}_{60}$ compounds as a function of the nearest neighbor distance d (symbols). The error bars give an estimate of the uncertainties arising from the normalization procedure in the KKA and the elastic line subtraction. The solid lines show the expected behavior for f.c.c. (lower line) and b.c.t. phases (upper line) within a simple Mott–Hubbard model (see text).

conductivities shown in Fig. 34. The agreement between the expectation derived from the simple model in Eqs. (11) and (12) and the measured gap values is remarkably good. This strongly indicates that alkali metal intercalated fullerene compounds with conduction bands that are partly filled with an even number of electrons have a correlated ground state, i.e. they are Mott–Hubbard insulators. This seems to be in contradiction to the observation that A_4C_{60} compounds are non-magnetic [176], whereas Mott–Hubbard insulators are usually magnetic having local magnetic moments, i.e. a local high-spin configuration. On the other hand, the results above also indicate a Jahn–Teller splitting of the C_{60} molecular electronic levels and such a splitting could stabilize a low-spin (non-magnetic) ground state if the Jahn–Teller splitting overcomes the Hund’s rule exchange energy as has been discussed in Section 2. Thus, both the Jahn–Teller effect and electronic correlations are important to understand the ground state of A_4C_{60} and $\text{Na}_{10}\text{C}_{60}$ and one is led to the conclusion that these materials deserve the name *non-magnetic molecular Jahn–Teller–Mott insulators*. It has also been proposed that the interplay of electronic correlations and the Jahn–Teller distortion causes intra-orbital charge disproportionation within the LUMO which results in an energy gap for A_4C_{60} compounds [188] that is mainly determined by the correlation energy U . This would also be in agreement with the experimental result discussed above.

The question now arises why the A_3C_{60} compounds are metallic although electronic correlations are strong and render the A_4C_{60} materials insulating. A relatively small but important difference between these two classes of compounds is the Jahn–Teller contribution to the correlation energy, U_{JT} [34,35,38,189]. While in A_4C_{60} it provides a positive contribution, thus stabilizing an insulating ground state, U_{JT} is negative for A_3C_{60} ($U_{\text{JT}} \sim -0.15$ eV) [34,35,38] which helps to reduce correlation effects (see Section 2). Considering the observed gap for f.c.c. Na_4C_{60} of ~ 0.25 eV and the reduction of U due to the Jahn–Teller contribution [34] one would expect the A_3C_{60} compounds to be metallic although still correlated. The fact that A_3C_{60} is strongly correlated and situated near a metal–insulator transition is nicely demonstrated in ammoniated K_3C_{60} which undergoes a phase transition to a correlated,

insulating ground state as a consequence of the larger lattice constant (=reduced bandwidth) as compared to pure K_3C_{60} [190]. Hence, a complete description of the electronic properties of alkali metal intercalated fullerenes requires the inclusion of electron correlation effects as well as electron–phonon coupling (both static and dynamic) and electron–plasmon coupling. These systems therefore provide model substances to study the interplay of various interactions.

5.4. K_xC_{70}

Alkali metal intercalation can also be carried out in higher fullerene solids. In Fig. 37 photoemission profiles for K_xC_{70} phases at 450 K are shown. This temperature has been chosen in order to examine the properties of all known K_xC_{70} phases, including K_3C_{70} which is stable only above 440 K (see the K_xC_{70} phase diagram above). The bottom curve represents the high temperature phase of pure C_{70} . Dilute doping stabilizes the aligned-but-rotating phase of C_{70} (see discussion of temperature-dependent photoemission profiles of C_{70} above) and shifts the valence band features by ~ 0.3 eV to higher binding energies as the Fermi level is now pinned at the conduction band minimum. The energy separation between the valence band, taken as the onset of emission, and the pinned Fermi level represents the band gap (transport gap) of C_{70} . This energy, 2.1 eV, is in excellent agreement with that deduced from combined photoemission and inverse photoemission experiments [150]. It corresponds to the energy needed to create an isolated electron and an isolated hole. The transport gap exceeds the optical gap, which is about 1.3 eV [191], because the optical excitations create electron–hole pairs that are bound on

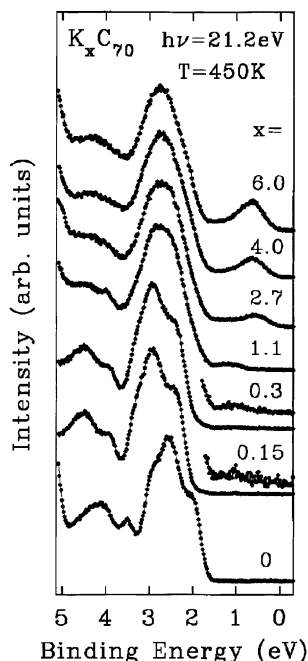


Fig. 37. Photoemission valence band spectra for K_xC_{70} at 450 K, a temperature that stabilizes $x = 1, 3, 4$ and 6 phases. The initial shift observed upon dilute doping corresponds to Fermi level pinning at the conduction band minimum as has been discussed for K_xC_{60} above. None of the spectra shows emission from the Fermi level, i.e. none of the K_xC_{70} phases is metallic.

a molecule as an exciton. This is a consequence of the electron correlation effects which, as discussed above, are also important in the case of higher fullerenes.

The spectrum in Fig. 37 for $x = 1.1$ represents the valence band of K_1C_{70} , although with a very small amount of K_3C_{70} . For it, the main feature centered at about 2.7 eV and the feature at about 4.5 eV are broader than in pristine C_{70} . Cooling to lower temperatures produces sharper structures but no other effects. Significantly, the onset of the leading feature of K_1C_{70} is 0.7 eV below the Fermi level. This feature, centered at about 1.3 eV, reflects states derived from the LUMO of C_{70} , a non-degenerate a_1'' orbital [192]. Its energy position is remarkable because, in an independent particle picture, a system with one valence electron in a primitive unit cell should have a half-filled band and thus states at the Fermi level.

Most likely, the width and location of the conduction band in K_1C_{70} results from a combination of two factors, band splitting due to a reduced crystal symmetry and electron correlation effects. The latter has been extensively discussed above for K_xC_{60} systems and the presence of a strong Coulomb interaction also in C_{70} has been established by experimental investigations (Ref. [31] and discussion above). A symmetry lowering in K_1C_{70} is not surprising given the ellipsoidal shape of the C_{70} molecule and the doubling of the unit cell observed for pristine C_{70} at low temperatures [42,43].

The spectrum in Fig. 37 for $x = 2.7$ represents the valence band of K_3C_{70} . An additional feature due to occupation of the LUMO + 1 band of C_{70} appears at about 0.5 eV. Despite the odd number of electrons transferred to the C_{70} molecules in K_3C_{70} , no emission from the Fermi level is observed. The spectral features near the Fermi level are very broad in comparison to K_3C_{60} (Fig. 29), which is also attributed to the reduced symmetry of the crystal lattice.

The valence spectrum of K_4C_{70} exhibits a single K-induced band that is centered at 0.7 eV below the Fermi level. Again, there is no emission from the Fermi level, i.e. insulating behavior, although the LUMO + 1 level of C_{70} is doubly degenerate [192], i.e. only half-filled in K_4C_{70} . This is analogous to what is observed for the A_4C_{60} compounds and it also most probably is a consequence of the strong electron correlations in fulleride materials. Continued intercalation to $x = 6$ increases the intensity of the feature near the Fermi level without introducing further changes. The insulating behavior of K_6C_{70} as observed in Fig. 37 is expected as it has completely filled electronic states.

In conclusion, none of the K_xC_{70} phases shows metallic behavior in contrast to their C_{60} relatives. This suggests that, as soon as further mechanisms such as disorder or symmetry lowering which hinder charge carrier mobility come into play, the intercalated fullerenes are insulating independent of the intercalation level. The main underlying cause, however, are electron correlation effects present in all fullerenes. Thus, the A_3C_{30} compounds might remain the only superconducting representative of the alkali intercalated fullerene family, where the fullerene molecules are not polymerized.

5.5. Intercalation beyond $x = 6$: Na_xC_{60}

One parameter that governs the phase diagram of intercalated fullerenes is the ionic radius of the intercalant. For instance, sodium ions are small enough to allow multiple occupancy of the octahedral site of the f.c.c. C_{60} lattice. Indeed, X-ray studies have shown that Na intercalation can be accomplished up to an intercalation level of $x \sim 10$ [193]. The crystal structure of $Na_{10}C_{60}$ with eight Na atoms occupying the octahedral site is shown in Fig. 38. Consequently, this offers one way to fill electrons not only into the t_{1u} -derived C_{60} states (LUMO) but also into the next higher lying t_{1g} -states (LUMO + 1). However, Na fullerenes do not behave as one would naively expect. This is demonstrated in Fig. 39,

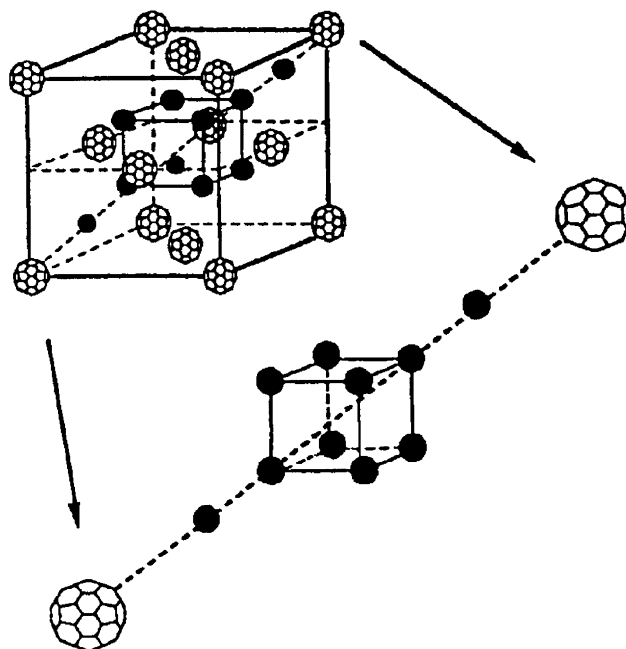


Fig. 38. Schematic crystal structure of $\text{Na}_{10}\text{C}_{60}$ (from Ref. [193]). The octahedral site of the f.c.c. fullerene lattice is large enough to harbor more than one sodium atom.

where the $\text{C}1\text{s}$ excitation spectra of Na_xC_{60} compounds are shown [194,195]. The curves are normalized to the σ^* -derived onset at about 290 eV. The intercalation level of the compounds shown has been determined via the lattice constant change as a function of x and the intensity of the $\text{Na}2\text{p}$ excitation edges [195]. As discussed above, $\text{C}1\text{s}$ excitation measurements can be used to determine the charge transfer to the C_{60} molecules. In the inset of Fig. 39 the charge on the C_{60} molecules as determined from the integrated area of the t_{1u} - and t_{1g} -derived features can be seen as a function of the intercalation level x . Whilst for intercalation less than six a full charge transfer from sodium to C_{60} is observed (in agreement with the alkali intercalated compounds discussed above) the $\text{C}1\text{s}$ excitation spectra do not change on going from Na_6C_{60} to Na_8C_{60} indicating that, despite the increasing Na intercalation level, there is no change of the charge on the fullerene molecules. This is corroborated by measurements of the loss function which also remains unchanged in this intercalation range [195]. At intercalation higher than eight, the charge on C_{60} once again starts to increase linearly with the intercalation level. Incomplete charge transfer has also been observed for alkaline-earth intercalated C_{60} (see below) but the behavior observed for $\text{Na}-\text{C}_{60}$ is quite unique among the alkali metal fullerenes. It becomes even more intriguing when one takes into account the fact that the $\text{Na}2\text{p}$ excitation edges [194,195] show that the sodium in Na_8C_{60} or $\text{Na}_{10}\text{C}_{60}$ is fully ionized, i.e. the oxidation of the sodium is complete but not all of the charge arrives at the C_{60} molecules.

The fact that the octahedral site of the f.c.c. C_{60} lattice is multiply occupied harbors the explanation for this effect. The sodium ions form a fully ionized aggregate around the octahedral site which gives rise to an ‘O void’ (octahedral void) with an attractive potential for electrons [194,196]. This is schematically shown in Fig. 40. Ab initio calculations [194,196] have shown that this O void can

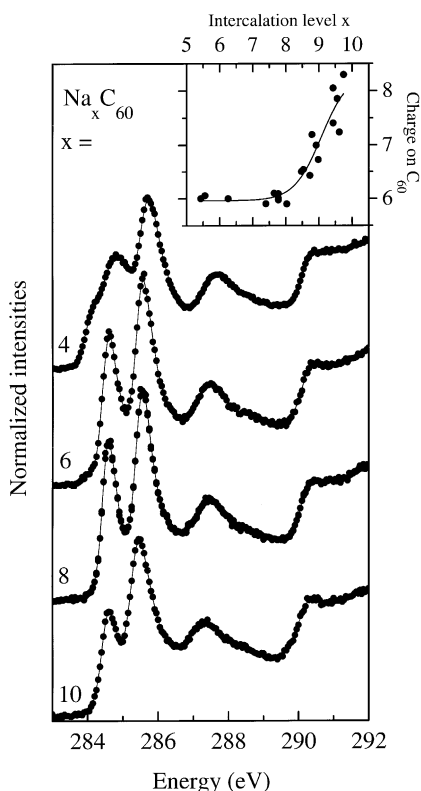


Fig. 39. C1s excitation spectra of Na_xC₆₀ compounds measured using EELS. The inset shows the charge on the C₆₀ molecules as derived from the intensity of the t_{1u}-(LUMO) and t_{1g}-(LUMO + 1) derived features.

accommodate two electrons and its BE is lower than the t_{1g}-derived (LUMO + 1) C₆₀ states. It thus becomes filled going from Na₆C₆₀ to Na₈C₆₀ resulting in the unusual behavior described above. Therefore, although for Na higher intercalation levels are accessible compared to K, Rb and Cs, volume confinement and geometrical constraints prevent intercalation from being an efficient charge transfer method in order to reach very high electron doping.

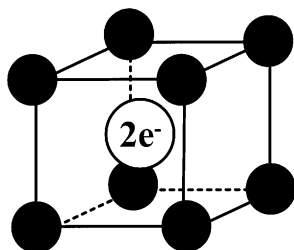


Fig. 40. Schematic representation of the 'O void' state (inner sphere) inside the aggregate formed by the positively charged sodium ions (black spheres) [194]. The BE of the two electrons that can occupy the 'O void' is lower than that of the (LUMO + 1) levels of C₆₀.

5.6. Charge transfer to single molecule: C_{70} on potassium

A further possibility to achieve high doping of fullerene molecules is to deposit the molecules onto alkali metal surfaces. For solid $K-C_{60}$ and $K-C_{70}$, for instance, saturation occurs at an intercalation level of $x = 6$. This saturation need not to be intrinsic as far as the charge transfer to the molecule is concerned. It rather reflects the maximum filling of the interstitial lattice sites. Higher coordination with metal ions is indeed achieved by depositing the fullerene molecules onto an alkali metal surface at low temperatures under UHV conditions. This has been successfully carried out for C_{60} where a charge transfer up to 12 electrons to the molecules was reached [197]. Similar results have also been obtained for C_{70} . In Fig. 41 the photoemission profile of single C_{70} molecules deposited onto potassium at 40 K is shown in comparison to that of K_6C_{70} . The spectra are normalized to the intensity of the feature located near 2.8 eV. The photoemission intensity between 0 and about 1.9 eV is considerably higher for C_{70} deposition onto K, and there is a significant change in line shape with an additional feature appearing at ~ 0.3 eV BE. These results indicate a filling of additional unoccupied states of C_{70} . Moreover, the feature at about 2.8 eV is narrower for C_{70} molecules on potassium and it is shifted slightly to higher BE. The differences between the spectra in Fig. 41 indicate that further electron transfer to C_{70} causes a rearrangement of the electronic states. Adding more C_{70} ultimately results in a photoemission spectrum equivalent to that of K_6C_{70} as the coordination number is progressively diluted in this metastable structure.

One can roughly estimate the $K-C_{70}$ coordination number by assuming equal cross-sections for photoemission from the electronic states of C_{70} that are filled with the electrons stemming from potassium. Comparison of intensities within 1.9 eV of the Fermi level yields an effective charge transfer of about 12 electrons to the C_{70} molecules on K metal. This represents the charge state arising from K saturation of the C_{70} molecules. The $K-C_{70}$ atomic and molecular arrangements are then very different from those of an ordered fulleride crystal or an adsorbate on a rigid surface. The fact that C_{70} does not accommodate more charge than the smaller C_{60} after deposition onto potassium might arise from a

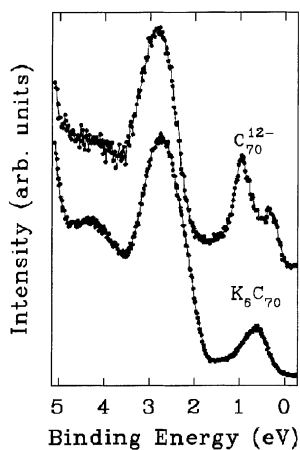


Fig. 41. Comparison of the photoemission spectrum of K_6C_{70} and C_{70} deposited on a potassium metal surface at 40 K. The higher intensity of the low BE feature and the shift to higher BEs for the upper curve shows that more than six electrons have been transferred to the C_{70} molecules. The enhanced charge transfer is a consequence of the fact that the K ions “solvate” the C_{70} molecules [69].

large enough gap in the unoccupied electronic structure of C_{70} which prevents the next states from filling due to energy reasons.

5.7. Alkaline-earth intercalation

Alkaline-earth intercalation was first reported for thin C_{60} films by Chen et al. [198]. They exposed the films in vacuo to Mg, Sr, and Ba, respectively, and performed PES measurements to determine the electronic structure. While for Mg intercalation only small interaction was observed, metallic character was seen for Sr and Ba. The reports of superconductivity in alkaline-earth intercalated C_{60} compounds [53–57] initiated further studies.

The electronic structure of Ca_xC_{60} compounds has been investigated using PES and IPES as well as band structure calculations [199–201]. It was shown that Ca_3C_{60} is insulating in agreement with activated transport behavior for this stoichiometry [202]. Ca_5C_{60} has been found to be metallic consistent with the transition into a superconducting phase. Furthermore, the calculations indicate a strong hybridization between Ca and C_{60} states for this stoichiometry [199,203]. In Fig. 42, C1s excitation measurements of Ca_xC_{60} compounds as a probe of the unoccupied electronic structure are shown [204]. The reduction in intensity of the first, LUMO-derived, feature with increasing Ca content clearly signals the charge transfer from Ca on successive intercalation. The C1s excitation spectrum of $Ca_{3.3}C_{60}$ closely resembles that of K_6C_{60} , in which six electrons have been transferred to the fullerene t_{1u} -derived band consistent with a complete transfer of the Ca4s electrons to the fullerene molecule. For $Ca_{5.6}C_{60}$ the t_{1u} -derived feature is absent as expected, but the intensity of the next t_{1g} -related feature is also significantly reduced. On further intercalation to $x \sim 7$, the t_{1g} spectral weight is still smaller, and

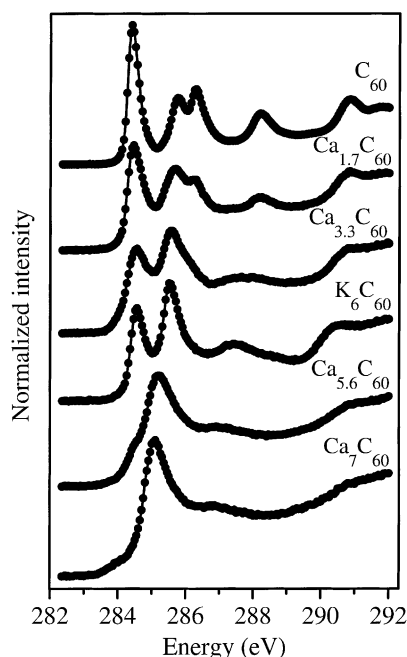


Fig. 42. C1s excitation spectra of Ca_xC_{60} and K_6C_{60} (from Ref. [204]). The curves are offset in y-direction.

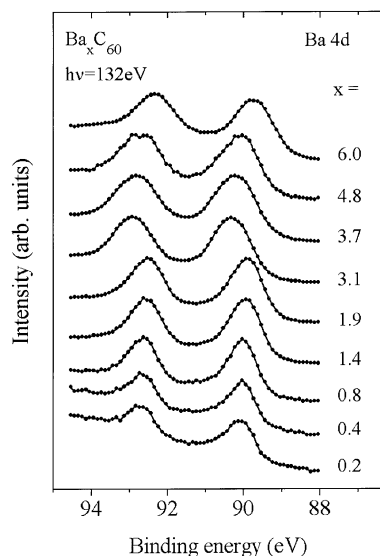


Fig. 43. Ba4d core level photoemission spectra for Ba_xC_{60} measured with a photon energy of 132 eV and an energy resolution of 300 meV.

one can roughly estimate a C_{60} charge state in Ca_7C_{60} of $\sim 11^-$, clearly showing the reduced degree of charge transfer from the Ca at higher intercalation levels due to hybridization confirming the predictions of the band structure calculations mentioned above.

The electronic structure of Ba_xC_{60} has been studied using photoemission and resonant photoemission spectroscopy [205]. Fig. 43 shows Ba4d core level spectra acquired at room temperature with an energy resolution of 300 meV. The two features at 92.7 and 90.1 eV BE reflect the $\text{Ba}4d_{3/2,5/2}$ spin–orbit doublet. This doublet grows in intensity with increasing barium intercalation. The peak binding energies and widths do not change for stoichiometries below $x = 1$. Thus, the core level results indicate the occupation of a single type of interstitial site below $x = 1$. This indicates the formation of a Ba_1C_{60} phase with the barium ions most likely occupying the octahedral sites of the f.c.c. fullerene lattice. This is consistent with transport measurements that found a minimum in activation energy around $x = 1$ [206].

This proposed Ba_1C_{60} phase has not been confirmed by structural studies yet. It would have a site occupation analogous to Rb_1C_{60} or Cs_1C_{60} . It is intriguing that Ba_1C_{60} seems to be stable at room temperature while K_1C_{60} is not, despite the fact that the Ba^{2+} ion is nearly the same size as the K^+ (1.34 vs. 1.33 Å). It is likely that the higher ionization state of Ba^{2+} leads to stronger attractive interactions between the Ba and C_{60} ions, thus stabilizing the Ba_1C_{60} compound.

Intercalation beyond $x = 1$ produces a broadening and a shift in the Ba4d doublet as can be seen from Fig. 43. This continues until $x = 3$, when the binding energies abruptly shift higher by about 0.35 eV. The broadening for $1 < x < 3$ reflects the superposition of more than one phase in the sample. The line-shape changes are too subtle to encourage spectral decomposition for further analysis. The abrupt shift evident for the spectrum at $x = 3.1$ reflects the complete filling of the t_{1u} -derived bands and the movement of the Fermi level across the gap to the lower part of the t_{1g} -derived bands.

Fig. 43 shows that intercalation past three results in a steady shift of the Ba4d doublet toward lower BE. At the same time, the spectra broaden slightly and the line shape becomes more asymmetric. The

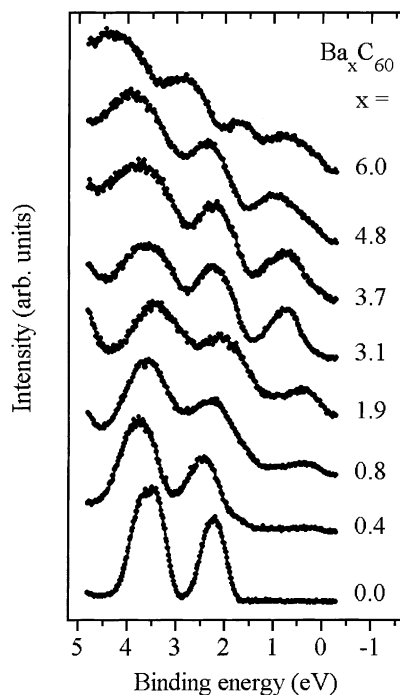


Fig. 44. Valence band photoemission spectra for Ba_xC_{60} measured at room temperature with a photon energy of 65 eV and an energy resolution of 90 meV. They are normalized to the area of the feature derived from the HOMO of C_{60} .

asymmetry can be understood in terms of the evolution from an insulating to a metallic state where the core hole, created by the photoemission process, is screened differently. The rather large shift is also related to the formation of a metallic phase beyond $x = 3$ which occurs together with a hybridization between Ba and C_{60} derived electronic states as will be discussed below.

Fig. 44 shows valence band photoemission spectra that demonstrate the effects of doping into the t_{1u} - and t_{1g} -derived levels of C_{60} . The energy resolution was 90 meV and the spectra were taken at room temperature. The bottommost curve of Fig. 44 shows features at 2.2 and 3.5 eV that arise from the highest occupied molecular orbitals, HOMO and HOMO-1, of pristine C_{60} . Intercalation to about $x = 0.1$ induces a rigid shift as the Fermi level is now pinned at the edge of the lowest unoccupied states of t_{1u} symmetry. Further intercalation induces changes that again can be attributed to Ba_1C_{60} formation. The spectrum for $x = 0.8$ represents, within experimental accuracy, the valence band of Ba_1C_{60} . Inspection shows a leading band that is about 1 eV wide, has a maximum at 0.4 eV, and has emission at the Fermi level. While the presence of these states at the Fermi level is a necessary condition for metallic character, it is insufficient. Indeed, transport measurements [206] at this intercalation level indicate that the resistivity increases upon cooling. Such behavior can be rationalized in terms of the very low electron density and charge carrier localization of the conduction band electrons due to disorder.

Intercalation beyond $x = 1$ increases the emission from the t_{1u} -derived bands. There is also broadening of the main valence band features because they represent a superposition of different phases in the samples. Comparison of the curve for $x = 3$ to that of saturated K_6C_{60} shows almost identical line

shape and binding energies. This indicates full charge transfer from the Ba6s level to fill the t_{1u} band completely.

Intercalation between $x = 3.1$ and $x = 6$ results in a shift of the valence band features, the appearance of new structure, and emission from the Fermi level that all can be attributed to occupation of the t_{1g} -derived states. By the time x reaches 6 there are two features visible at 0.7 and 1.7 eV BE which can be related to t_{1g} - and t_{1u} -derived states, respectively. This time, the appearance of emission from the Fermi level for $x > 3$ is connected with a metallic ground state of the corresponding phases [57,206]. The spectra for x between 3 and 6 cannot be modelled with a superposition of weighted amounts of the two end structures. This indicates that there exists at least one additional phase in this intercalation range in agreement with the fact that the superconducting phase of the Ba–C₆₀ compounds is Ba₄C₆₀ [56,57].

The metallic character of Ba₆C₆₀ requires that there are changes in the electronic states that reflect more than just charge transfer. In particular, the t_{1g} level of C₆₀ is threefold degenerate and full charge transfer would produce an insulator for Ba₆C₆₀. Band structure calculations have indicated that in Ba₆C₆₀ the 6s levels of Ba move high enough in energy that hybridization between Ba and C₆₀ involves Ba4d states [207,208]. In order to investigate the Ba character of the states near the Fermi level, resonant photoemission studies at the Ba4d resonance have been performed. At this resonance, the photoemission cross-section for valence states can be strongly enhanced due to an interference between direct photoemission and an Auger decay of the core excitation [127]. Since the core hole is localized on an atom, resonance can only be observed for electrons with the same atomic character, and the specific partial DOS (PDOS) can be deduced by comparing photoemission measurements with photon energies off- and on-resonance.

Fig. 45 shows valence band spectra of Ba₆C₆₀ measured at 103 (on-resonance) and 98 eV (off-resonance) photon energy. Here, the Ba4d¹⁰ → 4d⁹4f¹ excitation leads to resonant behavior. The valence band behavior near the Fermi level shows a pronounced dependence on the photon energy. In

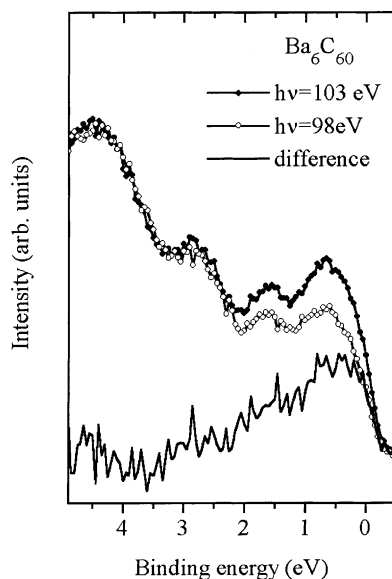


Fig. 45. Resonant photoemission spectra for Ba₆C₆₀ measured with photon energies that correspond to off-resonance (98 eV) and on-resonance (103 eV).

particular, the intensity between the Fermi level and 2.1 eV is about 25% larger for on-resonance measurements. Note that there is no change in the deeper lying states which shows that they have no Ba character. The fact that the features at 0.7 and 1.7 eV both show enhancement signifies that the t_{1u} and t_{1g} orbitals of C_{60} are hybridized with Ba states. The average admixture of Ba can be estimated to be about 25%, assuming that the states near the Fermi level exhibit the same resonant enhancement as the Ba5p shallow core levels [205]. The spectral shape of the Ba PDOS, obtained by subtraction of the off-resonance from the on-resonance spectrum, is also shown in Fig. 45. The hybridization of the t_{1g} level is about twice that of the t_{1u} level, consistent with the energy alignment of the respective levels. These results are in agreement with band structure calculations of Ba_6C_{60} and Ba_4C_{60} [207–209] where a hybridization between Ba4d and C_{60} orbitals was deduced. Resonant photoemission studies of Ba_1C_{60} and Ba_3C_{60} failed to reveal any enhancement of the photoemission intensity near the Fermi level. This again indicates that there is essentially complete charge transfer of the Ba6s electrons to C_{60} with no hybridization for Ba_xC_{60} compounds with $x < 3$. Later PES studies of the Ba– C_{60} series [200,201,210] reported results equivalent to what is discussed above.

6. Heterofullerenes

In this section, the experimental results on the electronic structure of pristine $C_{59}N$ in the solid, which were obtained using high-energy spectroscopies, are presented. $C_{59}N$ is one example of how to achieve a type of n-type doping by substituting C atoms with heteroatoms (N). It turns out that $C_{59}N$ forms dimers which condensate in a monoclinic crystal structure [80]. The molecular structure of $C_{59}N$ is illustrated in Fig. 46. The dimer formation has pronounced consequences on the electronic properties as will be shown in the following.

Fig. 47 shows a comparison of the valence band photoemission and the C1s excitation spectra (EELS) of $(C_{59}N)_2$ and C_{60} [211]. The data are normalized to the intensity of the σ -derived structure at

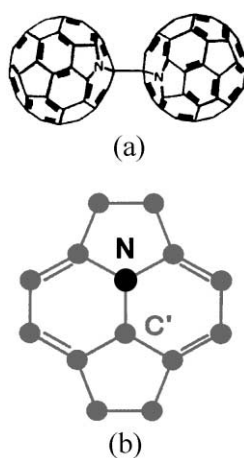


Fig. 46. Schematic representation of the molecular structure of $C_{59}N$ dimers. The two monomeric units are connected by a single carbon–carbon bond (a), whereby the two carbon atoms involved sit next to the nitrogen on each monomer (labeled C' (b)).

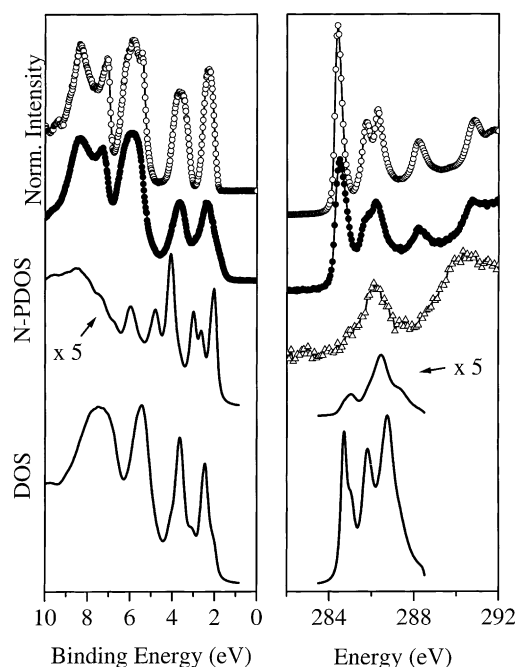


Fig. 47. Valence band photoemission spectra and C1s core level excitation spectra of $(C_{59}N)_2$ (●), and C_{60} (○). Also shown is the N1s excitation spectrum (Δ) of the heterofullerene. At the bottom in each panel are both the calculated DOS for the $C_{59}N$ dimer and the DOS projected onto the N atomic functions (N-PDOS).

5.5 eV BE and to the σ^* onset at 290.5 eV. In addition, the right-hand panel of Fig. 47 shows the N1s excitation spectrum of $(C_{59}N)_2$ downshifted in energy by 115.5 eV, which is the difference between the N1s and C1s core level binding energies ($400.7 - 285.2 = 115.5$ eV), measured using X-ray photoemission [212]. At the bottom in each panel, the calculated N-derived PDOS and the total DOS are plotted which have been obtained performing calculations based upon density functional theory (DFT) [81,211]. For the purpose of comparison, the discrete levels of the isolated dimer were broadened so as to simulate solid state effects as well as lifetime and spectrometer resolution broadening, and the DOS were shifted such that the energy of the leading maximum matches that observed in experiment. For $(C_{59}N)_2$, both the photoemission and C1s excitation spectra are broader than those of C_{60} , but the energy positions of the main features remain essentially unchanged. The broadening is most probably a result of the lower molecular symmetry, i.e. the lower degeneracy of the electronic levels. Additionally, the first photoemission maximum of $(C_{59}N)_2$ has a shoulder at about 0.5 eV lower BE, which, upon consideration of the occupied N-PDOS, can be assigned to states related to the extra electron which maintains a high degree of nitrogen character.

This conclusion is in perfect agreement with the C1s and N1s excitation spectra shown in Fig. 47. The overall shape of the C1s excitation spectrum of the heterofullerene is very similar to that of C_{60} , apart from an extra broadening of the spectral features of the former. In fact, within experimental error, the spectral weight of all π^* -derived structures below the σ^* edge at 292 eV is identical for both C_{60} and the heterofullerene. This indicates that the N-substitution does not lead to significant occupation of the C-derived low-lying unoccupied states of C_{60} . The lack of a strong feature in the N1s excitation

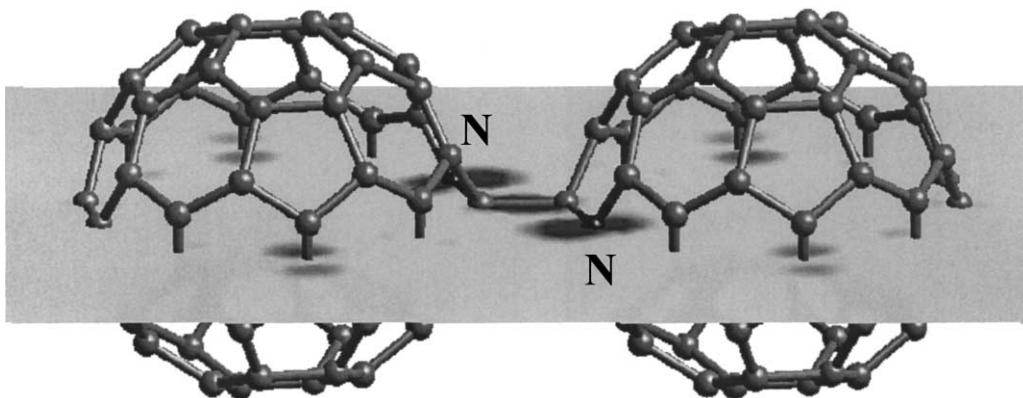


Fig. 48. A cut through the electronic density distribution of the HOMO of $(C_{59}N)_2$ depicted in the plane passing through the N atoms and the intermolecular bond.

spectrum at energies corresponding to the lowest unoccupied states in the C1s spectrum also lends weight to the arguments put forward above in favor of the localization of the “extra” electron. This is also fully consistent with the calculated unoccupied N-PDOS.

The results discussed above are a direct consequence of the electron density distribution of the HOMO and the LUMO of the $C_{59}N$ dimer. The HOMO of $(C_{59}N)_2$ is considerably different from that of C_{60} and also from that of a single $C_{59}N$ molecule [213] as is outlined in Fig. 48. Its electron density is strongly concentrated on the N atoms and the intermolecular bond [81,211]. In contrast, the LUMO of $(C_{59}N)_2$ only has a strong weight on the C atoms sitting at both ends of the dimer with a weak amplitude at the intermolecular bond.

The dielectric function of solid $(C_{59}N)_2$ has been determined by performing a KKA of the loss function measured using EELS [214,215]. This yields a static dielectric function at zero energy, $\epsilon(0)$, of ~ 5.6 which is larger than that of C_{60} ($\epsilon(0) = 4$) [13]. This higher static polarizability of the $(C_{59}N)_2$ solid has its origin in the smaller optical gap. In Fig. 49, the optical conductivity, $\sigma = \omega\epsilon_0\epsilon_2$, for small momentum transfer ($q = 0.1 \text{ \AA}^{-1}$) of $(C_{59}N)_2$ is shown in comparison to that of C_{60} [215]. Both curves

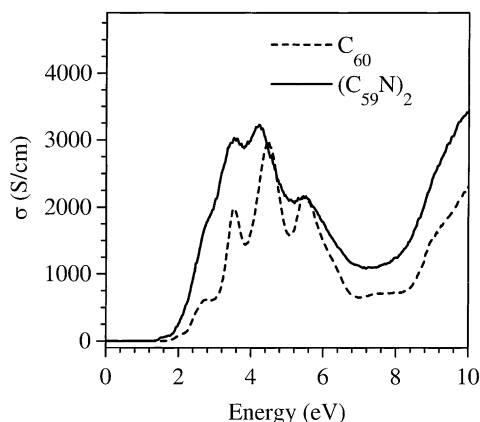


Fig. 49. Optical conductivity, σ , of solid $(C_{59}N)_2$ and C_{60} .

are similar in overall shape. Five structures are visible, respectively, which arise from dipole allowed transitions between the occupied and unoccupied electronic states. The features for $(C_{59}N)_2$ are broadened similar to what is observed for the results from photoemission and EELS excitation measurements (see above). The onset of the spectra gives a measure of the optical gap which is found to be 1.8 eV for C_{60} and 1.4 eV for $(C_{59}N)_2$. This difference is in nice agreement with the calculations of Kohn–Sham energy levels [81] which predict a decrease of the optical gap of about 0.4 eV going from C_{60} to $(C_{59}N)_2$.

Excitations between the occupied and the unoccupied electronic states can also occur in core level photoemission experiments. This is a direct consequence of the enhancement of the effective nuclear charge by one in the photoemission final state which is felt by all outer electrons. The sudden change of the effective nuclear charge can now result in interband transitions which ‘screen’ the core hole induced by photoemission. Such interband transitions then appear as so-called shake-up structures on the high BE side of the main core level. These shake-up structures supplement the information gained from optical or EELS studies, as they are not governed by selection rules.

Fig. 50 shows a comparison of the C1s core level shake-up structures of C_{60} and $(C_{59}N)_2$ to the corresponding loss function as obtained using EELS [212]. Apart from an overall broadening of both the C1s main line and shake-up structures as well as of the loss function for $(C_{59}N)_2$, which is caused by the distortion of the fullerene cage and the presence of the more electronegative N, the curves compared in Fig. 50 look very similar. The origin of the features in the $(C_{59}N)_2$ loss function and shake-up spectrum can therefore be addressed in the same way as for C_{60} [18,20]. The six features recognizable in the $(C_{59}N)_2$ loss function (labelled 1–6) are due to transitions between the π and π^* molecular orbital manifolds and have (except for peak 2 — labelled B in the shake-up spectrum) clearly corresponding

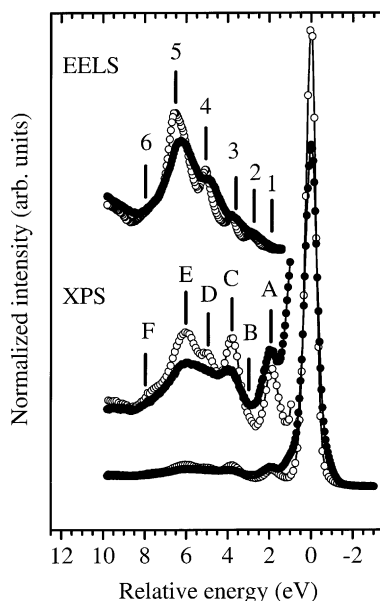


Fig. 50. C1s core level photoemission spectra of $(C_{59}N)_2$ (●) and C_{60} (○). The shake-up structures on the high BE sides of the C1s main lines of $(C_{59}N)_2$ and C_{60} are shown on a vertically expanded scale. The energy-zero of the photoemission spectra corresponds to the C1s BE. Uppermost: EELS loss functions of $(C_{59}N)_2$ (●) and C_{60} (○).

counterparts in the photoemission shake-up spectrum (labelled A, C, D, E and F). Apart from the relatively small weight of feature B in the shake-up spectra, the most striking difference between the loss functions and the shake-up spectra is the intensity of feature 1. The onset of the loss function has very low intensity, whereas peak A in the shake-up spectra is intense. This is a clear indication that this lowest transition has non-dipole character. In C_{60} , the lowest transition corresponds to the dipole-forbidden ‘gap’ transition between the h_u (HOMO) and the t_{1u} (LUMO). For $C_{59}N$, this corresponds to the lowest energy transition possible between molecular orbitals which have significant weight at the carbon sites of the heterofullerene. As discussed above, the HOMO of $(C_{59}N)_2$ lies at lower BE than that of C_{60} and has a high degree of N character. Nevertheless, the majority of the low-lying occupied states having C character correspond more to the HOMO of unsubstituted C_{60} . This is consistent with the fact that peak A occurs at the same energy in the shake-up spectra of both fullerenes.

The substitution of the N into the heterofullerene now gives us the possibility of measuring the excitations of the system in a site specific manner. By measuring the shake-up satellites of the N1s core level, we can selectively study the transitions between molecular orbitals with significant weight at the N site. Fig. 51 shows a comparison of the shake-up regions of the C1s and N1s core level photoemission spectra of $(C_{59}N)_2$. In each case, the energy zero corresponds to the BE of the main line (N1s: 400.7 eV; C1s: 285.2 eV) and the spectra are normalized to have the same total area. Comparison of the C1s and N1s shake-up spectra reveals a marked difference. In contrast to the C1s shake-up spectrum, the N1s shake-up spectrum has no peak at ~ 1.8 eV relative energy (peak A in Fig. 50). This is once more clear evidence in support of the calculated spatial distributions of the electronic states on either side of the chemical potential. Thus, as the LUMO states of the heterofullerene have practically zero weight at the N site, the sudden injection of a core hole at this site cannot be screened by a

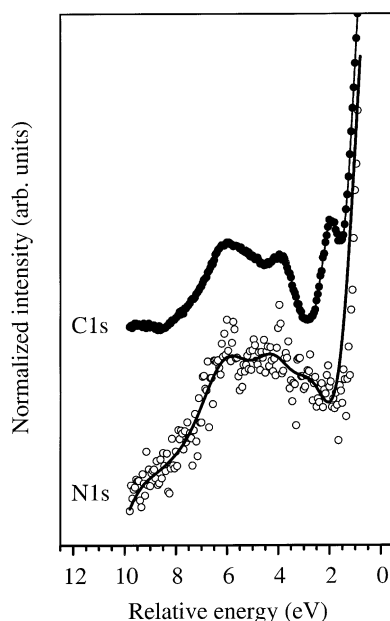


Fig. 51. C1s (●) and N1s (○) core level photoemission shake-up spectra of pristine $(C_{59}N)_2$. The shake-up spectra are offset vertically and are plotted on an energy scale relative to the respective 1s core level binding energies (see text for details).

transition between the high-lying occupied states and the lowest unoccupied molecular orbitals of the heterofullerene. Above ~ 3 eV relative energy, the C1s and N1s shake-up spectra look similar with peaks at ~ 4 and ~ 6 eV. These features involve transitions into π^* levels of higher energy than the LUMO, or represent excitation of the π plasmon, showing that the molecular orbitals involved have significant weight at the nitrogen site.

It is also instructive to compare the electronic structure of $(C_{59}N)_2$ with another fullerene compound that is comprised of C_{60}^- dimers, the RbC_{60} dimer phase. Formally, these two materials are isostructural and isoelectronic. Fig. 52 shows such a comparison for the photoemission spectra of $(C_{59}N)_2$ and RbC_{60} (data from Ref. [216]) up to a BE of 5 eV. For the purposes of comparison, the spectrum of dimerized RbC_{60} has been shifted by 0.25 eV to lower BE. Fig. 52 suggests that the perturbation of the electronic levels of C_{60} is more pronounced in the case of the RbC_{60} dimer — with the photoemission feature at lowest BE clearly consisting of two peaks separated by ~ 0.3 eV, and split-off from the rest of the spectrum by ~ 1 eV. Based on the behavior of other alkali metal fullerenes, one can reasonably expect the charge transfer from the Rb5s states to be complete and thus the photoemission spectrum of RbC_{60} can be compared with the broadened DOS of the isolated C_{60}^- dimer [211]. The energy distribution of the states observed in the photoemission spectra of the solids is well reproduced in the calculation, apart from a smaller separation of the highest energy feature from the main peak in the case of the C_{60}^- dimer. This type of discrepancy can be expected as a result of the difference between a free molecular anion and one confined in the fulleride. The calculations also show that the spatial distribution of the HOMO in the C_{60}^- dimer is also as in $(C_{59}N)_2$, with the largest amplitude on the intermolecular bond and the C atoms in the positions corresponding to the nitrogens in $(C_{59}N)_2$ [211]. The most important difference between the two dimers is due to the presence of the additional positive charge on the nitrogen cores in the heterofullerene. This causes a lowering of the

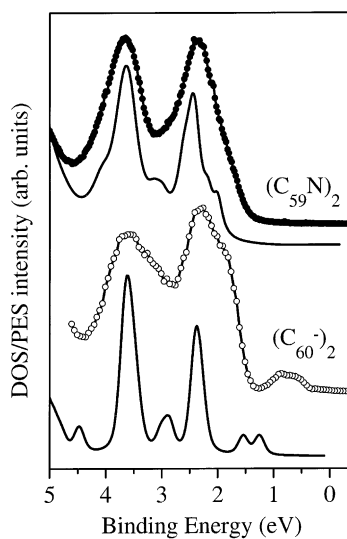


Fig. 52. Valence band photoemission spectra of solid $(C_{59}N)_2$ (●) and the RbC_{60} dimer phase (○) (the latter from Ref. [216]). The spectrum of RbC_{60} is shifted by 0.25 eV to lower BE. The solid lines depict the calculated DOS for a $C_{59}N$ and a C_{60} dimer, respectively.

energy of the HOMO and HOMO-1 states of the $C_{59}N$ dimer, and reduces the splitting of the occupied electronic levels in general.

7. Endohedrally doped fullerenes

7.1. $La@C_{82}$

The last of the three fullerene doping methods to be considered is endohedral doping. One of the key parameters which control the electronic properties of endohedrally doped fullerenes is the amount of charge that is transferred from the encaged atom to the fullerene molecule. Until recently, the charge distribution in monometallofullerenes filled with lanthanide ions has been discussed almost exclusively in terms of the inclusion of trivalent ions. The most prominent example is $La@C_{82}$. Fig. 53 provides an overview of the electronic structure of $La@C_{82}$ and C_{82} [87]. It compares the predominantly carbon derived electronic DOS near the Fermi level. The two curves are offset for clarity. The differences are emphasized by the bottom spectrum, which was obtained by subtracting the data points for C_{82} from those for $La@C_{82}$ after shifting the C_{82} spectrum by -0.18 eV to obtain the best overall agreement of the main valence band features. The difference spectrum makes it clear that the valence electronic structures differ throughout the leading 10 eV. This demonstrates that La incorporation introduces more profound changes than simple charge transfer to rigid electronic states of the fullerene cage.

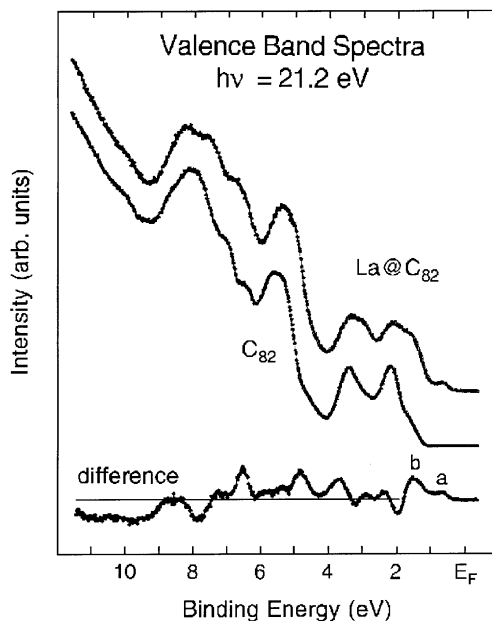


Fig. 53. Comparison of the valence band photoemission spectra of $La@C_{82}$ and C_{82} measured with a photon energy of 21.2 eV. At this photon energy mainly the C2p derived electronic DOS is probed. The difference curve at the bottom was obtained after shifting the C_{82} spectrum by -0.18 eV for the best overall agreement of the main features. Significantly, the difference curve shows spectral changes throughout the valence band. The feature with lowest BE for $La@C_{82}$ centered at 0.64 eV is attributed to the SOMO-derived level.

Nevertheless, the two low energy features in the difference spectrum within the first 2 eV of the Fermi level indicate ‘new’ occupied electronic states which result from a charge transfer from the La to the carbon cage. The observation of two features at low binding energies with an intensity ratio of about 2 suggests that the charge transfer in La@C_{82} is 3, resulting in a completely occupied HOMO-1 level and a singly occupied molecular orbital (SOMO) near the Fermi level. This interpretation is in good agreement with electron spin resonance studies which find an unpaired spin in La@C_{82} [217]. It is evident from Fig. 53 that there is no emission from the Fermi level, i.e. La@C_{82} is an insulator despite having a singly occupied molecular orbital. This might again be a consequence of the strong electronic correlations in fullerenes although, in a La@C_{82} solid, effects like disorder or unit cell doubling might also be present rendering the material non-conducting.

Further insight into the interaction between the La ions and the fullerene cage in La@C_{82} can be gained by core level photoemission. Fig. 54 shows the $\text{La}3d$ spectrum measured with a photon energy of 1486.6 eV [87]. As the $\text{La}3d$ electrons are quite sensitive to the distribution of valence electronic charge surrounding the La ion, the $\text{La}3d$ photoemission spectrum provides a clear indication of the electronic environment sensed by La inside the C_{82} cage. The $\text{La}3d$ spectrum in Fig. 54 shows two dominant structures, each with weaker shoulders at lower BE. A comparison of the $\text{La}3d$ signature for La@C_{82} to that of the trihalides of La [86] shows very similar line shapes, supporting the picture that the La ion within the fullerene cage is essentially trivalent. For the La trihalides the relative magnitude of the lower energy doublet decreases as the electronegativity of the halide decreases. By comparison, one finds that the carbon cage environment of La@C_{82} has an effective electronegativity less than that in LaBr_3 . This also indicates that La@C_{82} is not purely ionic but there is hybridization between the La ion and the fullerene cage. A finite hybridization of $\text{C}2p$ and $\text{La}5d$ levels has indeed been observed in a resonant photoemission study where the effective charge on the La ion has been determined to be $\text{La}^{2.7}$ [88]. It is emphasized that such a hybridization tends to localize charge inside the fullerene cage providing an additional mechanism that stabilizes an insulating ground state of La@C_{82} solids.

7.2. Tm@C_{82}

A further example of inclusion of a lanthanide ion in a fullerene cage is Tm@C_{82} . It represents the first example of a purely divalent lanthanide monometallofullerene. The divalent nature of Tm in

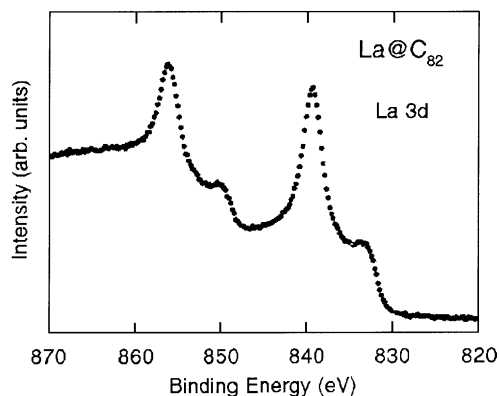


Fig. 54. $\text{La}3d$ core level photoemission profile of La@C_{82} obtained with a photon energy of 1486.6 eV.

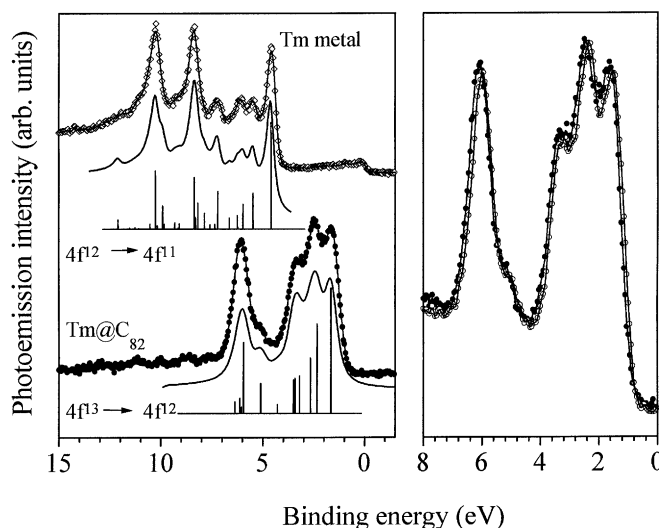


Fig. 55. Left-hand panel: 4f photoemission spectra of Tm metal (\diamond) and the $C_{3v}(8)$ isomer of $Tm@C_{82}$ (\bullet) (the C_{82} background has been subtracted as described in Ref. [218]). Below the spectra the calculated multiplet distribution for $4f^{12} \rightarrow 4f^{11}$ and $4f^{13} \rightarrow 4f^{12}$ photoemission after Ref. [219] are shown. Right-hand panel: comparison between the 4f multiplets of the $C_{3v}(8)$ isomer (\bullet) and the $C_s(6)$ isomer (\circ) of $Tm@C_{82}$.

$Tm@C_{82}$ is demonstrated in Fig. 55, where in the left-hand panel, the Tm4f X-ray photoemission (XPS) profile of the C_{3v} isomer of $Tm@C_{82}$ [218] is compared to that of Tm metal and calculations of the Tm4f multiplet spectra for a Tm^{2+} and a Tm^{3+} ion [219]. In the case of $Tm@C_{82}$ the spectral contributions of the C_{82} derived states have been subtracted [218]. As is evident from Fig. 55, the 4f multiplet spectra can be used as a fingerprint of the charge state of the Tm ion. There is an almost perfect agreement of the $Tm@C_{82}$ spectra with the calculations for a $4f^{13} \rightarrow 4f^{12}$ photoemission process, which proves a $4f^{13}$ ground state configuration and thus the divalent nature of Tm in $Tm@C_{82}$. Furthermore, the charge transfer is independent of the fullerene cage symmetry. The right-hand panel of Fig. 55 shows a comparison of the 4f spectra of $Tm@C_{82}$ isomers with $C_{3v}(8)$ and $C_s(6)$ symmetry which are, apart from a small energy shift, virtually identical [220].

This result has been corroborated by measurements of the Tm4d XPS profile and the Tm4d excitation spectra for the two $Tm@C_{82}$ isomers [218,220]. In Fig. 56, a comparison of the Tm4d excitation spectra of $Tm@C_{82}$ (C_{3v} isomer, Ref. [218]) and Tm metal (from Ref. [221]) is presented. From the selection rules within the Russell–Saunders coupling scheme, the allowed absorptions for the $4f^{12}$ and $4f^{13}$ initial state configurations give $4d^9 4f^{13}$ final states with 3H_6 , 3H_5 , and 3G_5 symmetry and a $4d^9 4f^{14}$ final state with $^2D_{5/2}$ symmetry, respectively [222]. These final states match the experimental spectra for Tm metal and the monometallofullerene nicely. Thus, the Tm4d excitation spectrum of the endohedral shown in Fig. 56 quite clearly indicates a $4f^{13}$ ground state, with no indication of trivalent Tm.

The C-derived part of the electronic structure of the two isomers of $Tm@C_{82}$ discussed above significantly differs, i.e. is dependent on the molecular structure and symmetry, as was also found for the C_{78} isomers discussed earlier. This is demonstrated in Fig. 57, where we show the C1s excitation edges of the two $Tm@C_{82}$ isomers [220]. The spectra are normalized to the σ^* edge at 290.5 eV. The lowest lying unoccupied states of the $C_{3v}(8)$ isomer appear to be more strongly clustered in energy,

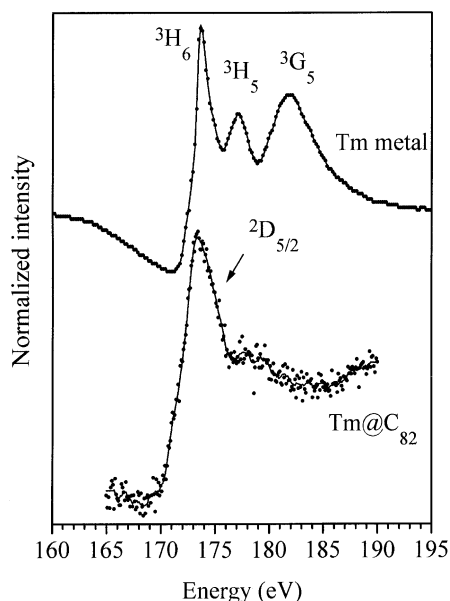


Fig. 56. Below: Tm4d excitation spectrum of the C_{3v} isomer of Tm@C₈₂ measured using EELS in transmission. Above: the corresponding spectrum of Tm metal from Ref. [221].

giving rise to the more pronounced LUMO-derived spectral weight at 284.2 eV in the C1s excitation spectrum. This is consistent with the higher symmetry of the $C_{3v}(8)$ isomer. For the $C_s(6)$ isomer, the LUMO is seen as a broad shoulder at 284 eV. The additional π^* molecular orbitals of both isomers make themselves felt as a broad peak at about 285.2 eV.

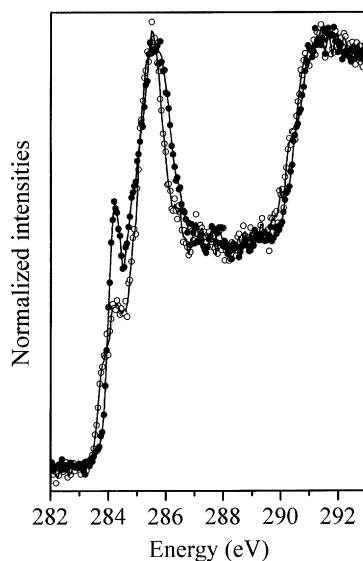


Fig. 57. C1s excitation spectra of the $C_{3v}(8)$ isomer (●) and $C_s(6)$ isomer (○) of Tm@C₈₂. The spectra are normalized to the σ^* edge at 290.5 eV.

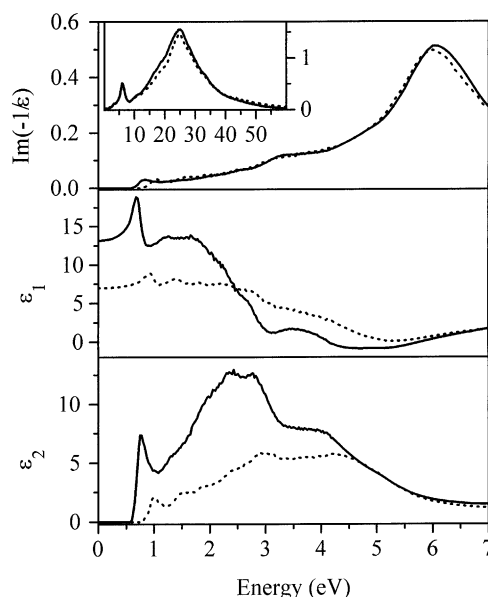


Fig. 58. Loss function ($\text{Im}(-1/\epsilon)$), real part (ϵ_1) and imaginary part (ϵ_2) of the dielectric function of the $\text{C}_{3v}(8)$ isomer (dotted line) and $\text{C}_s(6)$ isomer (solid line) of Tm@C_{82} .

Additional information on the optical properties of the two Tm@C_{82} isomers is obtained from a KKA of the loss function measured using EELS. The resulting real and imaginary part (ϵ_1 , ϵ_2) of the dielectric function are depicted in the lower panels of Fig. 58 [220]. The static background dielectric function at the low energy limit can be derived via extrapolation of the real part of the dielectric function. This value $\epsilon(0) \sim 7.3$ ($\text{C}_{3v}(8)$ isomer) and $\epsilon(0) \sim 12.8$ ($\text{C}_s(6)$ isomer) reflects all contributions to the static polarizability. The larger values of $\epsilon(0)$ compared to C_{60} ($\epsilon(0) \sim 4$) also indicate a higher static polarizability and reflect the fact that the onset of the interband transitions is at lower energy for the endohedral monometallofullerenes. The gap transitions of the two isomers significantly differ in energy. The onset for the $\text{C}_s(6)$ isomer is at ~ 0.6 eV, whereas that of the $\text{C}_{3v}(8)$ isomer is at ~ 0.8 eV. This shows that while the isomerization of the host carbon cage does not have a significant effect upon the valence of the endohedral Tm atom, it does play a defining role in the determination of the optical properties of the endohedral fullerene molecule as a whole. This is consistent with the differences observed in the UV–Vis–NIR spectra and the colors of the Tm@C_{82} isomers in solution [112]. As regards the energy region of the loss function where the $\pi \rightarrow \pi^*$ transitions contribute (below ~ 6 eV), the general spectral shape is quite similar to that for C_{60} . Due to the relatively low symmetry of these endohedral molecules, the fine structure is less clear and an assignment of the features visible in ϵ_2 to particular transitions between the occupied and unoccupied molecular orbitals is hardly possible.

7.3. K intercalated Tm@C_{82}

In the preceding sections various examples of the three different routes to dope fullerenes and their consequences have been discussed. It has been shown that all three ways of doping (intercalation, formation of heterofullerenes, endohedral doping) enable a controlled variation of the physical

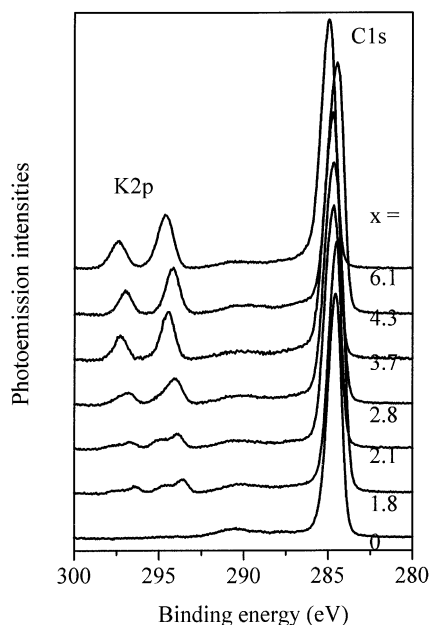


Fig. 59. C1s and K2p core level photoemission spectra of $K_xTm@C_{82}$ as a function of potassium content [223].

properties of fullerenes. A natural extension would be the combination of at least two of the three methods. This has been carried out for the $Tm@C_{82}$ isomer with $C_s(6)$ symmetry which in the solid phase was intercalated with potassium [223]. Fig. 59 shows the C1s and K2p core level photoemission spectra of $K_xTm@C_{82}$ as a function of potassium content. The potassium concentration x was calculated from the relative intensity of the C1s/K2p photoemission lines taking into account the photoionization cross-sections. For low doping concentrations ($x \leq 3$) the K2p levels are split into two doublets arising from two different interstitial lattice sites indicating the occupation of octahedral and tetrahedral interstitials. The K2p_{3/2} binding energies are 294.85 and 293.95 eV, respectively. At higher doping concentrations, only one K2p doublet is observed as it is expected for b.c.t. and b.c.c. structures. Compared to the well studied phase diagram of K_xC_{60} (see above) it is found that although the symmetry of the carbon cage is lower the intercalation process is very similar. Therefore at room temperature for $x \leq 2.5$ close-packed ('f.c.c.') molecular crystals are formed whereas crystals with b.c.t.- and/or b.c.c.-like structures are stable above this intercalation level. Moreover, for $x \leq 3$ the intensity of the two K2p doublets increases with intercalation but the ratio of $\frac{1}{2}$ between the octahedral and tetrahedral interstitials remains unchanged. This suggests a phase separation between only two stable phases, $Tm@C_{82}$ and $K_3Tm@C_{82}$ in this intercalation region.

For potassium concentrations $2.5 > x > 4$ an increasing amount of a new K2p component emerges with the K2p_{3/2} BE at 294.15 eV. This component corresponds to the occupation of tetrahedral sites in a body centered phase. For $x > 4$ up to the fully intercalated compound $K_6Tm@C_{82}$ the K2p BE is shifted to 294.45 eV. This indicates the formation of at least one new body centered phase, $K_6Tm@C_{82}$, in this intercalation region. However, from the close similarity of the doping process to K_xC_{60} , one can speculate about the existence of an additional body centered phase, e.g. with $K_4Tm@C_{82}$ stoichiometry. Since the photoemission features of the interstitials in the different body centered phases are at nearly

identical binding energies, it is not possible to unambiguously identify a possible stable phase with $x = 4$ from core level photoemission alone and only X-ray diffraction measurements can clarify this point. Further increasing the amount of potassium leads to the formation of a surface layer of potassium but no additional charge transfer or structural change is observed.

The valence band electronic structure of $K_xTm@C_{82}$ compounds was probed using HeI and monochromatic Al $K\alpha$ radiation. While, due to the different photoionization cross-sections, the latter measurements mainly probe the Tm4f multiplet and thus give access to the valence of the encaged Tm ion, the former provide information about the carbon derived DOS. Regarding the charge transfer from the encaged Tm to the fullerene molecule, no change of the Tm valence has been observed through the whole intercalation series [223]. The valence band photoemission spectra taken with HeI radiation are shown in Fig. 60. In photoemission spectra of pristine C_{82} the HOMO is visible as shoulder at 1.6 eV BE [87]. In the pristine metallofullerene $Tm@C_{82}$ of $C_s(6)$ symmetry the charge transfer of the two Tm6s electrons to the C_{82} molecules leads to the formation of a new HOMO which is visible in Fig. 60 as a pronounced peak at 1.5 eV BE. The deeper lying valence levels occur as features at 2, 3, 3.3 and 5.3 eV. Compared to metallofullerenes with a charge transfer bigger than 2 (e.g. $La@C_{82}$) we find no indication for an additional feature in the spectrum signalling the occupation of the LUMO + 1 of C_{82} by an extra electron. This is consistent with the divalent Tm ion inside C_{82} .

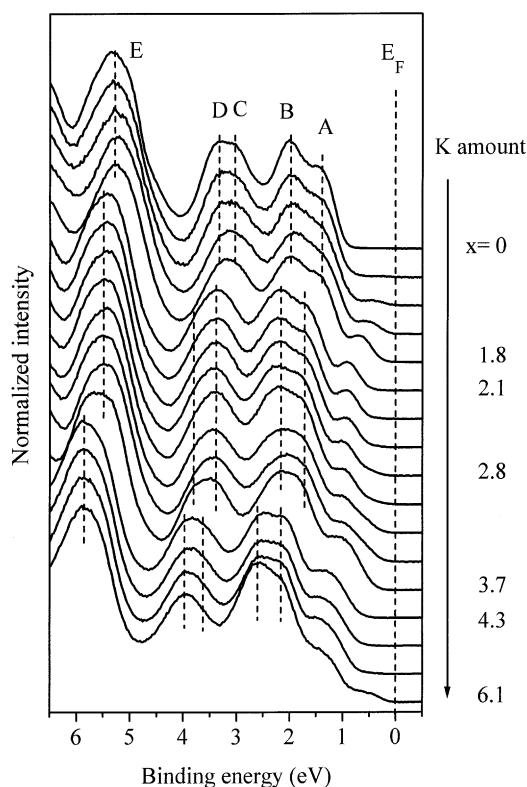


Fig. 60. Valence band photoemission spectra of $K_xTm@C_{82}$ as a function of potassium intercalation. The main valence band features are labeled A, B, C, D and E. The dashed lines illustrate the abrupt shift of the whole photoemission profile to higher binding energies at $x = 2$ and 4.

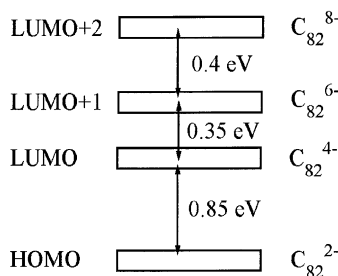


Fig. 61. Energy level diagram of the $C_{s(6)}$ isomer of C_{82} as derived from the photoemission studies of K intercalated $Tm@C_{82}$.

At low potassium intercalation a new structure appears at about 0.5 eV. Until a concentration of $x = 2$ the intensity of this feature is continuously growing and the maximum of spectral weight is shifted slightly to 0.65 eV BE. This behavior can be assigned to the filling of the LUMO derived bands of $Tm@C_{82}$ with the $K4s$ electrons. At a stoichiometry of $x = 2$ the whole photoemission spectrum abruptly shifts to higher BE by about 0.35 eV and above $x = 2$ a new feature at 0.5 eV starts to evolve. Until a potassium concentration of $x = 4$ the intensity of this new feature is steadily increasing while the maximum of spectral weight is shifted to 0.65 eV. This indicates the occupation of the LUMO + 2 derived bands of the $Tm@C_{82}$ molecular crystal. A further abrupt shift of 0.4 eV of the photoemission profiles occurs at about $x = 4$ and a structure at 0.6 eV starts to evolve up until the final equilibrium stoichiometry of $K_6Tm@C_{82}$ with a total charge transfer of eight electrons to the C_{82} cage is reached.

The subsequent filling of unoccupied levels and the sudden shifts to higher binding energies of the spectral features upon intercalation allows to identify the separation between the HOMO, LUMO, LUMO + 1 and LUMO + 2 levels of $Tm@C_{82}$ with $C_{s(6)}$ symmetry. The energy level separation in the charged C_{82} molecule is shown in Fig. 61. Such an experimentally derived energy diagram can be directly compared to the results of calculations and thus helps to decide which theoretical model is best suited to describe the electronic properties of fullerene molecules. Unfortunately, there are no calculations available as regards the C_s isomers of C_{82} , i.e. a more extended discussion of this point can only happen in the future.

None of the photoemission spectra shown in Fig. 60 shows emission from the Fermi level, i.e. none of the $K-Tm@C_{82}$ phases is metallic. This parallels the results for $K-C_{70}$ and the A_4C_{60} phases discussed above and again is most likely related to the strong electronic correlations combined with further aspects or mechanisms such as disorder or electron–phonon coupling, which all are present and important in the fullerene compounds and derivatives.

8. Single-wall carbon nanotubes

Carbon nanotubes are a new member of the growing family of novel fullerene-based materials, and represent a promising extension of this material class. The best system in which to investigate the intrinsic properties of this new material class are SWNTs. Macroscopic nanotube samples generally contain a distribution of tubes with different diameters and chirality and thus present the experimentalist with an averaged picture of their properties. Therefore, many studies have concentrated

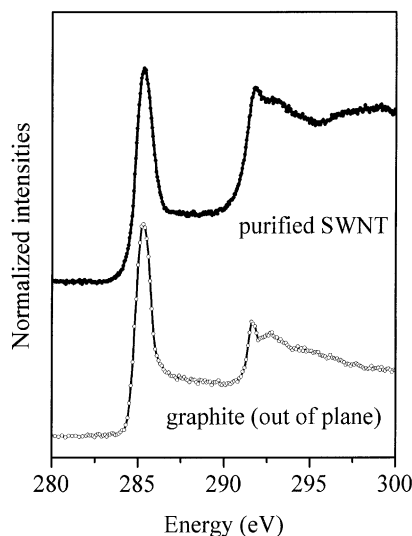


Fig. 62. C1s excitation spectra of purified SWNTs and highly oriented pyrolytic graphite (momentum transfer 'out of plane'). The curves are offset in y-direction.

on individual SWNTs. Transport measurements [105] and scanning tunneling spectroscopic (STS) and topographic (STM) studies of *single* nanotubes [103,104] have one much to determine some of the properties of SWNTs, e.g. by experimentally verifying the remarkable relationship between nanotube geometry and their electronic properties. During the first year of carbon nanotube research, much less has been done using methods that can be applied to macroscopic samples. One of the first studies on clean macroscopic samples has been carried out using EELS in transmission [224–226]. The results of these measurements are presented in the following.

In Fig. 62, the EELS C1s excitation spectrum of purified SWNT is compared to that of highly oriented pyrolytic graphite (HOPG, measured with the momentum transfer perpendicular to the graphite plane). In such a measurement, excitations of the core electron into unoccupied states with C2p character are probed. The spectrum of the SWNTs strongly resembles that of graphite. By comparison with directional-dependent C1s excitation measurements of HOPG [227,228], we see that the SWNT spectrum most closely resembles an average of the in-plane and out-of-plane graphite spectra. The predicted singularities in the unoccupied C2p-derived electronic states of the SWNTs [22,100,101] are conspicuous by their absence in Fig. 62. This fact is most probably due to the effect of the C1s core hole in the final state. In the case of C1s excitation spectroscopy of graphite, both the π^* [229–232] and σ^* [228,232] onsets are dominated by spectral weight resulting from the influence of the core hole. Thus, assuming a similar interaction between the excited electron and the core hole in SWNTs as in graphite, we can expect that the π^* resonances related to the DOS singularities of the different types of SWNTs are washed out, resulting in the broad peak centered at 285.2 eV.

In Fig. 63, the loss function ($\text{Im}(-1/\epsilon(q, E))$) for the purified SWNTs measured as a function of q is shown, after the subtraction of the quasi-elastic line. The inset shows the loss function for $q = 0.15 \text{ \AA}^{-1}$ over a wide energy range, in which the π plasmon, which represents the collective excitation of the π -electron system, can be clearly seen at an energy of 5.2 eV, and the $\sigma + \pi$ plasmon (the collective excitation of all valence electrons) at 21.5 eV. These values for SWNTs are in agreement with spatially-

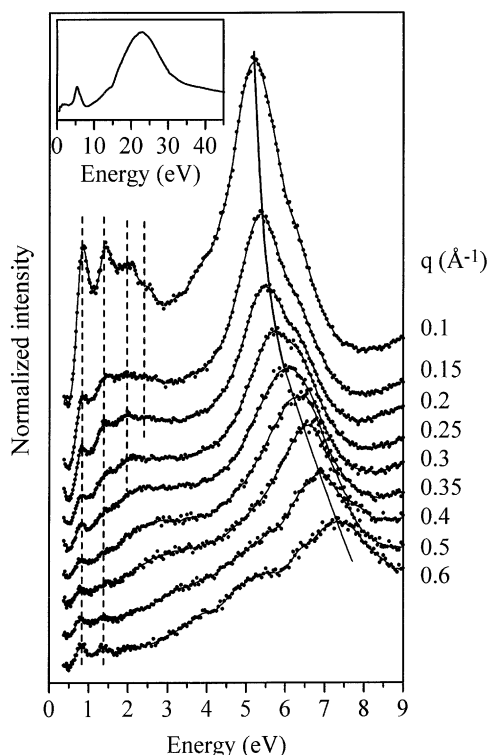


Fig. 63. The loss function of purified SWNTs from EELS in transmission for the different momentum transfers q shown. The contributions from the elastic peak have been subtracted. The inset contains the loss function over an extended energy range for $q = 0.15 \text{ \AA}^{-1}$, showing the π plasmon and the $\pi + \sigma$ plasmon at around 5 and 22 eV, respectively.

resolved EELS data measured using a transmission electron microscope [233], and they also confirm theoretical predictions that the π plasmon should occur in the energy range of 5–7 eV in the loss function of these materials [234–236]. Fig. 63 shows that it is possible to reliably measure the q -dependence of excitations in SWNTs with energies as low as 0.5 eV, which will be shown in the following to be vital to the understanding of their dielectric response. Furthermore, these data provide a wealth of information not accessible in spatially-resolved EELS measurements, in which the study of momentum-dependence is excluded and the broad quasi-elastic tail of the direct beam has only allowed the extraction of reliable information for energies above ~ 3 eV [233].

From the momentum dependence of the loss function, one can distinguish directly between features arising from localized or delocalized electronic states. Localized states give rise to a vanishingly small dispersion of peaks in the loss function as has been observed, e.g., for the features related to the interband excitations and both the π and $\pi + \sigma$ plasmons of C_{60} [144]. On the other hand, excitations between delocalized states generally exhibit a band structure dependent dispersion relation. Bearing these points in mind, the identification of excitations between localized and delocalized states in SWNTs is straightforward. At low momentum transfer, features in the loss function are visible at about 0.85, 1.45, 2.0, 2.55, 3.7, 5.2 and 6.4 eV whose origin lies in the π electron system of the SWNTs. However, two distinct behaviors of these features as a function of momentum transfer are observed. The

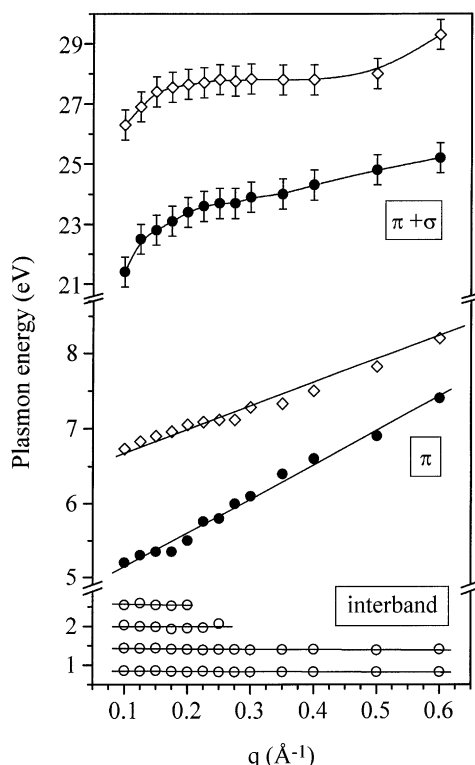


Fig. 64. The dispersion of the $\pi + \sigma$ plasmons (\bullet), and of the features arising from interband transitions between localized states (\circ) in purified SWNTs from EELS in transmission measurements. When invisible, the error bars are within the size of the symbols. For comparison the dispersion of the π and $\pi + \sigma$ plasmons in graphite for momentum transfers parallel to the planes is also shown (\diamond).

π plasmon disperses strongly from 5.2 eV at $q = 0.1 \text{ \AA}^{-1}$ to 7.4 eV at $q = 0.6 \text{ \AA}^{-1}$, whereas all the other peaks have a vanishingly small dispersion.

The momentum dependence of the peaks in the loss function resulting from the four lowest lying interband transitions of the SWNTs, as well as those of the π and $\pi + \sigma$ plasmons is summarized in Fig. 64. For comparison we also show the dispersion of the π and $\pi + \sigma$ plasmons of graphite with the momentum transfer parallel to the planes. The non-dispersive peaks in the loss function can be attributed to excitations between localized states which thus resemble molecular interband transitions such as those of C_{60} . In contrast, the π plasmon (at 5.2 eV for low momentum transfer), represents a plasma oscillation of delocalized states that are polarized along the nanotube axis. As can be seen from Fig. 64, the dispersion relations of both the π and the $\pi + \sigma$ plasmons in SWNTs and graphite are very similar, which confirms the graphitic nature of the axial electron-system in carbon nanotubes.

By carrying out a Kramer–Kronig analysis of the loss function the real (ϵ_1) and imaginary parts (ϵ_2) of the dielectric function have been derived. The results of such an analysis are depicted in the upper panels of Fig. 65 for C_{60} , SWNTs, and graphite (measured for the momentum transfer parallel to the graphite planes). In the lowest panel the corresponding real part of the optical conductivity is plotted, whereby $\sigma_r(E) = (E/\hbar)\epsilon_0\epsilon_2$ is a measure of the joint DOS. For the KKA of the SWNTs the loss function was normalized using an estimated $\epsilon_1(q, 0)$ [224].

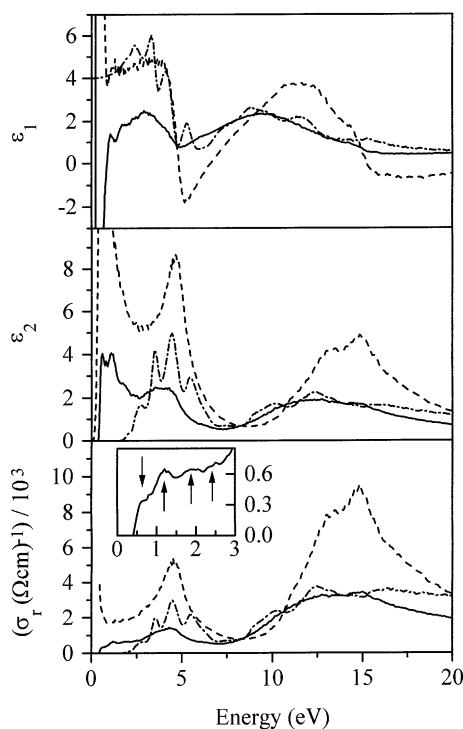


Fig. 65. The real and imaginary part of the dielectric function (upper panels) and the real part of the optical conductivity (σ_r) at low momentum transfer: SWNTs (solid line) at $q = 0.1 \text{ \AA}^{-1}$, C_{60} (dotted-dashed line) and graphite ('in plane' (dashed line)) at $q = 0.15 \text{ \AA}^{-1}$, respectively. The inset shows σ_r for the four lowest lying interband transitions of SWNTs in an expanded range.

In general, the optical conductivity of these sp^2 conjugated carbon systems shows peaks due to transitions between the (π/σ) and the (π^*/σ^*) electronic states. In C_{60} these peaks are very pronounced which is consistent with the high symmetry of the molecule and the weak, van der Waals interactions in the solid state, making C_{60} a prototypical zero-dimensional solid. In graphite three broad features are observed at 4.5 ± 0.05 , 13 ± 0.05 , and 15 ± 0.05 eV. Their breadth is an expression of the band-like nature of the electronic states in the graphite plane. For the SWNTs three broad features at energies slightly lower than those in graphite — i.e. 4.3 ± 0.1 , 11.7 ± 0.2 , and 14.6 ± 0.1 eV are found. Importantly, the optical conductivity of the SWNTs also exhibits additional structures at low energy. This region is shown in detail in the inset of Fig. 65, where three pronounced interband transitions are seen at energies of 0.65 ± 0.05 , 1.2 ± 0.1 and 1.8 ± 0.1 eV. Three further features, which are less pronounced, are located at 2.4 ± 0.2 , 3.1 ± 0.2 and 6.2 ± 0.1 eV.

As the SWNT data in the lowest panel (and inset) of Fig. 65 represent joint densities of states, one can directly relate the energy position of the features with the energetic separation of the van Hove singularities in the electronic DOS. It is known from X-ray diffraction that these samples of SWNTs have a narrow diameter distribution around a mean value of 1.4 nm [4]. The fact that we observe well defined, non-dispersive features in the EELS data confirms a narrow diameter distribution, as otherwise the sheer number of energetically different interband transitions would wash out all fine structure in this energy range, both in the loss function or in the optical conductivity.

The origin of the features at lowest energy (0.65 and 1.2 eV) is unambiguous — for the nanotube diameter range relevant here, only the gap transition and the transition between the next pair of DOS singularities in semiconducting nanotubes are predicted to lie at such energies [22,100,101]. Scanning tunneling spectroscopy experiments on single nanotubes have recently confirmed these predictions [103,104]. The peak appearing in the optical conductivity at 1.8 eV, corresponds directly to the ‘gap’ between the DOS singularities straddling the Fermi level which have been observed experimentally in scanning tunneling spectroscopy of metallic chiral and zig-zag tubes. Thus the feature at 1.8 eV in the optical conductivity clearly originates from metallic nanotubes. For the features at higher energies, an assignment based upon a discussion of particular nanotubes becomes less secure due to the large number of possible optically allowed transitions.

The results of EELS studies on SWNTs presented here show that they represent a text-book example of a system supporting both excitations between localized and delocalized electronic states. This parallels the situation found in conjugated polymers that are used in various organic devices [237]. Furthermore, it is clear that experimental studies on purified samples of carbon nanotubes can provide important insight into their physical properties despite the disordered nature of the samples available up to now. Studies of the lowest lying electronic excitations are additionally very helpful in the characterization of nanotube samples as regards the diameter distribution of the nanotubes.

9. Concluding remarks

In this paper, a summary of experimental work using high-energy spectroscopic tools has been presented, aimed at the determination and understanding of the electronic structure of carbon nanostructures: fullerenes, their compounds and derivatives, as well as carbon nanotubes. The wide range of fascinating physical and chemical properties of the fullerenes and carbon nanotubes is only matched by the wide range of important physical phenomena which need to be invoked to understand these properties. Thus, carbon nanostructures are ideal systems in which to study the interaction of such quantities as band formation, electronic degeneracy, electron correlation, electron–phonon coupling, charge transfer and low-dimensionality. In addition, it was shown that a variety of methods exist to engineer the electronic properties of the carbon nanostructures via doping, each of which effect the electronic structure in a characteristic manner and might lead to interesting properties with potential applications. In summary, the experimental investigations of the electronic structures of fullerenes and carbon nanotubes world-wide have been remarkably productive and resourceful such that we now possess a well-founded understanding of a number of these materials’ properties. Nevertheless, there are still a number of puzzles which remain to be solved, guaranteeing that carbon nanostructures will remain a guest in numerous spectrometers and computers for many years to come.

Acknowledgements

The work described here has been carried out at the Institut für Festkörperund Werkstofforschung (IFW) Dresden, the University of Minnesota in Minneapolis and the Forschungszentrum Karlsruhe (FZK). I appreciate the wide range of experimental techniques and the scientific and personal environment at these locations which were part of the basis of the numerous results summarized in this

paper. Most of the studies and the results presented above would not have been possible without many scientific collaborations and discussions with J. Fink, M.S. Golden, J.H. Weaver, O. Gunnarsson, W. Andreoni, V. Eyert, A.I. Liechtenstein, V.P. Antropov, E. Tosatti, G.A. Sawatzky, S.L. Drechsler, T. Pichler, X. Liu, J.F. Armbruster, S. Haffner, R. Friedlein, S. Schuppler, D.M. Poirier, F. Stepniak, H.A. Romberg, T.R. Cummins, M. Sing, E. Sohmen, and M. Roth, who all are gratefully acknowledged. Furthermore, the work would not have been possible without high-quality fullerene and carbon nanotube material. I am grateful to W. Krätschmer, M.M. Kappes, P. Adelmann, F. Wudl, L. Dunsch, K. Prassides, Y. Achiba, R.E. Smalley and their co-workers for the provision of purified and characterized samples. Part of the work has been supported by the European Commission (TMR research network FULPROP), the Deutsche Forschungsgemeinschaft (Graduiertenkolleg der TU Dresden, FI439/8-1), the Deutsche Akademische Austauschdienst, the Sächsische Staatsministerium für Wissenschaft und Kunst and the Bundesministerium für Bildung, Wissenschaft, Forschung und Technologie (13N6676/7).

References

- [1] H.W. Kroto, J.R. Heath, S.C. O'Brien, R.F. Curl, R.E. Smalley, *Nature* 318 (1985) 162.
- [2] W. Krätschmer, L.D. Lamb, K. Fostiropoulos, D.R. Huffman, *Nature* 347 (1989) 354.
- [3] S. Iijima, *Nature* 354 (1991) 56.
- [4] A. Thess, R. Lee, P. Nikolaev, H. Dai, P. Petit, J. Robert, C. Xu, Y.H. Lee, S.G. Kim, A.G. Rinzler, D.T. Colbert, G.E. Scuseria, D. Tomanek, J.E. Fischer, R.E. Smalley, *Science* 273 (1996) 483.
- [5] W.B. Choi, D.S. Chung, J.H. Kang, H.Y. Kim, Y.W. Jin, I.T. Han, Y.H. Lee, J.E. Jung, N.S. Lee, G.S. Park, J.M. Kim, *Appl. Phys. Lett.* 75 (1999) 3129.
- [6] Special issue: *Accounts Chem. Res.* 25 (1992).
- [7] Special issue: *Carbon* 8 (8) (1992).
- [8] Special issue: *J. Chem. Phys.* 53 (11) (1992).
- [9] D.S. Bethune, R.D. Johnson, J.R. Salem, M.S. de Vries, C.S. Yannoni, *Nature* 366 (1993) 123.
- [10] M.J. Rosseinsky, *J. Mater. Chem.* 5 (1995) 1497.
- [11] K. Tanigaki, K. Prassides, *J. Mater. Chem.* 5 (1995) 1515.
- [12] L. Degiorgi, *Mod. Phys. Lett. B* 9 (1995) 445.
- [13] H. Kuzmany, R. Winkler, T. Pichler, *J. Phys.: Condens. Matter* 7 (1995) 6601.
- [14] V. Buntar, H.W. Weber, *Supercond. Sci. Technol.* 9 (1996) 599.
- [15] O. Gunnarsson, *Rev. Mod. Phys.* 69 (1997) 575.
- [16] P. Petit, J. Robert, *Appl. Magn. Reson.* 11 (1996) 183.
- [17] L. Pintschovius, *Rep. Prog. Phys.* 57 (1996) 473.
- [18] J.H. Weaver, D.M. Poirier, in: H. Ehrenreich, F. Saepen (Eds.), *Solid State Physics*, Vol. 48, Academic Press, New York, 1994, p. 1.
- [19] W.E. Pickett, in: H. Ehrenreich, F. Saepen (Eds.), *Solid State Physics*, Vol. 48, Academic Press, New York, 1994, p. 225.
- [20] M.S. Golden, M. Knupfer, J. Fink, J.F. Armbruster, T.R. Cummins, H.A. Romberg, M. Roth, M. Sing, M. Schmidt, E. Sohmen, *J. Phys.: Condens. Matter* 7 (1995) 8219.
- [21] P. Rudolf, M.S. Golden, P.A. Brühwiler, *J. Electron Spectrosc. Relat. Phenom.* 100 (1999) 409.
- [22] R. Saito, G. Dresselhaus, M.S. Dresselhaus, *Physical Properties of Carbon Nanotubes*, Imperial College Press, London, 1998.
- [23] H. Prinzbach, A. Weiler, P. Landenberger, F. Wahl, J. Wörth, L.T. Scott, M. Gelmont, D. Olevano, B.v. Issendorff, *Nature* 407 (2000) 60.
- [24] C. Piskoti, J. Yarger, A. Zettl, *Nature* 393 (1998) 771.
- [25] R.C. Haddon, L.E. Brus, K. Raghavachari, *Chem. Phys. Lett.* 125 (1986) 459.

- [26] P.A. Heiney, J.A. Fischer, A.R. McGhie, W.J. Romanov, A.M. Denenstien, J.P. McCauley, A.B. Smith, D.E. Cox, *Phys. Rev. Lett.* 66 (1991) 2911.
- [27] S. Saito, A. Oshima, *Phys. Rev. Lett.* 66 (1991) 2637.
- [28] W.I.F. David, R.M. Ibberson, J.C. Matthewman, K. Prassides, T.J.S. Dennis, J.P. Hare, H.W. Kroto, R. Taylor, D.R.M. Walton, *Nature* 353 (1991) 147.
- [29] N. Troullier, J.L. Martins, *Phys. Rev. B* 46 (1992) 1754.
- [30] R.W. Lof, M.A. van Veenendaal, B. Koopmans, H.T. Jonkman, G.A. Sawatzky, *Phys. Rev. Lett.* 68 (1992) 3924.
- [31] M. Knupfer, D.M. Poirier, J.H. Weaver, *Phys. Rev. B* 49 (1994) 2281.
- [32] P. Brühwiler, A.J. Maxwell, N. Mårtensson, O. Gunnarsson, *Phys. Rev. B* 48 (1993) 18296.
- [33] K. Harigaya, *Phys. Rev. B* 45 (1992) 13676.
- [34] N. Manini, E. Tosatti, A. Auerbach, *Phys. Rev. B* 49 (1994) 13008.
- [35] O. Gunnarsson, *Phys. Rev. B* 51 (1995) 3493.
- [36] C.M. Varma, J. Zaanen, K. Raghavachari, *Science* 254 (1991) 989.
- [37] M. Schlüter, M. Lannoo, M. Needels, G.A. Baraff, *Phys. Rev. Lett.* 68 (1992) 526.
- [38] M. Fabrizio, E. Tosatti, *Phys. Rev. B* 55 (1997) 13465.
- [39] P.W. Stephens, L. Mihaly, P.L. Lee, R.L. Whetten, S.-M. Huang, R. Kaner, F. Diederich, K. Holczer, *Nature* 351 (1991) 632.
- [40] M.P. Gelfand, J.P. Lu, *Phys. Rev. Lett.* 68 (1992) 1050.
- [41] E.J. Mele, S.C. Erwin, *Phys. Rev. B* 50 (1994) 2150.
- [42] G.B.M. Vaughan, P.A. Heiney, J.E. Fischer, D.E. Luzzi, D.A. Richetts-Foot, W.J. Romanov, B.H. Allen, N. Coustel, J.P. McCauley, A.M. Smith III, *Science* 254 (1991) 1350.
- [43] M.A. Verheijen, H. Meekes, G. Meijer, P. Benema, J.L. de Boer, S. van Smaalen, G. van Tendeloo, S. Amelinckx, S. Muto, J. van Landuyt, *Chem. Phys.* 166 (1992) 287.
- [44] Y.Z. Li, J.C. Patrin, M. Chander, J.H. Weaver, K. Kikuchi, Y. Achiba, *Phys. Rev. B* 47 (1993) 10867.
- [45] J.F. Armbruster, H.A. Romberg, P. Schweiss, P. Adelman, M. Knupfer, J. Fink, R.H. Michel, J. Rockenberger, F. Hennrich, H. Schreiber, M.M. Kappes, *Z. Phys. B* 95 (1994) 469.
- [46] P.W. Fowler, D.E. Manolopoulos, *An Atlas of Fullerenes*, Clarendon Press, Oxford, 1995.
- [47] J.H. Schön, Ch. Kloc, R.C. Haddon, B. Batlogg, *Science* 288 (2000) 656.
- [48] R.C. Haddon, A.F. Hebard, M.J. Rosseinsky, D.W. Murphy, S.J. Duclos, K.B. Lyons, B. Miller, J.M. Rosamilia, R.M. Fleming, A.R. Kortan, S.H. Glarum, A.V. Makhija, A.J. Muller, R.H. Eick, S.M. Zahurak, R. Tycko, G. Dabbagh, F.A. Thiel, *Nature* 350 (1991) 320.
- [49] A.F. Hebard, M.J. Rosseinsky, R.C. Haddon, D.W. Murphy, S.H. Glarum, T.T.M. Palstra, A.P. Ramirez, A.R. Kortan, *Nature* 350 (1991) 600.
- [50] K. Holczer, O. Klein, S.-M. Huang, R.B. Kaner, K.-J. Fu, R.L. Whetten, F. Diederich, *Science* 252 (1991) 1154.
- [51] M.J. Rosseinsky, A.P. Ramirez, S.H. Glarum, D.W. Murphy, R.C. Haddon, A.F. Hebard, T.T.M. Palstra, A.R. Kortan, S.M. Zahurak, A.V. Makhija, *Phys. Rev. Lett.* 66 (1991) 2380.
- [52] K. Tanigaki, T.W. Ebbesen, S. Saito, J. Mizuki, J.S. Tsai, Y. Kubo, S. Kuroshima, *Nature* 352 (1991) 222.
- [53] A.R. Kortan, N. Kopylov, S. Glarum, E.M. Gyorgy, A.P. Ramirez, R.M. Fleming, F.A. Thiel, R.C. Haddon, *Nature* 355 (1992) 529.
- [54] A.R. Kortan, N. Kopylov, S. Glarum, E.M. Gyorgy, A.P. Ramirez, R.M. Fleming, O. Zhou, F.A. Thiel, P.L. Tervot, R.C. Haddon, *Nature* 360 (1992) 566.
- [55] A.R. Kortan, N. Kopylov, E. Ozdas, A.P. Ramirez, R.M. Fleming, R.C. Haddon, *Chem. Phys. Lett.* 223 (1994) 501.
- [56] M. Baenitz, M. Heinze, K. Lueders, H. Werner, R. Schloegl, M. Weiden, G. Sparr, F. Steglich, *Solid State Commun.* 96 (1995) 539.
- [57] Y. Iwasa, M. Kawaguchi, S. Taga, T. Takenobu, T. Mitani, K. Prassides, C.M. Brown, *Electrochem. Soc. Proc.* 98 (8) (1998) 428.
- [58] P.M. Allemand, K.C. Khemani, A. Koch, F. Wudl, K. Holczer, S. Donava, G. Gruner, J.D. Thompson, *Science* 253 (1991) 301.
- [59] A. Lappas, K. Prassides, K. Vavakis, D. Arcon, R. Blinc, P. Cevc, A. Amato, R. Feyerherm, F.N. Gygax, A. Schenck, *Science* 267 (1991) 1799.
- [60] B. Koopmans, A.M. Janner, H.T. Jonkman, G.A. Sawatzky, F. van der Woude, *Phys. Rev. Lett.* 71 (1993) 3569.
- [61] B. Koopmans, A. Anema, H.T. Jonkman, G.A. Sawatzky, F. van der Woude, *Phys. Rev. B* 48 (1993) 2759.

- [62] A.M. Janner, R. Eder, B. Koopmans, H.T. Jonkman, G.A. Sawatzky, *Phys. Rev. B* 52 (1996) 17158.
- [63] P.W. Stephens, G. Bortel, G. Faigel, M. Tezge, A. Janossy, S. Pekker, G. Oszlanyi, L. Forro, *Nature* 370 (1994) 636.
- [64] G. Oszlanyi, G. Baumgartner, G. Faigel, L. Forro, *Phys. Rev. Lett.* 78 (1997) 4438.
- [65] D.L. Lichtenberger, K.W. Nebesny, C.D. Ray, D.R. Huffman, L.D. Lamb, *Chem. Phys. Lett.* 176 (1991) 203.
- [66] R.M. Fleming, M.J. Rosseinsky, A.P. Ramirez, D.W. Murphy, J.C. Tully, R.C. Haddon, T. Siegrist, R. Tycko, S.H. Glarum, P. Marsh, G. Dabbagh, S.M. Zahurak, A.V. Makhija, C. Hampton, *Nature* 352 (1991) 701.
- [67] D.M. Poirier, D.W. Owens, J.H. Weaver, *Phys. Rev. B* 51 (1995) 1830.
- [68] M. Kobayashi, Y. Akahama, H. Kawamura, H. Shinohara, H. Sato, Y. Saito, *Phys. Rev. B* 48 (1993) 16877.
- [69] M. Knupfer, D.M. Poirier, J.H. Weaver, *Phys. Rev. B* 49 (1994) 8464.
- [70] D.M. Poirier, J.H. Weaver, K. Kikuchi, Y. Achiba, *Z. Phys. D* 26 (1993) 79.
- [71] S. Hino, K. Matsumoto, S. Hasegawa, K. Kamiya, H. Inokuchi, T. Morikawa, T. Takahashi, K. Seki, K. Kikuchi, S. Suzuki, I. Ikemoto, Y. Achiba, *Chem. Phys. Lett.* 190 (1992) 169.
- [72] S. Hino, K. Matsumoto, S. Hasegawa, H. Inokuchi, T. Morikawa, T. Takahashi, K. Seki, K. Kikuchi, S. Suzuki, I. Ikemoto, Y. Achiba, *Chem. Phys. Lett.* 197 (1992) 38.
- [73] E. Sohmen, J. Fink, *Phys. Rev. B* 47 (1993) 14532.
- [74] S. Hino, K. Matsumoto, S. Hasegawa, K. Iwasaki, K. Yakushi, T. Morikawa, T. Takahashi, K. Seki, *Phys. Rev. B* 47 (1993) 8418.
- [75] T.R. Cummins, M. Bürk, M. Schmidt, J.F. Armbruster, D. Fuchs, P. Adelman, S. Schuppler, R.H. Michel, M.M. Kappes, *Chem. Phys. Lett.* 261 (1996) 228.
- [76] K. Iwasaki, K. Umishita, S. Hino, T. Miyamae, K. Kikuchi, Y. Achiba, *Phys. Rev. B* 60 (1999) 5044.
- [77] T. Guo, C. Jin, R.E. Smalley, *J. Phys. Chem.* 95 (1991) 4948.
- [78] T. Pradeep, V. Vijayakrishnan, A.K. Santra, C.N.R. Rao, *J. Phys. Chem.* 95 (1991) 10564.
- [79] J.C. Hummelen, B. Knight, J. Pavlovich, R. Gonzales, F. Wudl, *Science* 269 (1995) 1554.
- [80] C.M. Brown, L. Cristofolini, K. Kordatos, K. Prassides, C. Bellavia-Lund, R. Gonzales, M.-K. Keshavarz, F. Wudl, A.K. Cheetham, J.P. Zhang, W. Andreoni, A. Curioni, A.N. Fitch, P. Pattison, *Chem. Mater.* 8 (1996) 2548.
- [81] W. Andreoni, A. Curioni, K. Holczer, K. Prassides, M.-K. Keshavarz, J.C. Hummelen, F. Wudl, *J. Am. Chem. Soc.* 118 (1996) 11335.
- [82] K. Prassides, M.-K. Keshavarz, J.C. Hummelen, W. Andreoni, P. Giannozzi, E. Beer, C. Bellavia-Lund, L. Cristofolini, R. Gonzalez, A. Lappas, Y. Murata, M. Malecki, V. Srdanov, F. Wudl, *Science* 271 (1996) 1833.
- [83] M. Saunders, H.A. Jimenez-Vasquez, R.J. Cross, R.J. Poreda, *Science* 259 (1993) 1428.
- [84] T. Almeida-Murphy, Ch. Wolf, B. Pietzak, A. Weidinger, Th. Pawlik, J.-M. Spaeth, M. Höhne, in: H. Kuzmany, F. Fink, M. Mehring, S. Roth (Eds.), *Fullerenes and Fullerene Nanostructures*, World Scientific, Singapore, 1996, p. 191.
- [85] M. Takata, B. Umeda, E. Nishibori, M. Sakata, Y. Saito, M. Ohno, H. Shinohara, *Nature* 377 (1995) 46.
- [86] J.H. Weaver, Y. Chai, G.H. Kroll, C. Jin, T.R. Ohno, R.E. Haufler, T. Guo, J.M. Alford, J. Conceicao, L.P.F. Chibante, A. Jain, G. Palmer, R.E. Smalley, *Chem. Phys. Lett.* 190 (1992) 460.
- [87] D.M. Poirier, M. Knupfer, J.H. Weaver, W. Andreoni, K. Laasonen, M. Parrinello, D.S. Bethune, K. Kikuchi, Y. Achiba, *Phys. Rev. B* 49 (1994) 17403.
- [88] B. Kessler, A. Bringer, S. Cramm, C. Schlebusch, W. Eberhardt, S. Suzuki, Y. Achiba, F. Esch, M. Barnaba, D. Cocca, *Phys. Rev. Lett.* 79 (1997) 2289.
- [89] M.R. Falvo, G.J. Clary, R.M. Taylor II, V. Chi, F.P. Brooks Jr., S. Washburn, R. Superfine, *Nature* 389 (1997) 582.
- [90] P.M. Ajayan, S. Iijima, *Nature* 361 (1993) 333.
- [91] P.M. Ajayan, T.W. Ebbesen, T. Ichihashi, S. Iijima, K. Tanigaki, H. Hiura, *Nature* 362 (1993) 522.
- [92] D.S. Bethune, C.H. Kiang, M.S. Devries, G. Gorman, R. Savoy, J. Vazquez, R. Beyers, *Nature* 363 (1993) 605.
- [93] S. Iijima, T. Ichihashi, *Nature* 363 (1993) 603.
- [94] A.M. Rao, E. Richter, S. Bandow, B. Chase, P.C. Eklund, K.A. Williams, S. Fang, K.R. Subbaswamy, M. Menon, A. Thess, R.E. Smalley, G. Dresselhaus, M.S. Dresselhaus, *Science* 275 (1997) 187.
- [95] S. Bandow, S. Asaka, Y. Saito, A.M. Rao, L. Grigorian, E. Richter, P.C. Eklund, *Phys. Rev. Lett.* 80 (1998) 3779.
- [96] O. Jost, A.A. Gorbunov, W. Pompe, T. Pichler, R. Friedlein, M. Knupfer, M. Reibold, H.-D. Bauer, L. Dunsch, M.S. Golden, J. Fink, *Appl. Phys. Lett.* 75 (1999) 2217.
- [97] C. Journet, W.K. Maser, P. Bernier, A. Loiseau, M. Lamy de Chapelle, S. Lefrant, P. Deniard, R. Lee, J.E. Fischer, *Nature* 388 (1997) 756.
- [98] H. Dai, A. Rinzler, P. Nikolaev, A. Thess, D.T. Colbert, R.E. Smalley, *Chem. Phys. Lett.* 260 (1996) 471.

- [99] J.W. Mintmire, C.T. White, *Phys. Rev. Lett.* 81 (1998) 2506.
- [100] J.W. Mintmire, B.I. Dunlap, C.T. White, *Phys. Rev. Lett.* 68 (1992) 631.
- [101] N. Hamada, S. Sawada, A. Oshiyama, *Phys. Rev. Lett.* 68 (1992) 1579.
- [102] J.-C. Charlier, J.-P. Issi, *Appl. Phys. A* 67 (1998) 79.
- [103] J.W.G. Wildoer, L.C. Venema, A.G. Rinzier, R.E. Smalley, C. Dekker, *Nature* 391 (1998) 59.
- [104] T.W. Odom, J.L. Huang, P. Kim, C.M. Lieber, *Nature* 391 (1998) 62.
- [105] S.J. Tans, M.H. Devoret, H. Dai, A. Thess, R.E. Smalley, L.J. Geerlings, C. Dekker, *Nature* 386 (1998) 474.
- [106] M. Bockrath, D.H. Cobden, P.L. McEuen, N.G. Chopra, A. Zettl, A. Thess, R.E. Smalley, *Science* 275 (1997) 1922.
- [107] R.S. Lee, H.J. Kim, J.E. Fischer, A. Thess, R.E. Smalley, *Nature* 388 (1997) 255.
- [108] A.M. Rao, P.C. Eklund, S. Bandow, A. Thess, R.E. Smalley, *Nature* 388 (1997) 257.
- [109] C. Bower, S. Suzuki, K. Tanigaki, O. Zhou, *Appl. Phys. A* 67 (1998) 47.
- [110] T. Pichler, M. Sing, M. Knupfer, M.S. Golden, J. Fink, *Solid State Commun.* 109 (1999) 721.
- [111] R.H. Michel, Ph.D. Thesis, University of Karlsruhe, 1996.
- [112] U. Kirbach, L. Dunsch, *Angew. Chem. Int. Ed. Engl.* 35 (1996) 2380.
- [113] S. Suzuki, S. Kawata, H. Shiromaru, K. Yamauchi, K. Kikuchi, T. Kato, Y. Achiba, *J. Phys. Chem.* 96 (1992) 7159.
- [114] K. Kikuchi, S. Suzuki, Y. Nakao, N. Nakahara, T. Wakabayashi, H. Shiromaru, S. Kazuya, I. Ikemoto, Y. Achiba, *Chem. Phys. Lett.* 216 (1993) 67.
- [115] J.C. Hummelen, M. Prato, F. Wudl, *J. Am. Chem. Soc.* 117 (1995) 7003.
- [116] A.G. Rinzier, J. Liu, H. Dai, P. Nikolaev, C.B. Huffman, F.J. Rodriguez-Macias, P.J. Boul, A.H. Lu, D. Heyman, D.T. Colbert, R.S. Lee, J.E. Fischer, A.M. Rao, P.C. Eklund, R.E. Smalley, *Appl. Phys. A* 67 (1998) 29.
- [117] D.M. Poirier, *Appl. Phys. Lett.* 64 (1994) 1356.
- [118] M. Knupfer, J. Fink, J.F. Armbruster, H.A. Romberg, *Z. Phys. B* 98 (1995) 9.
- [119] J. Fink, *Adv. Electron. Electron Phys.* 75 (1989) 121.
- [120] J. Stöhr, *NEXAFS Spectroscopy*, Springer, Berlin, 1992.
- [121] R. Ahuja, P.A. Brühwiler, J.M. Wills, B. Johansson, N. Martensson, O. Eriksson, *Phys. Rev. B* 54 (1996) 14396.
- [122] M. Nyberg, Y. Luo, L. Triguero, L.G.M. Pettersson, H. Agren, *Phys. Rev. B* 60 (1999) 7956.
- [123] M. Knupfer, T. Pichler, M.S. Golden, J. Fink, M. Murgia, R.H. Michel, R. Zamboni, C. Taliani, *Phys. Rev. Lett.* 83 (1999) 1443.
- [124] M. Knupfer, J. Fink, *Phys. Rev. B* 60 (1999) 10731.
- [125] M. Knupfer, J. Fink, E. Zojer, G. Leising, D. Fichou, *Chem. Phys. Lett.* 318 (2000) 585.
- [126] M. Knupfer, J. Fink, E. Zojer, G. Leising, J.L. Bredas, *Phys. Rev. B* 61 (2000) 1662.
- [127] S. Hüfner, *Photoelectron Spectroscopy*, Springer, Berlin, 1995.
- [128] H. Petersen, C. Jung, C. Hellwig, W.B. Peatman, W. Gudat, *Rev. Sci. Instrum.* 66 (1995) 1.
- [129] M. Merkel, M. Knupfer, M.S. Golden, J. Fink, R. Seemann, R.L. Johnson, *Phys. Rev. B* 47 (1993) 11470.
- [130] M.S. Golden, M. Knupfer, J. Fink, J.F. Armbruster, T.R. Cummins, H.A. Romberg, M. Roth, M. Schmidt, M. Sing, E. Sohmen, R. Michel, F. Hennrich, J. Rockenberger, M.M. Kappes, D.R.C. Hoad, A.J. Roberts, W.R. Flavell, M. Roper, M. Surman, D.A. Teehan, *Mol. Mater.* 4 (1994) 51.
- [131] M. Knupfer, O. Knauff, M.S. Golden, J. Fink, M. Bürk, D. Fuchs, S. Schuppler, R.H. Michel, M.M. Kappes, *Chem. Phys. Lett.* 258 (1996) 513.
- [132] J.F. Armbruster, M. Roth, H.A. Romberg, M. Sing, M. Schmidt, P. Schweiss, P. Adelmann, M.S. Golden, J. Fink, R.H. Michel, J. Rockenberger, F. Hennrich, M.M. Kappes, *Phys. Rev. B* 50 (1994) 4933.
- [133] J.H. Weaver, J.L. Martins, T. Komeda, Y. Chen, T.R. Ohno, G.H. Kroll, N. Troullier, R.E. Haufler, R.E. Smalley, *Phys. Rev. Lett.* 66 (1991) 1741.
- [134] C.T. Chen, L.H. Tjeng, P. Rudolf, G. Meigs, J.E. Rowe, J. Chen, J.P. McCauley, A.B. Smith, A.R. McGhie, W.J. Romanov, W.E. Plummer, *Nature* 352 (1991) 603.
- [135] G.K. Wertheim, J.E. Rowe, D.N.E. Buchanan, E.E. Chaban, A.F. Hebard, A.R. Kortan, A.V. Makhija, R.C. Haddon, *Science* 252 (1991) 1419.
- [136] D.L. Lichtenberger, M.E. Jatcko, K.W. Nebesny, C.D. Ray, D.R. Huffman, L.D. Lamb, *Mater. Res. Soc. Symp. Proc.* 206 (1991) 673.
- [137] A.J. Stones, D.J. Wales, *Chem. Phys. Lett.* 128 (1986) 501.
- [138] S. Saito, S. Okada, S. Saeda, N. Hamada, *Phys. Rev. Lett.* 75 (1995) 685.
- [139] J.C. Nilesand, X.Q. Wang, *J. Chem. Phys.* 103 (1995) 7040.

- [140] D.L. Lichtenberger, M.E. Rempe, B. Gogosha, *Chem. Phys. Lett.* 198 (1992) 454.
- [141] M.B. Jost, N. Troullier, D.M. Poirier, J.-L. Martins, J.H. Weaver, L.P.F. Chibante, R.E. Smalley, *Phys. Rev. B* 44 (1991) 1966.
- [142] B. Wästberg, S. Lunell, C. Enkvist, P.A. Brühwiler, A.J. Maxwell, N. Martensson, *Phys. Rev. B* 50 (1994) 13031.
- [143] E.L. Shirley, S.G. Louie, *Phys. Rev. Lett.* 71 (1993) 133.
- [144] H. Romberg, E. Sohmen, M. Merkel, M. Knupfer, M. Alexander, M.S. Golden, P. Adelman, T. Pietrus, J. Fink, R. Seemann, R.L. Johnson, *Syn. Met.* 55–57 (1993) 3038.
- [145] M. Muccini, H. Schlaich, J. Feldmann, H. Bässler, E.O. Göbel, R. Zamboni, C. Taliani, J. Erxmeier, A. Weidinger, *Syn. Met.* 77 (1996) 177.
- [146] F. Negri, G. Orlandi, F. Zerbetto, *J. Chem. Phys.* 97 (1992) 6496.
- [147] E.L. Shirley, L.X. Benedict, S.G. Louie, *Phys. Rev. B* 54 (1996) 10970.
- [148] S. Kazaoui, N. Minami, Y. Tanabe, H.J. Byrne, A. Eilmes, P. Petelenz, *Phys. Rev. B* 58 (1998) 7689.
- [149] G. Gensterblum, L.-M. Yu, J.J. Pireaux, P.A. Thiry, R. Caudano, J.P. Vigneron, Ph. Lambin, A.A. Lucas, W. Krätschmer, *Phys. Rev. Lett.* 67 (1991) 2171.
- [150] P.J. Benning, D.M. Poirier, T.R. Ohno, Y. Chen, M.B. Jost, F. Stepniak, G.H. Kroll, J.H. Weaver, J. Fure, R.E. Smalley, *Phys. Rev. B* 45 (1992) 6899.
- [151] R.E. Haufler, L.S. Wang, L.P.F. Chibante, C. Jin, J. Conceicao, Y. Chai, R.E. Smalley, *Chem. Phys. Lett.* 179 (1991) 449.
- [152] M. Knupfer, M. Merkel, M.S. Golden, J. Fink, O. Gunnarsson, V.P. Antropov, *Phys. Rev. B* 47 (1993) 13944.
- [153] M. Knupfer, J.F. Armbruster, H.A. Romberg, J. Fink, *Syn. Met.* 70 (1995) 1321.
- [154] E. Sohmen, J. Fink, W. Krätschmer, *Europhys. Lett.* 17 (1992) 51.
- [155] Y. Iwasa, T. Kaneyasu, *Phys. Rev. B* 51 (1995) 3678.
- [156] P.J. Benning, F. Stepniak, D.M. Poirier, J.L. Martins, J.H. Weaver, L.P.F. Chibante, R.E. Smalley, *Phys. Rev. B* 47 (1993) 13843.
- [157] M. De Seta, F. Evangelisti, *Phys. Rev. Lett.* 71 (1993) 2477.
- [158] F. Stepniak, P.J. Benning, D.M. Poirier, J.H. Weaver, *Phys. Rev. B* 48 (1993) 1899.
- [159] R.C. Haddon, A.S. Perel, R.C. Morris, S.-H. Chang, A.T. Fiory, A.F. Hebard, T.T.M. Palstra, G.P. Kochanski, *Chem. Phys. Lett.* 218 (1994) 100.
- [160] T. Yildirim, L. Barbette, J.E. Fischer, C.L. Lin, J. Robert, P. Petit, T.T.M. Palstra, *Phys. Rev. Lett.* 77 (1996) 167.
- [161] O. Gunnarsson, H. Handschuh, P.S. Bechthold, B. Kessler, G. Ganteför, W. Eberhardt, *Phys. Rev. Lett.* 74 (1995) 1875.
- [162] V.P. Antropov, O. Gunnarsson, A.I. Liechtenstein, *Phys. Rev. B* 48 (1993) 7651.
- [163] G.A. Sawatzky, in: H. Kuzmany, J. Fink, M. Mehring, S. Roth (Eds.), *Physics and Chemistry of Fullerenes and Derivatives*, World Scientific, Singapore, 1995, p. 373.
- [164] O. Gunnarsson, *Z. Phys. B* 104 (1997) 279.
- [165] A. Ceulemans, L.F. Chibotaru, F. Cimpoeșu, *Phys. Rev. Lett.* 78 (1997) 3725.
- [166] T.R. Cummins, J.F. Armbruster, M.S. Golden, M. Knupfer, H.A. Romberg, M. Sing, J. Fink, *Physica C* 235–240 (1994) 2491.
- [167] O. Gunnarsson, J.E. Han, *Nature* 405 (2000) 1027.
- [168] R. Hesper, L.H. Tjeng, A. Heeres, G.A. Sawatzky, *Phys. Rev. Lett.* 85 (2000) 1970.
- [169] T. Tsubo, K. Nasu, *Solid State Commun.* 91 (1994) 907.
- [170] J. Van den Brink, O. Gunnarsson, V. Eyert, *Phys. Rev. B* 57 (1998) 2163.
- [171] O. Gunnarsson, A.I. Liechtenstein, V. Eyert, M. Knupfer, J. Fink, J.F. Armbruster, *Phys. Rev. B* 53 (1996) 3455.
- [172] O. Gunnarsson, V. Eyert, M. Knupfer, J. Fink, J.F. Armbruster, *J. Phys.: Condens. Matter* 8 (1996) 2557.
- [173] A.I. Liechtenstein, O. Gunnarsson, M. Knupfer, J. Fink, J.F. Armbruster, *J. Phys.: Condens. Matter* 8 (1996) 4001.
- [174] H. Raether, *Excitations of Plasmons and Interband Transitions by Electrons*, Springer, Berlin, 1980.
- [175] V.V. Kresin, V.Z. Kresin, *Phys. Rev. B* 49 (1994) 2715.
- [176] R.F. Kiefl, T.L. Duty, J.W. Schneider, A. MacFarlane, K. Chow, J.W. Elzey, P. Mendels, G.D. Morris, J.H. Brewer, E.J. Ansaldo, C. Niedermayer, D.R. Noakes, C.E. Stronach, B. Hitti, J.E. Fischer, *Phys. Rev. Lett.* 69 (1992) 2005.
- [177] S.C. Erwin, C. Bruder, *Physica B* 199/200 (1994) 600.
- [178] J.P. Lu, *Phys. Rev. B* 49 (1994) 5687.
- [179] Y. Iwasa, T. Kaneyasu, M. Nagata, N. Mizutani, *Syn. Met.* 70 (1995) 1361.

- [180] R. Kerkoud, P. Auban-Senzier, D. Jerome, S. Brazovskii, N. Kirova, I. Lukyanchuk, F. Rachdi, C. Goze, *Syn. Met.* 77 (1996) 205.
- [181] M. Knupfer, J. Fink, *Phys. Rev. Lett.* 79 (1997) 2714.
- [182] G. Ruani, P. Guptasarma, C. Taliani, J. Fischer, *Physica C* 235–240 (1994) 2477.
- [183] M. Knupfer, J. Fink, J.F. Armbruster, *Z. Phys. B* 101 (1996) 57.
- [184] S.C. Erwin, W.E. Pickett, *Science* 254 (1991) 842.
- [185] M.J. Rosseinsky, D.W. Murphy, R.M. Fleming, R. Tycko, A.P. Ramirez, T. Siegrist, G. Dabbagh, S.E. Barret, *Nature* 356 (1992) 416.
- [186] O. Gunnarsson, E. Koch, R.M. Martin, *Phys. Rev. B* 54 (1996) R11026.
- [187] W.A. Harrison, *Electronic Structure and the Properties of Solids*, Dover, New York, 1992.
- [188] L.F. Chibotaru, A. Ceulemans, S.P. Cojocaru, *Phys. Rev. B* 59 (1999) R12728.
- [189] J.E. Han, E. Koch, O. Gunnarsson, *Phys. Rev. Lett.* 84 (2000) 1276.
- [190] Y. Iwasa, H. Shimoda, T.T.M. Palstra, Y. Maniwa, O. Zhou, T. Mitani, *Phys. Rev. B* 53 (1996) R8836.
- [191] S.L. Ren, K.A. Wang, Y. Zhou, A.M. Rhao, M.S. Meier, J.P. Selegue, P.C. Eklund, *Appl. Phys. Lett.* 61 (1992) 124.
- [192] W. Andreoni, F. Gygi, M. Parrinello, *Chem. Phys. Lett.* 189 (1992) 241.
- [193] T. Yildirim, O. Zhou, J.E. Fischer, N. Bykovetz, R.A. Strongin, M.A. Cichy, A.B. Smith III, C.L. Lin, R. Jelinek, *Nature* 360 (1992) 568.
- [194] W. Andreoni, P. Giannozzi, J.F. Armbruster, M. Knupfer, J. Fink, *Europhys. Lett.* 34 (1996) 699.
- [195] J.F. Armbruster, M. Knupfer, J. Fink, *Z. Phys. B* 102 (1997) 55.
- [196] W. Andreoni, P. Giannozzi, M. Parrinello, *Phys. Rev. Lett.* 72 (1994) 848.
- [197] L.Q. Jiang, B.E. Koel, *Phys. Rev. Lett.* 72 (1994) 140.
- [198] Y. Chen, F. Stepniak, J.H. Weaver, L.P.F. Chibante, R.E. Smalley, *Phys. Rev. B* 45 (1992) 8845.
- [199] Y. Chen, D.M. Poirier, M.B. Jost, C. Gu, T.R. Ohno, J.L. Martins, J.H. Weaver, L.P.F. Chibante, R.E. Smalley, *Phys. Rev. B* 46 (1992) 7961.
- [200] G.K. Wertheim, D.N.E. Buchanan, J.E. Rowe, *Science* 258 (1992) 1638.
- [201] G.K. Wertheim, D.N.E. Buchanan, *J. Phys. Chem. Solids* 56 (1995) 745.
- [202] R.C. Haddon, G.P. Kochanski, A.F. Hebard, A.T. Fiory, R.C. Morris, *Science* 258 (1992) 1636.
- [203] S. Saito, A. Oshiyama, *Solid State Commun.* 83 (1992) 107.
- [204] H. Romberg, M. Roth, J. Fink, *Phys. Rev. B* 49 (1994) 1427.
- [205] M. Knupfer, F. Stepniak, J.H. Weaver, *Phys. Rev. B* 49 (1994) 7620.
- [206] R.C. Haddon, G.P. Kochanski, A.F. Hebard, A.T. Fiory, R.C. Morris, A.S. Perel, *Chem. Phys. Lett.* 203 (1993) 433.
- [207] S.C. Erwin, M.R. Pederson, *Phys. Rev. B* 47 (1993) 14657.
- [208] S. Saito, A. Oshiyama, *Phys. Rev. Lett.* 71 (1993) 121.
- [209] K. Umemoto, S. Saito, *Phys. Rev. B* 61 (2000) 14204.
- [210] Th. Schedel-Niedrig, M.C. Böhm, H. Werner, J. Schulte, R. Schlögl, *Phys. Rev. B* 55 (1997) 13542.
- [211] T. Pichler, M. Knupfer, M.S. Golden, S. Haffner, R. Friedlein, J. Fink, W. Andreoni, A. Curioni, M.-K. Keshavarz, C. Bellavia-Lund, A. Sastre, J.-C. Hummelen, F. Wudl, *Phys. Rev. Lett.* 78 (1997) 4249.
- [212] S. Haffner, T. Pichler, M. Knupfer, B. Umlauf, R. Friedlein, M.S. Golden, J. Fink, M.-K. Keshavarz, C. Bellavia-Lund, A. Sastre, J.-C. Hummelen, F. Wudl, *Eur. Phys. J. B* 1 (1998) 11.
- [213] W. Andreoni, F. Gygi, M. Parrinello, *Chem. Phys. Lett.* 190 (1992) 159.
- [214] T. Pichler, M. Knupfer, R. Friedlein, S. Haffner, B. Umlauf, M.S. Golden, O. Knauff, H.-D. Bauer, J. Fink, M.-K. Keshavarz, C. Bellavia-Lund, A. Sastre, J.-C. Hummelen, F. Wudl, *Syn. Met.* 86 (1997) 2313.
- [215] T. Pichler, M. Knupfer, M.S. Golden, J. Fink, J. Winter, M. Haluska, H. Kuzmany, M.-K. Keshavarz, C. Bellavia-Lund, A. Sastre, J.-C. Hummelen, F. Wudl, *Appl. Phys. A* 64 (1997) 301.
- [216] D.M. Poirier, C.G. Olson, J.H. Weaver, *Phys. Rev. B* 52 (1995) R11662.
- [217] R.D. Johnson, M.S. de Vries, J.R. Salem, D.S. Bethune, C.S. Yannoni, *Nature* 355 (1992) 239.
- [218] T. Pichler, M.S. Golden, M. Knupfer, J. Fink, U. Kirbach, P. Kuran, L. Dunsch, *Phys. Rev. Lett.* 79 (1997) 3026.
- [219] F. Gerken, *J. Phys. F* 11 (1983) 113.
- [220] T. Pichler, M. Knupfer, M.S. Golden, T. Böske, J. Fink, U. Kirbach, P. Kuran, L. Dunsch, *Appl. Phys. A* 66 (1998) 281.
- [221] C.L. Nicklin, C. Binns, S. Mozley, C. Norris, E. Allen, M.G. Barthes-Labrousse, G. van der Laan, *Phys. Rev. B* 52 (1995) 4815.
- [222] J. Sugar, *Phys. Rev. B* 5 (1972) 1785.

- [223] T. Pichler, J. Winter, C. Grazioli, M.S. Golden, M. Knupfer, P. Kuran, L. Dunsch, J. Fink, *Syn. Met.* 103 (1999) 2470.
- [224] T. Pichler, M. Knupfer, M.S. Golden, J. Fink, A. Rinzler, R.E. Smalley, *Phys. Rev. Lett.* 80 (1998) 4729.
- [225] M. Knupfer, T. Pichler, M.S. Golden, J. Fink, A. Rinzler, R.E. Smalley, *Carbon* 37 (1999) 733.
- [226] T. Pichler, M. Knupfer, M.S. Golden, J. Fink, A. Rinzler, R.E. Smalley, *Syn. Met.* 103 (1999) 2515.
- [227] P.E. Batson, *Phys. Rev. B* 48 (1993) 2608.
- [228] Y. Ma, P. Skytt, N. Wassdahl, P. Glans, D.C. Mancini, J. Guo, J. Nordgren, *Phys. Rev. Lett.* 71 (1993) 3725.
- [229] E.J. Mele, J.J. Ritsko, *Phys. Rev. Lett.* 43 (1979) 68.
- [230] P. Brühwiler, A.J. Maxwell, C. Puglia, A. Nilsson, S. Andersson, N. Martensson, *Phys. Rev. Lett.* 74 (1995) 614.
- [231] M. van Veenendaal, P. Carra, *Phys. Rev. Lett.* 78 (1997) 2839.
- [232] E.L. Shirley, *Phys. Rev. Lett.* 80 (1998) 794.
- [233] R. Kuzuo, M. Terauchi, M. Tanaka, Y. Saito, *Jpn. J. Appl. Phys.* 33 (1994) L1316.
- [234] A.A. Lucas, L. Henrad, Ph. Lambin, *Phys. Rev. B* 49 (1994) 2888.
- [235] M.F. Lin, K.W.K. Shung, *Phys. Rev. B* 50 (1994) 17744.
- [236] M.F. Lin, D.S. Chu, C.S. Huang, Y.K. Lin, K.W.K. Shung, *Phys. Rev. B* 53 (1996) 15493.
- [237] M. Knupfer, J. Fink, E. Zojer, G. Leising, U. Scherf, K. Müllen, *Phys. Rev. B* 57 (1998) R4202.